

Distribution Agreement

Distribution Agreement

In presenting this thesis or dissertation as a partial fulfillment of the requirements for an advanced degree from Emory University, I hereby grant to Emory University and its agents the non-exclusive license to archive, make accessible, and display my thesis or dissertation in whole or in part in all forms of media, now or hereafter known, including display on the world wide web. I understand that I may select some access restrictions as part of the online submission of this thesis or dissertation. I retain all ownership rights to the copyright of the thesis or dissertation. I also retain the right to use in future works (such as articles or books) all or part of this thesis or dissertation.

Signature:

_____ Date 2016/06/06
Hening Wang

Approval Sheet

Development of Multi-modality polymer-coated Quantum Dots for cancer imaging

By

Hening Wang
Doctor of Philosophy
Biomedical Engineering

[Advisor's signature]
Qiushi Ren
Advisor

[Advisor's signature]
Shuming Nie
Co-advisor

[Member's signature]
Changhui Li
Committee Member

[Member's signature]
Peng Xi
Committee Member

[Member's signature]
Xiaodong Liu
Committee Member

Accepted:

Lisa A. Tedesco, Ph.D.
Dean of the James T. Laney School of Graduate Studies

Date

Abstract Cover Page

Development of Multi-modality polymer-coated Quantum Dots for cancer imaging

By

Hening Wang
B.A. Shanghai Jiao Tong University, 2010

Advisor: Dr. Qiushi Ren and Dr. Shuming Nie

An abstract of
A **dissertation** submitted to the Faculty of the
James T. Laney School of Graduate Studies of Emory University
in partial fulfillment of the requirements for the degree of
Doctor of Philosophy
in **Biomedical Engineering**
2016

Abstract

Abstract

Development of Multi-modality polymer-coated Quantum Dots for cancer imaging

By Hening Wang

Cancer has become a large threat to people's health and lives in the world. It is very important if we can achieve the early diagnosis of cancer, which can significantly reduce cancer mortality and improve the life quality of patients. Nanotechnology is currently widely used in cancer diagnosis and treatment. Nanometer-sized Quantum Dots have intrinsic optical, electronic, and structural properties therefore they have found many applications in the biomedical imaging field. For better applications, we need the QDs to have excellent water-stability, biocompatibility and even targeting ability. Here, we design and develop novel biocompatible Hyaluronic acid polymer coated QDs for CD44⁺ cancer targeted imaging. The resulted QDs not only have good water solubility, biocompatibility, strong stability, but also achieved CD44 receptor targeted cancer cell imaging. The development of multi-modal imaging equipment requires the design for multi-modality imaging probes. We synthesized DTPA and DOTA chelating agent conjugated hyaluronic acid, which can couple magnetic resonance imaging elements-Gd, and PET isotopes-Cu respectively to make a NIR / MR or NIR / PET dual-modality imaging probes. The multi-modality imaging probe holds the ability for fluorescence imaging, magnetic resonance imaging and PET imaging which can complement the advantages of different imaging modality and help to enhance tumor identification and diagnostic capabilities. We expect our novel method to have broad applications in biomedical imaging research, for the realization of precise diagnosis of tumors, as well as to promote personalized medicine.

Development of Multi-modality polymer-coated Quantum Dots for cancer imaging

By

Hening Wang
B.A. Shanghai Jiao Tong University, 2010

Advisor: Dr. Qiushi Ren and Dr. Shuming Nie

A **dissertation** submitted to the Faculty of the
James T. Laney School of Graduate Studies of Emory University
in partial fulfillment of the requirements for the degree of
Doctor of Philosophy
in **Biomedical Engineering**
2016

ACKNOWLEDGEMENTS

I would like to thank all the people that come to my life and I dedicated this thesis to all of you. I would like to thank my family, my mentors, labmates, and friends in my life and am forever grateful for the support you have given to me during the completion of my PhD.

First, I would like to thank my advisors. I thank Dr. Qiushi Ren and Dr. Peng Xi to gave me this opportunity to be a PhD candidate and have two years' study in the US. Thank you for your patient coach and help on my study. I thank Dr. Shuming Nie, you have inspired me a lot on my research. Without your support, I cannot learn that much in the US. Your generous help and kindness is my spiritual prop and your pursuit for truth will always encourage me. I thank Dr. Hongfang Sun, you are a pure and able women full of love, your kind guidance and direction benefits me a lot, and your attitude towards research and life will always be my role model. I also thank Dr. Changhui Li, Dr. Andrew Smith and Dr. Hui Wei, you are so nice and I appreciate all of your help on my study and research.

I would like to thank my labmates in Peking University and in Georgia Tech and Emory Univerisity. I would like to thank Dr. Brad Kairdolf, Dr. Lucas Lane, Dr. Yichen Ding, Dr. Guohe Wang, Jian Tian, and all the labmates. Thank you for your support and help not only on my research, but also the good memories that we have.

I would like to thank my parents, Hui Wang and Jianheng Wang, who have always supported me. You filled my life with all your love, stand by me at any time and encourage me to pursue better education and a life of continuous learning. I thank my

handsome and brilliant husband Hechao Wang, your love and your shoulder is the strongest support during the completion of my degree. I thank all my grandparents, my parents in law and sister in law and all my family members for your endless love and support.

Finally I would like to thank all my friends. I thank Dr. Wei Yang, my soulmate. The luckiest thing in my life is that I met you in my PhD and I cherish all the time that I had with you. I thank Zhen Zhen, Yang Wang and all the friends. Thank you for your support and help.

I'd like to thank everyone that come to my life who has supported and helped me to get here today. Thank you for all.

TABLE OF CONTENTS

<u>CHAPTER</u>	Page
1 Introduction	1
1.1 Background	1
1.2 Thesis goals	6
2 Semiconductor Quantum Dots and biological applications	8
2.1 Semiconductor physics and semiconductor nanocrystals	8
2.1.1 Semiconductor physics and nanocrystals	8
2.1.2 Properties of Quantum Dots	10
2.2 Chemical synthesis and coating methods of Quantum Dots	13
2.2.1 Chemical synthesis of QDs	13
2.2.2 QDs coating methods	14
2.2.3 Bioconjugation of QDs	17
2.3 Biological applications of Quantum Dots	18
2.3.1 Fixed cells and tissue staining	18
2.3.2 live cell imaging	20
2.3.3 <i>In vivo</i> animal imaging	21
2.3.4 Challenges and opportunities	22
3 Biocompatible Hyaluronic Acid-cystamine polymer coated QDs for cancer cell imaging	25
3.1 HA applications and the mechanism for targeting CD44 receptor	25
3.1.1 Hyaluronic Acid	25
3.1.2 CD44 receptor	30
3.1.3 HA-based CD44 targeted imaging using QDs	32

3.2 Materials and Methods	33
3.2.1 Materials	33
3.2.2 Methods	34
3.3 Results and Discussions	38
3.3.1 Results	38
3.3.2 Discussions	47
3.4 Summary	49
4 Multi-modality HA coated-QDs for optical/MRI/PET imaging	51
4.1 Background of Multi-modality imaging probes	51
4.1.1 Background	51
4.1.2 Multi-modality QDs probes	55
4.2 HA-DTPA-Gd QDs for dual-modality optical/MRI imaging	61
4.2.1 Materials and Methods	61
4.2.2 Results and Discussions	68
4.2.3 Summary	80
4.3 HA-DOTA-Cu QDs for dual-modality optical/PET imaging	81
4.3.1 Materials and Methods	81
4.3.2 Results and Discussions	85
4.3.3 Summary	89
4.4 Summary	89
5 Summary	91
REFERENCES	93

LIST OF TABLES

	Page
Table 4.1: Typical amount for HA-cystamine synthesis	63
Table 4.2: Typical amount for HA-cystamine conjugating DTPA	64
Table 4.3: Typical amount for Gd coupling with HA-cystamine-DTPA polymer	64
Table 4.4: Typical amount for HA-cystamine synthesis	83
Table 4.5: Typical amount for HA-cystamine conjugating DOTA	84

LIST OF FIGURES

	Page
Figure 1.1: Among all the cancers, Lung, liver, stomach, colorectal and breast cancers cause the most cancer deaths each year. (from 2014 world cancer report [1])	2
Figure 1.2: Nanometer scale comparison showing the nanoparticles size (from Peter R. Wich Research Lab)	3
Figure 2.1: (A). Diagram of electronic energy bands in solid-state materials showing the Bandgap (E_g) of semiconductor. E_g is the separation between the conduction and valence energy bands. (B). Electronic transitions in a semiconductor. (Figure from Andrew M. Smith.)	9
Figure 2.2: Size-tunable fluorescence properties and spectral range of six QD dispersions. (from Mattoussi et al. [2])	11
Figure 2.3: Photostability comparison between QDs and Alexa 488. (from Wu et al. [3])	12
Figure 2.4: QDs coating and bioconjugation methods (from Smith et al. [4])	16
Figure 2.5: Pseudocoloured image depicting five-colour QD staining of fixed human epithelial cells. Courtesy of Quantum Dot Corp. (from Wu et al. [3])	19
Figure 2.6: Multiplexed molecular profiling of FFPE tissue sections. (from Maksym V. Yezhelyev et al. [5])	19
Figure 2.7: Simultaneous <i>in vivo</i> imaging of multicolor QD-encoded microbeads. (from Gao et.al. [6])	22
Figure 2.8: Applications of quantum dots as multimodal contrast agents in bioimaging (from X. Michalet et al. [7])	24
Figure 3.1: The structure of HA)	26
Figure 3.2: Schematic illustration of HA-based 3-D constructs for cartilage engineering. (from Pereira et al. [8])	28
Figure 3.3: Advantages of drug delivery systems of chemotherapy agent conjugated with macromolecules (from Posocco et al. [9])	29
Figure 3.4: HA-based RNAi delivery nano-platform for siRNAs (from Choi et al. [10])	30
Figure 3.5: Synthesis of a hyaluronic acid–quantum dot (HA-QDot) conjugate using adipic acid dihydrazide-modified HA (HA-ADH) (from Kim et.al. [11])	32

Figure 3.6: Preparation of HA-cysteamine polymer-coated QDs. (a) The chemical synthesis of HA-cysteamine polymer. (b) Schematic illustration of HA polymer coating on QDs	39
Figure 3.7: Schematic illustration of reverse micelle phase transfer procedure for HA-cysteamine polymer coated QD synthesis	40
Figure 3.8: Characterization of QDs	41
Figure 3.9: pH stability of HA-cysteamine polymer coated QDs	43
Figure 3.10: Long-time stability of HA-cysteamine polymer coated QDs, compared with MAA coated QDs	43
Figure 3.11: Stability in cell culture medium of HA polymer coated QDs and commercial carboxyl QDs from Invitrogen	44
Figure 3.12: Cytotoxicity test of HA-cysteamine polymer-coated QDs	45
Figure 3.13: Illustration of the targeted imaging of breast cancer cells with HA-cysteamine polymer-coated QDs with final concentration of 5 and 10 nM	46
Figure 3.14: HA receptor competitive targeted imaging of MCF-7 cell line with HA-cysteamine polymer-coated QDs treated with different concentrations of HA47	
Figure 4.1: Comparisons of advantages and limitations for each imaging modality (from Yan Xing et al. [12])	52
Figure 4.2: Multi-modality imaging machines (A) Quad-modality imaging system design, which consisted of PET, CT, SPECT, and FMI modules. (B) Photograph of quad-modality imaging prototype system. (from Lu et al [13])	53
Figure 4.3: Synthesis of dual-function PET/NIRF probe DOTA-QD-RGD through Chelator coupling to surface of CdTe nanoparticles. (from Louie [14])	56
Figure 4.4: Synthesis of lipid-coated multi modality QDs (form Louie [15])	58
Figure 4.5: Schematic shown for the synthesis of the Gd:CdTe QDs and their surface function with Folic acid. (from Zhang et.al [16])	59
Figure 4.6: Schematic illustration of functionalized QD probe for in vivo cancer dual-targeting and dual-modality imaging (from Kongzhen Hu et al. [17])	60
Figure 4.7: Synthesis routes of HA-DTPA-Gd polymer	63
Figure 4.8: FT-IR image of HA and HA-cystamine-DTPA	69
Figure 4.9: NMR image of HA-cystamine-DTPA	70

Figure 4.10: NMR prediction by chemdraw of HA-cystamine-DTPA	70
Figure 4.11: UV-absorption and Fluorescence image of QDs and HA-QDs	71
Figure 4.12: TEM figures of QDs in decane (A) and HA-Gd QDs (B)	72
Figure 4.13: T1-weighted MR images of HA-Gd QDs and DTPA-Gd solution at different TE value	73
Figure 4.14: The matlab code used for calculating the T1 value at different concentrations of Gd	74
Figure 4.15: The typical curve for T1 value calculation	74
Figure 4.16: The proton longitudinal relaxation rate ($1/T_1$) according to the Gd concentration	75
Figure 4.17: Cell viability test of Hela cells	76
Figure 4.18: Fluorescence microscopic images of Hela and NIH/3T3 cells labeled with HA-Gd QDs	77
Figure 4.19: The HA-Gd QDs that was used to inject the mouse (A) Bright field image. (B) Fluorescence image. (C) Overlay of the bright field and fluorescence images	77
Figure 4.20: <i>In vivo</i> fluorescence imaging of Hela tumor-bearing mice injected with HA-Gd QDs. (A) before injection (B) 1 h (C) 2 h (D) 3 h (E) 6 h after HA-Gd QDs was injected. The figures are the merged images of bright field and fluorescence images. All of the images were taken under the same condition	78
Figure 4.21: The fluorescence image of the tumor and organs of the mouse. (A) photo to show the organs and tumor. (B) Bright field image. (C) Fluorescence image. (D) Overlay of the bright field and fluorescence images	79
Figure 4.22: T1-weighted MR images of the mice bearing Hela tumor (as indicated by arrow) following tail vein injection of HA-Gd QDs obtained at 0 h (before injection, Figure A) and 1 h (Figure B) after injection	80
Figure 4.23: Synthesis routes of HA-DOTA polymer	82
Figure 4.24: FT-IR image of HA and HA-cystamine-DOTA	85
Figure 4.25: NMR of HA-cystamine-DOTA and HA	86
Figure 4.26: NMR prediction of HA-cystamine-DOTA by Chemdraw	87
Figure 4.27: UV-absorption and Fluorescence image of QDs and HA-Cu QDs	87

- Figure 4.28: TEM figure of HA-DOTA Cu QDs to show a size distribution 88
- Figure 5.1: Multi-modality imaging probe based on our HA-cystamine QDs system 92
- Figure 5.2: Multi-modality imaging probe based on our HA-cystamine Au NP system 92

CHAPTER 1

INTRODUCTION

1.1 Background

Cancer by definition is the uncontrolled growth of cells that can invade and spread to distant sites of the body. Cancer can have serious health consequences, and is a leading cause of death all over the world. Cancer affects everyone and brings a tremendous burden to patients, families and societies. Cancer is a leading cause of death worldwide, and accounts for 8.2 million deaths in 2012. From the 2014 world cancer report, cancers figure among the leading causes of morbidity and mortality worldwide, with about 14 million new cases and 8.2 million cancer related deaths in 2012 [1]. It is expected that annual cancer cases will rise from 14 million in 2012 to 22 million within the next two decades. As Dr. Varmus mentioned, ‘Indeed, the age-adjusted mortality rate for cancer is about the same in the 21st century as it was 50 years ago, whereas the death rates for cardiac, cerebrovascular, and infectious diseases have declined by about two-thirds.’[18] Early detection, accurate diagnosis, and effective treatment help increase cancer survival rates and reduce suffering. Among all the cancers, lung, liver, stomach, colorectal and breast cancers cause the most cancer deaths each year, as shown in Figure 1.1. Research has vastly expanded our knowledge of cancer and cancer biology, particularly with new insights into the molecular mechanism of the disease[19, 20]. Although people have made a lot of progress in the treatment of cancer, substantial hurdles still remain because of its complexity nature. Because of these research efforts and recent advances in diagnostic technologies, there is an opportunity to bring the idea of ‘personalized medicine’ to reality. As WHO pointed out, 30% of cancers could be

prevented and early detection of cancer will greatly improve the likelihood for successful treatment.

Nanotechnology is a multidisciplinary field and it covers a broad diversification range from engineering, biology, physics and chemistry [21]. Formal definition of nanotechnological devices typically feature the requirements that the device itself or its essential components be man-made, and in the 1–100 nm range which is from a few atoms to subcellular size in at least one dimension. Two main fields of nanotechnology are nanovectors for the administration of targeted therapeutic and imaging moieties and the precise patterning of surfaces. Cancer-related examples of nanotechnologies include injectable drug delivery nanovectors such as liposomes for the therapy of breast cancer, biologically targeted, nanosized contrast agents for intraoperative imaging and novel, nanoparticle-based methods for high-specificity detection of DNA and protein. If properly combined with cancer research, nanotechnology provides a lot of opportunities to meet the challenges in cancer.

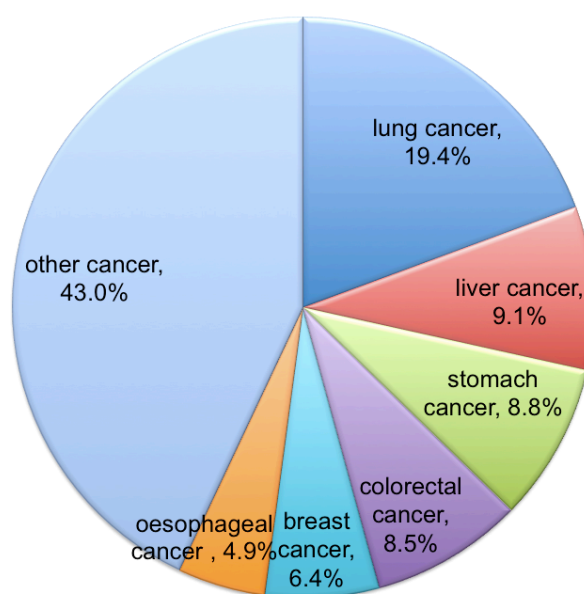


Figure 1.1. Among all the cancers, Lung, liver, stomach, colorectal and breast cancers cause the most cancer deaths each year. (from 2014 world cancer report [1])

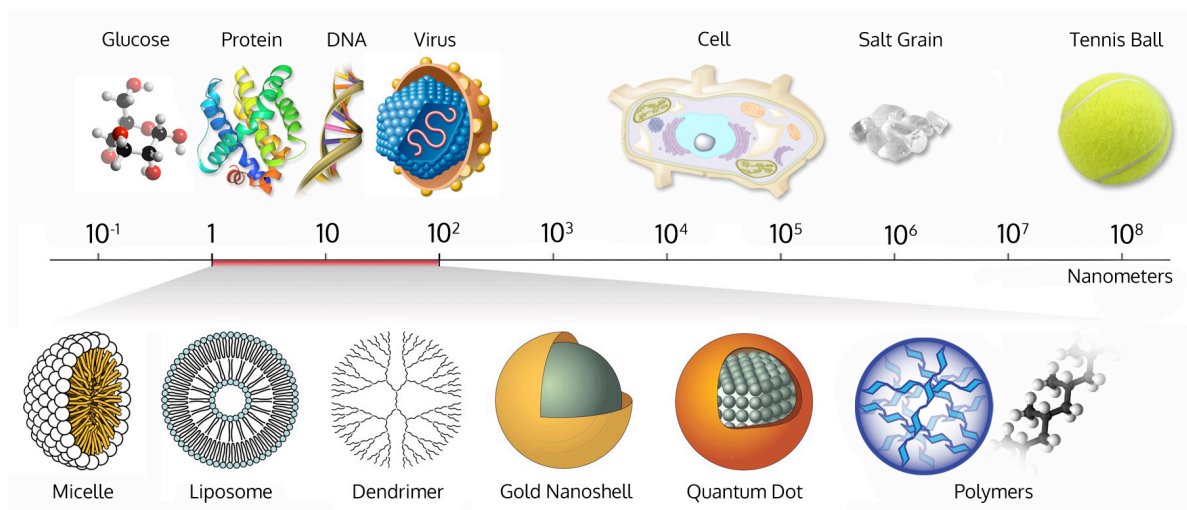


Figure 1.2. Nanometer scale comparison showing the nanoparticles size (from Peter R. Wich Research Lab)

Multifunctionality is the fundamental advantage of nanovectors for the cancer-specific delivery of therapeutic and imaging agents. The size and multicomponent nature of many nanomaterials offer an excellent platform to combine different materials for various imaging modalities. Primary functionalities include the avoidance of biobarriers and biomarker-based targeting, and the reporting of therapeutic efficacy. The dilemma of imaging modality selection in the clinic is that each modality has its own unique advantages and intrinsic limitations [22], such as insufficient sensitivity or low spatial resolution, so it remains difficult to extract accurate and reliable biomedical information solely based on single imaging modalities. Integrating the advantages of different imaging techniques is apparently an effective approach for improving the efficacy of clinical imaging diagnosis. Although the optical imaging techniques have shown potentials in extracting detailed biomedical information with high imaging sensitivities and low cost in imaging facilities, the assist of anatomical information is essentially required. Although not all imaging applications require multiple imaging modalities bind to a single probe, a multi-modality imaging probe has many advantages. A multi-modal

probe can guarantee the same pharmacokinetics and co-localization of different imaging modes. Also it avoid using multiple doses of imaging probes to bring a lot of pressure to the *in vivo* blood clearance [14].

A combination of MRI and optical imaging techniques can achieve more accurate biomedical detection, in which the whole body MRI or optical imaging can be used to track the probe distribution in the body [22-24]. Although the body optical imaging is less powerful compared to MRI, fluorophores allow histological studies after whole body imaging where optical imaging provides great convenience.

QDs are nanometer-sized crystals of semiconductor materials (typically 2-8 nm) that emit fluorescent light with great intensity and unparalleled signal stability. These attributes have found immediate use for monitoring individual molecules on cell surfaces in real time for extended periods, for sensitive detection of cancer *in vivo*, and for sensitive and specific characterization of viruses and cancer antigens in body fluids[2, 4, 6, 25-33]. Compared with traditional organic dyes and fluorescent proteins, QDs are highly bright and resistant to photobleaching. Even importantly they have size, composition, and lattice strain tunable emission wavelength [4, 34-36]. However, great concern has been raised over the application of quantum dots in living cells and animals due to their chemical composition of toxic heavy metals like Cd. Some studies have indicated that the cytotoxicity of QDs strongly correlated with the stability and surface coatings of these nanoparticles[6, 31, 37, 38]. Besides, for biomedical applications, ideal QDs should not only have good water solubility, high stability, minimized cell toxicity, but also have abundant functional groups such as amine ($-NH_2$) and carboxyl ($-COOH$) groups for further conjugation toward specific targeted imaging.

A number of QDs surface coating methods have been used, which include silica coating [25, 38, 39], encapsulation with amphiphilic polymers (most commercial water-soluble QDs) [40-42], and ligand replacement with hydrophilic ligands [27, 43, 44]. Silica shell coating and amphiphilic polymer encapsulation provide QDs with good

aqueous solubility and preserve high photoluminescence quantum yields. However, this approach is complex and usually results in large hydrodynamic diameters of 30–50 nm [27, 38], which are often much larger than the cellular receptors being labeled, and become a barrier for the widespread application of QDs in biomedical imaging. Due to the particularly strong affinity of sulfur for the metallic cations on the surface of QDs, mercaptopropionic acid (MPA) [27] and cysteine [43] are widely used as phase transfer reagents for QDs, owing to its simplicity, speed, and smaller size. Nevertheless, the colloidal stability is still limited due to the poor protection and drastic decrease in the quantum yields of the resulting water-soluble QDs. Thus, how to obtain water-soluble QDs with high quantum yield and high stability remains a great challenge.

Another way to make QDs watersoluble is through multidentate polymer coating by ligand exchange, which usually produces compact QDs with high colloidal stability, with different combinations of polymer backbone, anchoring groups and pendant groups [44-54]. However, further bioconjugation is needed since there are not any recognition sites on common polymers, which will increase the size of QDs and make the experiment too complicated. Therefore, if one can realize specific targeting and good stability as well as biocompatibility through one surface modification step, it would be very convenient for the further biomedical application of QDs.

At present, many people have used quantum dots to develop a lot of bimodal probes, such as PET or MRI. These methods can mainly be divided into three categories [14]. The first is through conjugates and other molecules such as Gd and Cu are attached to the QDs through surface chemistry. A typical approach is to attach chelators such as tetra-azacyclododecanetetra-acetic acid (DOTA) and diethylenetriaminepentaacetic acid (DTPA) to the surface of QDs to metalate PET- or MRI-active molecules Cu and Gd [55-57]. The second method is through core-shell structure and other molecules are incorporated by adding them in an additional layer coating the QDs [58, 59]. The third method is by doping appropriate molecules such as Mn to the core of the QDs [22, 60].

Hyaluronic acid (HA), which is a natural polysaccharide abundant in extracellular matrix, has been widely used in skin care [61, 62] and wound healing [63, 64] due to its intrinsic physicochemical and biological properties including great water retention ability and biocompatibility. HA is also reported to selectively bind with CD44 receptor, which is overexpressed in many cancers of epithelial origin [65] such as ovarian carcinoma [66] and breast adenocarcinoma [67]. Owing to these unique features, HA has been used for development of the targetable carriers to deliver the therapeutic agents such as drug delivery [68] and siRNA delivery [69-71] as well as imaging agents [72, 73]. Additionally, HA also contains derivable functional groups along its backbone. For instance, the carboxyl groups are good sites to be conjugated with thiol-containing cysteamine for QD surface binding. The hydroxyl groups can also act as good sites to conjugate DTPA, the Gd coupling unit for MRI imaging and conjugate DOTA, the Cu coupling unit for PET imaging [74, 75].

1.2 Thesis goals

This thesis aims to establish a facile and convenient method to obtain multimodality imaging probes based on QDs for the development of advanced functional nanometer scale tools for multimodality and targeted imaging of cancer. This goal is approached from three directions.

First, an understanding of the physics of the optical and electronic properties of quantum dots, previous coating and bioconjugation methods for QDs and biomedical applications of QDs is summarized. This is performed by providing an exhaustive review of the properties and applications of quantum dots (Chapter 2).

Second, a novel biocompatible Hyaluronic acid polymer was modified to coat the QDs and the colloidal properties of these nanocrystals were studied comprehensively. Its cellular toxicity and targeted imaging ability was also studied (Chapter 3).

Finally, the possibility of making multimodality QDs was tried by conjugating the HA cystamine polymer with DTPA and DOTA. HA-DTPA cysteamine polymer-coated QDs were conjugated with Gd for dual-modality MRI/optical imaging applications. Those QDs were used for MRI imaging and its longitudinal relaxation rate was calculated. HA-DOTA cystamine polymer was also synthesized and conjugated with Cu. The Cu content was determined by ICP-AES (Chapter 4).

We expect the multi-modality imaging methods can be extended to SPECT/optical, MRI/PET/optical, CT/PET/SPECT imaging and other combinations for multi-modality imaging and find more applications in cancer imaging.

CHAPTER 2

SEMICONDUCTOR QUANTUM DOTS AND BIOLOGICAL APPLICATIONS

Abstract

Quantum dots are nanometer-sized nanocrystals composed of semiconductor materials that have unique optical and electronic properties. The most important and useful feature of these particles is their size-dependent absorption and photoluminescence, which make them ideal for use in a number of biomedical applications. In this chapter, we will discuss the physical principles and properties of QDs. We will also describe the synthesis and coating methods of QDs. Finally, the relevant uses of QDs for biological applications will also be discussed.

2.1 Semiconductor physics and semiconductor nanocrystals

2.1.1 Semiconductor physics and nanocrystals

Solid state physics and materials science broadly classify solids as conductors, semiconductors, or insulators, depending on the capacity of the materials to conduct electricity at room temperature. The difference between these materials arises from the bandgap energy (E_g), the energy difference between the highest occupied electronic energy level and the lowest unoccupied electronic energy level. The energy difference separating these bands is called the bandgap, a region of forbidden electronic energy within the solid. If an electron is excited, for example absorption of a photon whose energy is greater than the bandgap, or through thermal excitation, the electron is free to move in the solid upon application of an electric field, thus generating current.

Semiconductors have energy gaps that are small enough to allow room temperature conduction, but large enough that the magnitude of conduction can be largely controlled by a host of useful intrinsic and extrinsic factors, such as doping, the presence of a magnetic field, material strain, or incident light.

When a photon of light with energy greater than E_g is illuminated on a semiconductor material, the electrons in the material can absorb the photon to transition to a higher electronic energy level, resulting in an excited state electron. As shown in Figure 2.1 B, an electron in the valence band absorbs a photon (green), exciting it to the conduction band, and leaving a positively charged hole in the valence band. The electron and hole quickly lose their excess kinetic energies through dissipation to lattice vibrations, settling at the band edges in a process called relaxation. The electron and hole can then recombine in a process that yields the emission of a single photon (red) with energy equal to the bandgap energy.

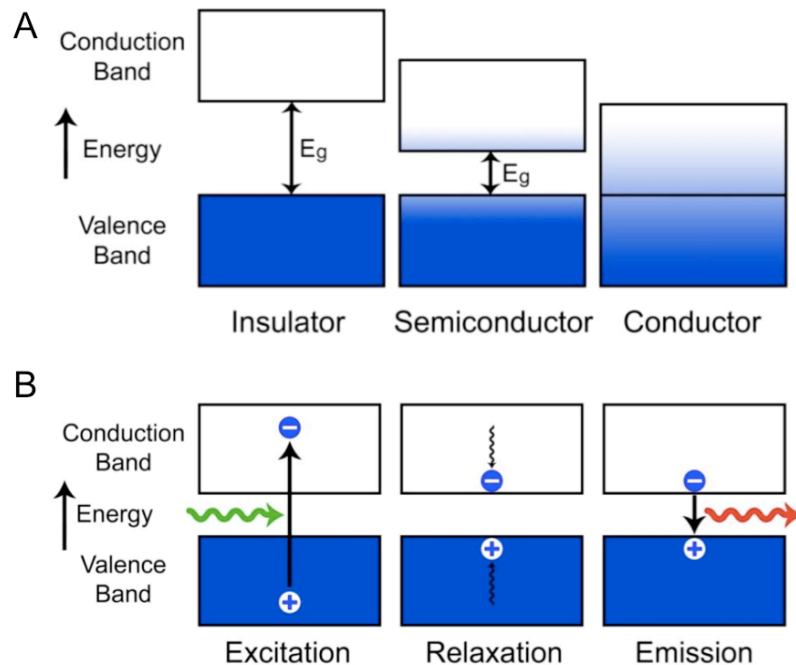


Figure 2.1. (A). Diagram of electronic energy bands in solid-state materials showing the Bandgap (E_g) of semiconductor. E_g is the separation between the conduction and valence energy bands. (B). Electronic transitions in a semiconductor. (Figure from Andrew M. Smith.)

Many of the unique electronic and optical properties of QDs are the result of a phenomenon called “quantum confinement” [76-78]. The first excited state of a semiconductor is the exciton state, in which an electron-hole pair is coulombically stabilized. The exciton state has a fundamental unit of length dictated by its Bohr radius, which can assume a value less than 1 nm diameter to over 100 nm, depending on the material. Therefore if the dimensions of the semiconductor crystal are on the nanometer scale, the electronic properties of a semiconductor can significantly differ from those of the bulk crystal. When a crystal is shrunk to a size similar to the Bohr diameter, the exciton becomes highly localized in space in the crystal. Similar to the classic example in quantum mechanics of a “particle in a box,”[79] the lowest energy state of the exciton (particle) will increase if the semiconductor nanocrystal (box) shrinks. This “quantum confinement effect” results in an increase in energy required to create the exciton and an increase in energy generated when the electron and hole recombine, i.e. an increase in the bandgap. This effect is illustrated by the characteristic blue-shift of the absorption and luminescence spectra for semiconductors nanocrystals near or smaller than the size of the exciton.

The most important consequence of the quantum confinement effect is the size dependence of the bandgap for nanocrystalline semiconductors. By confining the exciton of a semiconductor, the bandgap may be tuned to a precise energy depending on the dimensionality and degree of confinement.

2.1.2 Properties of Quantum Dots

QDs are nanometer-sized crystals of semiconductor materials (typically 2-8 nm) that emit fluorescent light with great intensity and unparalleled signal stability. These attributes have found immediate use for monitoring individual molecules on cell surfaces in real time for extended periods, for sensitive detection of cancer *in vivo*, and for sensitive and specific characterization of viruses and cancer antigens in bodily fluids [2,

4, 6, 25-33]. Compared with traditional organic dyes and fluorescent proteins, QDs are highly bright and resistant to photobleaching. Even importantly they have size, composition, and lattice strain tunable emission wavelength [4, 34-36].

The absorption and emission spectra of six different QDs was shown in Figure 2.2. The black line shows the absorption of the QDs at 510nm emission. Size-tunable fluorescence properties and spectral range of the six QDs compare to CdSe core size were also plotted. All samples were excited at 365 nm with a UV light source [2]. Simultaneous excitation of multiple fluorescence colors spanning the entire visible range allows highly multiplexed staining of different disease biomarkers.

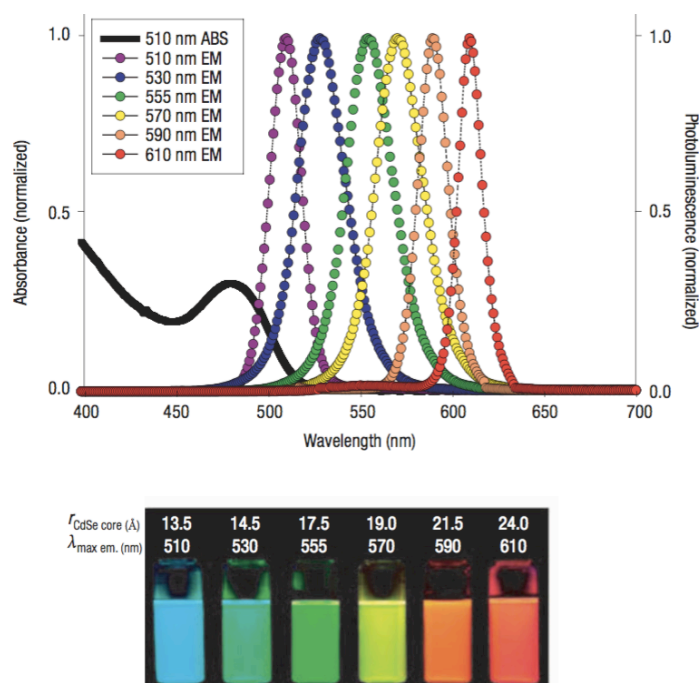


Figure 2.2. Size-tunable fluorescence properties and spectral range of six QD dispersions. (from Mattoussi et al. [2])

Resistance to photobleaching is another important feature that is necessary for use in clinical applications. Unlike organic dyes that can easily photobleach upon exposure to light, the constant fluorescence intensity of QDs make them ideal imaging and biosensing agents. As shown in Figure 2.3 [3], Nuclear antigens were labeled with QD 630–

streptavidin (red), and microtubules were labeled with Alexa 488 conjugated to anti-mouse IgG (green) simultaneously in a NIH/3T3 cell. The photos in bottom row showed microtubules that were labeled with QD 630–streptavidin (red), and nuclear antigens were stained green with Alexa 488 conjugated to anti-human IgG. The specimens were continuously illuminated for 3 min with light from a 100 W mercury lamp under a 100 times 1.30 oil-immersion objective. Images at 0, 20, 60, 120, and 180 s are shown. Whereas labeling signals of Alexa 488 faded quickly and became undetectable within 2 min, the signals of QD 630 showed no obvious change for the entire 3 min illumination period [3]. Quantitative analysis of changes in intensities of QD 608–streptavidin (stained microtubules) and Alexa 488–streptavidin (stained nuclear antigens) using specimens mounted with glycerol or antifade mounting medium were shown in Figure 2.3 B, QDs showed excellent photostability and resistance to photobleaching as compared to organic dyes, which make them ideal imaging and biosensing agents where consistent measurements are essential.

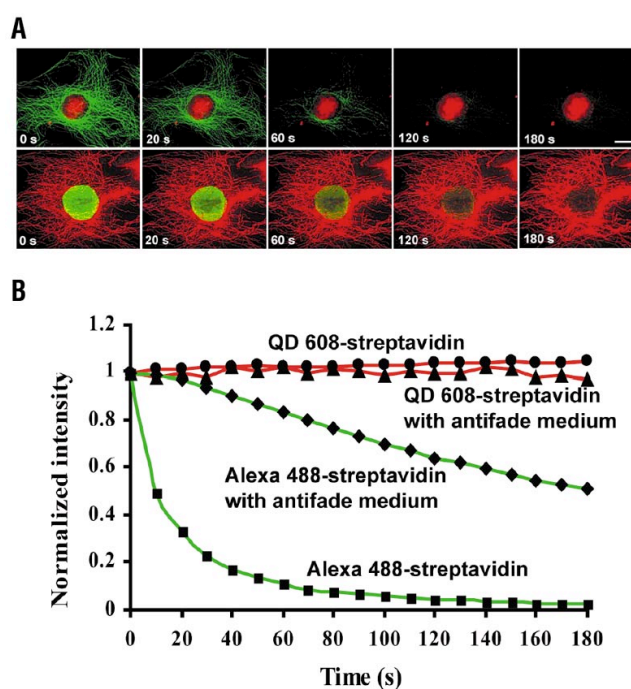


Figure 2.3. Photostability comparison between QDs and Alexa 488. (from Wu et al. [3])

2.2 Chemical synthesis and coating methods of Quantum Dots

2.2.1 Chemical synthesis of QDs

The synthesis of quantum confined semiconductor nanocrystals was first described in 1982 by Ekimov [80, 81], who grew nanocrystals and microcrystals of CuCl semiconductors in glass matrices. A major step toward the goal of monodisperse, colloiddally dispersible, and highly fluorescent quantum dots was made by Bawendi and coworkers in 1993 with the introduction of nanocrystal synthesis in a high temperature coordinating solvent composed of trioctylphosphine (TOP) and trioctylphosphine oxide (TOPO) [82]. This novel demonstration of temporal separation of nucleation and growth was found to be crucial for the production of monodisperse samples, although size-selective precipitations were still necessary to improve the size distribution.

The next major development in colloidal quantum dot synthesis was the demonstration that the overgrowth of an insulating shell on the surface of a quantum dot tremendously enhances the photoluminescence efficiency. For example, Arnim Henglein and coworkers found that the addition of excess cations to alkaline aqueous solutions of semiconductor colloids (e.g. Cd^{2+} for CdS) resulted in large fluorescence enhancements [83]. This was hypothesized to be the results of surface defect passivation, and a similar trend was found for the addition of alkylamines [84]. It was also reported that when a wider bandgap material (ZnS) was grown on top of semiconductor nanocrystals (CdSe) in reverse micelles, the luminescence efficiency was tremendously enhanced [85]. Bawendi and coworkers improved this synthetic method and analyzed the luminescence dependence of the shell thickness from the perspective of interfacial strain [86].

Up to now, considerable advances have been made in the chemical synthesis and preparation of high quality, monodispersed QDs [82, 87], especially with the use of organometallic and chelated cadmium precursors [88, 89], noncoordinating solvents [90], and inorganic passivating shells [86, 91]. These advances have led to the production of

nanoparticles with very narrow size distributions (fluorescence emission FWHM < 25 nm) and high quantum yields (QY > 75%).

While the resulting QDs have excellent physical and optical properties, the highest quality nanoparticles typically have hydrophobic surface ligands are often unsuited for use in biological environments. The production of biologically functional quantum dots has now become a multistep process involves three steps: 1. Synthesis of the nanocrystal core and growth of an inorganic shell (usually ZnS) to protect the optical properties of the quantum dot. 2. Coating of the QDs for phase transfer of the nanocrystal from organic liquid phase to aqueous solution. 3. Bioconjugation of biologically active molecules to the nanoparticle surface to render functionality, or linkage of biologically inert polymers to the nanoparticle to minimize biological activity.

2.2.2 QDs coating methods

To better make water-soluble QDs, a number of surface encapsulation and water solubilization strategies have been used to transfer QDs to aqueous solvents including direct ligand exchange of the hydrophobic surface ligands with hydrophilic small molecules, indirect surface encapsulation techniques using silica, lipids, block copolymers and low molecular weight amphiphilic polymers and multi-dentate polymers coating method.

Direct ligand exchange

For ligand exchange, a suspension of TOPO-coated quantum dots may be mixed with a solution containing an excess of a heterobifunctional ligand, which has one functional group that binds to the nanocrystal surface, usually a thiol group and another functional group that is hydrophilic. Thereby, hydrophobic TOPO ligands are displaced from the nanocrystal, as the new bifunctional ligand adsorbs to render water solubility. Thiol functional groups were found to strongly coordinate with the inorganic shell of the nanocrystal. Using this method, (CdSe)ZnS quantum dots have been coated with

mercaptoacetic acid [27] (3-mercaptopropyl) trimethoxysilane [25], and cysteine [43], which contain basic thiol groups to bind to the zinc atoms on the nanocrystal surface, yielding quantum dots displaying carboxylic acids or silane monomers, respectively. These methods with simplicity and speed generate quantum dots of smaller size and useful for biological assays. Nevertheless, the colloidal stability is still limited due to the poor protection, and ligand exchange is commonly associated with decreased fluorescent efficiency and a propensity to aggregate and precipitate in biological buffers.

Further advances have been made for this transfer strategy, using other functional groups to coordinate with the QD surface and ligand molecules capable of multivalent coordination to the surface [2, 44, 92-94], to improve the stability of the particles with different combinations of polymer backbone, anchoring groups and pendant groups [44-54], which usually produces compact QDs with high colloidal stability. In addition, biocompatible molecules such as amino acids, proteins have also been used for direct ligand exchange and QD coatings [95, 96].

Surface encapsulation with amphiphilic polymers

Another strategy for the transfer of QDs to aqueous environments involves the coating of the hydrophobic nanoparticles with amphiphilic polymers (most commercial water-soluble QDs) [40-42]. This method retains the native nonpolar coordinating ligands on the surface, and cover the hydrophobic nanocrystal with amphiphilic molecules, such as silica, lipids or polymers [6, 31, 97]. These methods yield water-soluble quantum dots that are stable for long periods of time due to a protective bilayer encapsulating the nanocrystal through hydrophobic interactions. Particles transferred using these techniques tend to have higher quantum yields than other particles, likely due to the protective layer of the hydrophobic segments of the polymer and the original surface ligands. These particles are also much more stable than ligand exchanged QDs, due to the multiple interactions between the polymer and the QD surface. One question of these strategies is a substantial increase in particle size. Nanoparticles are much larger when encapsulated

in amphiphiles compared to particles prepared using standard ligand exchange methods. This approach is complex and usually results in large hydrodynamic diameters of 30–50 nm [27, 38], which are often much larger than the cellular receptors being labeled, and become a barrier for the widespread application of QDs in biomedical imaging. Thus, how to obtain water-soluble QDs with high quantum yield and high stability remains a great challenge.

No matter what method was used to dissolve the quantum dots in water, for biological applications the QDs need to be purified, such as ultrafiltration, dialysis and other methods to remove excess chelators. In addition, the surface of the quantum dot can affect the biological and physical characteristics of the quantum dots and the thickness of the coated quantum dots will also affect the entire physical dimensions [4].

The use of quantum dots to observe molecular events in biology has become one of their most intriguing applications. For biological applications, further bioconjugation is needed since there are not any recognition sites on common polymers.

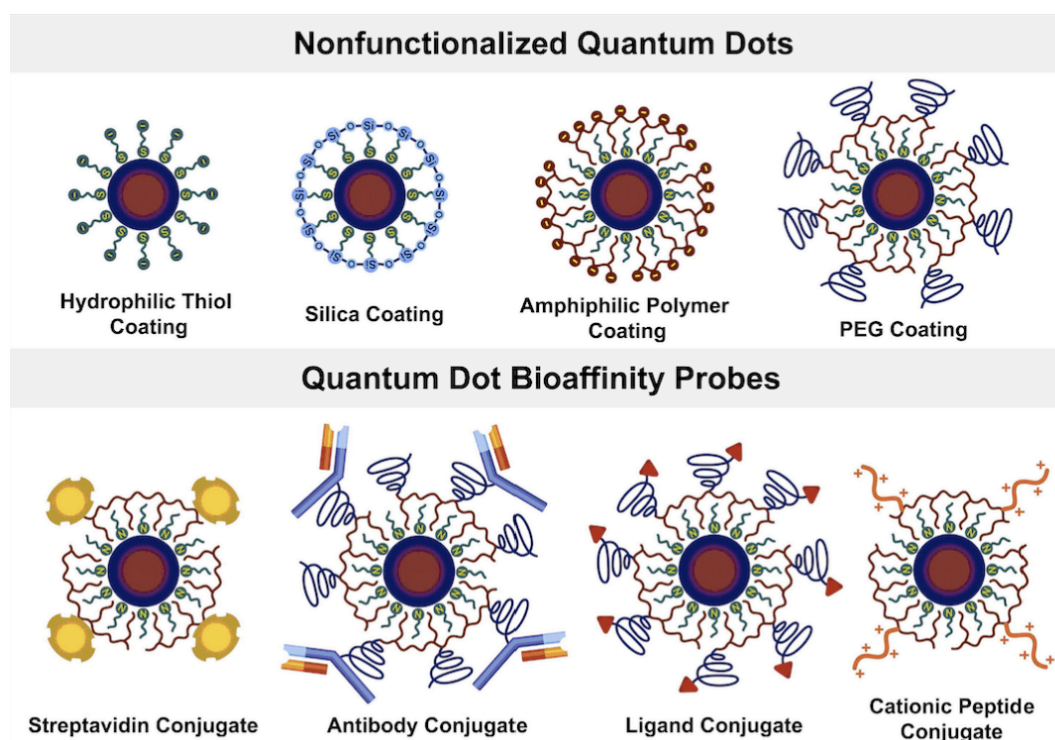


Figure 2.4. QDs coating and bioconjugation methods (from Smith et al. [4])

2.2.3 Bioconjugation of QDs

Biological specificity can be rendered by coupling to peptides, proteins, aptamers, nucleotides, polysaccharides, or small molecule ligands. Methods used to modify aqueous nanocrystals with bioaffinity molecules fall under several broad categories, with applicability dictated by the specific nanocrystal surface coating. Nanocrystals with accessible surface atoms can directly interact with biomolecules that contain chelating or strongly basic residues. This method has been used to successfully tag quantum dots coated with hydrophilic thiol ligands using peptides and nucleotides with reduced thiols [98, 99] and recombinant proteins containing histidine tags [100, 101]. These methods are generally not applicable for nanocrystals coated with thick hydrophobic bilayers, which have sterically inaccessible surface facets.

The most commonly used coupling scheme is the covalent coupling between functional groups of the organic surface coating and functional groups on proteins or other biomolecules. This typically involves amide bond formation between carboxylic acid groups on the quantum dot and primary amines on proteins using carbodiimide chemistry [32, 94]. This method is more specific, resulting in more predictable crosslinking geometries and reduced aggregation, especially for antibody-quantum dot coupling.

Bioconjugation may also be approached through a more modular direction using high-affinity streptavidin-biotin binding. Quantum dot-streptavidin conjugates are convenient for indirect binding to a broad range of biotinylated biomolecules, which are widely available commercially [31]. Biocompatible quantum dots are now commercially available, conjugated to a variety of functional biological molecules, like streptavidin, biotin, or monoclonal antibodies. Currently, bioconjugation methods are a major limiting step in the production of quantum dots for bioimaging applications due to the poor efficiency, specificity, reproducibility, scalability, and versatility of most coupling

schemes, and due to the inability to control the stoichiometry and geometry of binding [102].

More complex and specific bioconjugation methods are currently in development, including nickel-NTA-histidine interactions, SNAP-tagging, HALO-tagging, and crosslinking to glycosylated residues on proteins [32, 103].

2.3 Biological applications of Quantum Dots

Due to their novel optical and electronic properties, semiconductor QDs are being intensely studied as a new class of nanoparticle probe for molecular, cellular, and *in vivo* imaging [4, 104-122].

2.3.1 Fixed cells and tissue staining

Cell and tissue staining is an application that has received considerable attention for the use of QDs [31, 123, 124]. The fluorescence properties of QDs make them ideally suited for this type of application. Of particular interest for these applications are their photostability and the ability to excite multiple QD colors simultaneously. As shown in Figure 2.5, Pseudocoloured image depicts five-colour QD staining of fixed human epithelial cells. Cyan corresponds to 655-nm Qdots labelling the nucleus, magenta 605-Qdots labelling Ki-67 protein, orange 525-Qdots labelling mitochondria, green 565-Qdots labelling microtubules and red 705-Qdots labelling actin filaments [3]. Many different cellular antigens in fixed cells and tissues have been labeled using quantum dots, including specific genomic sequences [125], plasma membrane proteins [31], cytoplasmic proteins [25] and nuclear proteins, and it is apparent that they can function as both primary and secondary antibody stains. In addition, high resolution actin filament imaging has been demonstrated using quantum dot [31] , It is now clear that quantum dots are superior to organic dyes for fixed cell labeling.

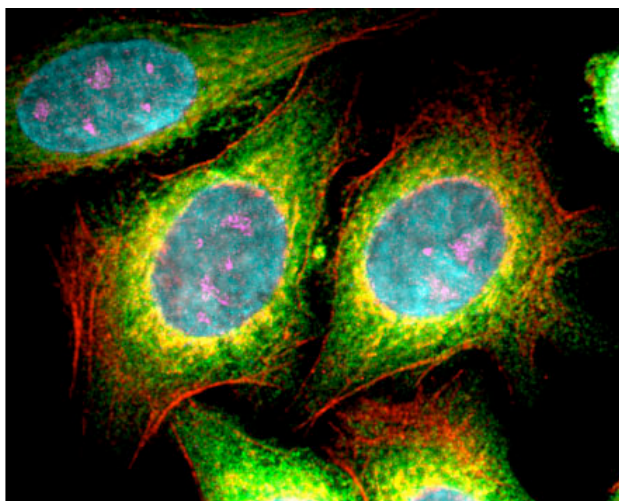


Figure 2.5. Pseudocoloured image depicting five-colour QD staining of fixed human epithelial cells. Courtesy of Quantum Dot Corp. (from Wu et al. [3])

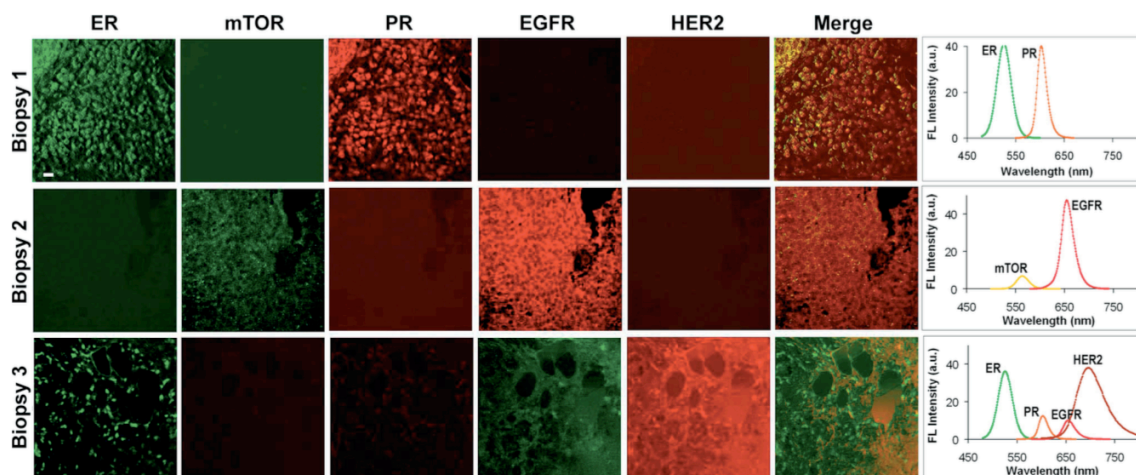


Figure 2.6. Multiplexed molecular profiling of FFPE tissue sections. (from Maksym V. Yezhelyev et al. [5])

Tissue staining is proving to be another exciting application for QDs [32]. The potential for multiplexing opens the possibility of a QD revolution for molecular imaging in cells and pathological analysis of tissues. As shown in Figure 2.6, up to five biomarkers have been simultaneously imaged in clinical tissue samples. Different

patterns of nuclear, cytoplasmic and cell membrane fluorescent signals were detected by microscopy (left panels, pseudo-color) and expression of these biomarkers was quantified by wavelength-resolved spectroscopy (right panels) [5], with the potential for even higher degrees of multiplexing. The optical stability of QDs also makes them attractive for this application, where samples are often stored and may be revisited at a later time for a second opinion or reanalysis.

2.3.2 live cell imaging

Quantum dots have found many applications in living cells targeting and identifying membrane antigen recognition [126]. In 2002 Thomas Jovin and coworkers coupled red-light emitting (CdSe)ZnS nanocrystals to epidermal growth factor, a small protein with a specific affinity for the erbB/HER membrane receptor[127]. Maxime Dahan and coworkers similarly reported that quantum dots conjugated to an antibody fragment specific for glycine receptors on the membranes of living neurons allowed tracking of single receptors [128]. These applications have inspired the use quantum dots for monitoring other plasma membrane proteins such as integrins [129] and G-protein coupled receptors [130] .

A variety of techniques have been explored to label cells internally with quantum dots using passive uptake, receptor-mediated internalization, chemical transfection, and mechanical delivery. Quantum dots have been loaded passively into cells by exploiting the innate capacity of many cell types to uptake their extracellular space through endocytosis [131]. Quantum dots have also been successfully delivered to cells using cell-penetrating peptides such as polyarginine and HIV-1 Tat [132, 133]. Nie and coworkers used Tat peptide-conjugated quantum dots to examine the cellular uptake and intracellular transport of nanoparticles in live cells, and confirmed previous reports of a macropinocytosis internalization mechanism [29]. Recently a novel method for three-dimensional localization for tracking the three-dimensional movements of single protein-

conjugated Quantum Dots in living cell was presented by out-of-focus imaging with diffraction pattern recognition. They localize commercially available Quantum Dots in living cells with accuracy better than 7 nm over 2 microns depth [134].

2.3.3 *In vivo* animal imaging

In vivo molecular imaging using QDs has also been reported [97, 135-150].

Tumor imaging is a big challenge, not only because of cancer imaging requires high sensitive and specific contrast agents, but of because of the cancerous tissue has inherent unique biological properties. During the tumor-induced angiogenesis, the blood vessels form abnormally erratic architectures and have wide endothelial pores, which are large enough to allow the extravasation for the large macromolecules up to ~400 nm in size, thus accumulate in the tumor microenvironment [151]. This ‘enhanced permeability and retention’ effect (EPR effect) has inspired the development of many nano-therapeutics for the treatment and imaging of cancer. Also the surface receptors on the cancer cells may be used as active targets of bioaffinity molecules. In developing imaging probes, active targeting cancer antigens got a lot of attention, because it can be used to detect early cancers and their metastasis. Semiconductor QDs were very promising in these applications due to their strong fluorescent signals and multiplexing capabilities, which allow a high degree of sensitivity and selectivity in cancer imaging with multiple antigens [4].

In 2004 Nie and coworkers demonstrated that tumor targeting with quantum dots could generate tumor contrast on the scale of whole-animal imaging [152]. These nanocrystals were conjugated to an antibody against the prostate-specific membrane antigen (PSMA), and were intravenously injected into mice bearing subcutaneous human prostate cancers [6]. Since that work, there have been a number of exciting studies showing the utility of QDs as *in vivo* imaging agents. Using similar methods, Ququan Wang and coworkers were able to actively target and image mouse models of human

liver cancer using quantum dots conjugated to an antibody against alpha-fetoprotein [153], and the group of Xiaoyuan Chen showed that labeling quantum dots with RGD peptides significantly increased their uptake in human glioblastoma tumors [154].

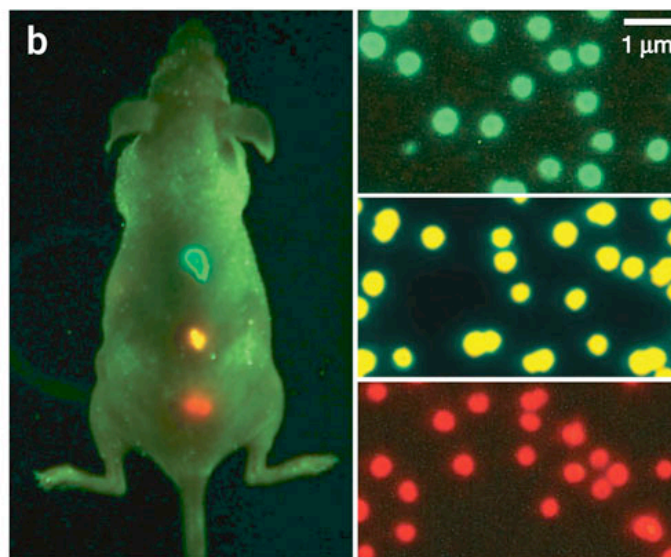


Figure 2.7. Simultaneous *in vivo* imaging of multicolor QD-encoded microbeads. (From Gao et.al. [6])

2.3.4 Challenges and opportunities

Many concerns have been raised over the application of quantum dots in living cells and animals due to their chemical composition of toxic heavy metals like Cd. Some studies have indicated that the cytotoxicity of QDs strongly correlates with the stability and surface coatings of these nanoparticles and many preliminary studies have shown that toxicity issues for QDs *in vivo* are of some concern [6, 31, 37, 38]. Although this could eventually prevent their use *in vivo*, immunohistological and cellular and tissue staining is performed on *in vitro* or *ex vivo* clinical samples, where heavy metal toxicity is consequential. As a result, the use of multicolor QD probes for tissue staining and biomarker detection is likely one of the most important and clinically relevant applications in the near term [32, 155].

The applications of quantum dots in biomedicine span a broad range of length scales and address a lot of clinical and biological sensing needs. Despite the many assets of these probes, many challenges must be overcome. The colloidal and surface properties of these nanoparticles must be optimized in order to maximize their stability, minimize nonspecific binding, and minimize their size. For biomedical applications, ideal QDs should not only have good water solubility, high stability, minimized cell toxicity, but also have abundant functional groups such as amine ($-\text{NH}_2$) and carboxyl ($-\text{COOH}$) groups for further conjugation toward specific targeted imaging.

In the future, the major goal for bio-nanotechnology is to develop complex biological probes and agents that can be used to monitor and specifically manipulate biological systems, most importantly for medical applications. The nanocrystal probes designed from quantum dot backbones have already reached an impressive level of layered complexity, and probes with multimodal imaging and drug delivery capabilities are in development [12, 17, 143, 156-188]. They have been the topic of many efforts to develop probes that are detectable by both optical imaging and other modalities such as PET or MRI [21], such as lipid-coated multimodality QDs [58, 59], doped QDs with Mn into the core matrix of the QDs [22, 60], and QDs conjugates with DOTA and DTPA to the surface to metalate PET or MRI active molecules [55-57, 189]. Increasing the precision, dimensionality, and multimodality of these particles may generate great advances throughout biomedical fields, such as for cancer detection, profiling and treatment and even for other diseases.

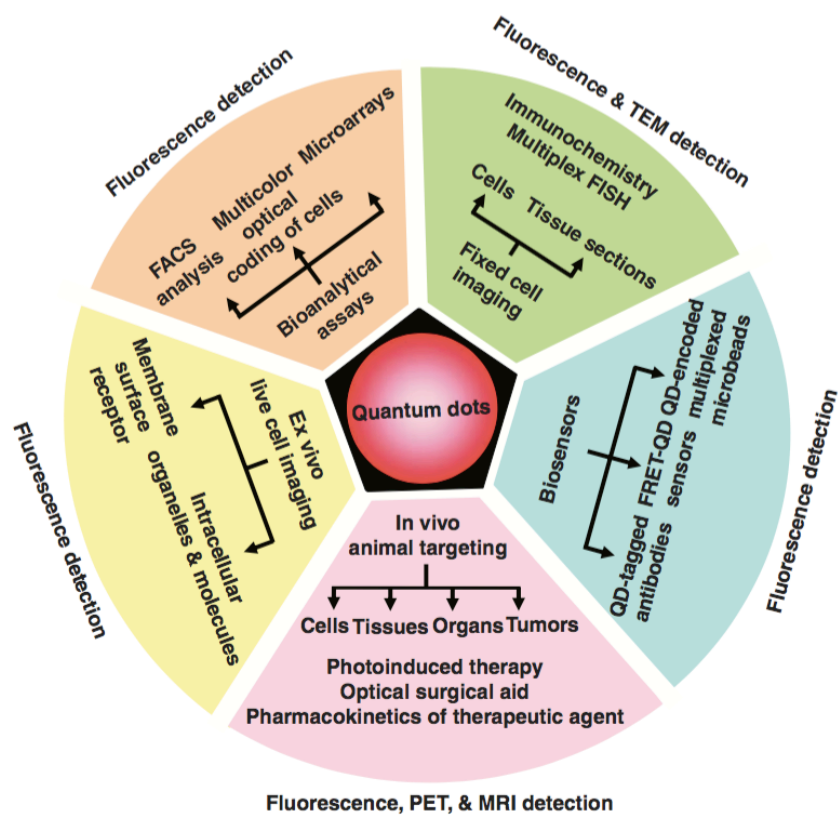


Figure 2.8. Applications of quantum dots as multimodal contrast agents in bioimaging (from X. Michalet et al. [7])

CHAPTER 3

BIOCOMPATIBLE HYALURONIC ACID-CYSTAMINE POLYMER COATED QDS FOR CANCER CELL IMAGING

Abstract

The cysteamine-modified hyaluronic acid (HA) polymer was employed to coat quantum dots (QDs) through a convenient one-step reverse micelle method, with the final QDs hydrodynamic size of around 22.6 nm. The HA coating renders the QDs with very good stability in PBS for more than 140 days and resistant to large pH range of 2–12. Besides, the HA-coated QDs also show excellent fluorescence stability in BSA-containing cell culture medium. In addition, the cell culture assay indicates no significant cytotoxicity for MD-MB-231 breast cancer cells, and its targeting ability to cancer receptor CD44 has been demonstrated on two breast cancer cell lines. The targeting mechanism was further proved by the HA competition experiment. This work has established a new approach to help solve the stability and toxicity problems of QDs, and moreover render the QDs cancer targeting property. The current results indicate that the HA polymer-coated QDs hold the potential application for both in vitro and in vivo cancer imaging researches.

3.1 HA applications and the mechanism for targeting CD44 receptor

3.1.1 Hyaluronic Acid

Hyaluronic acid (HA) is a glycosaminoglycan, which presents in the extracellular matrix of many parts of the body cell. As an important biological material, HA has a very wide range of applications in different fields, such as tissue culture scaffolds and

cosmetic materials [190]. Here we describe the structure and properties of HA and give several examples on the applications of HA in tissue engineering and nanocarriers for controlled delivery.

HA structure and properties

Hyaluronic acid is an anionic, non-sulfated, linear polysaccharide which consists of disaccharide units of d-glucuronic acid and N-acetyl-d-glucosamine linked together by β -1,4 and β -1,3 glycosidic bonds, as shown in Figure 3.1 [8].

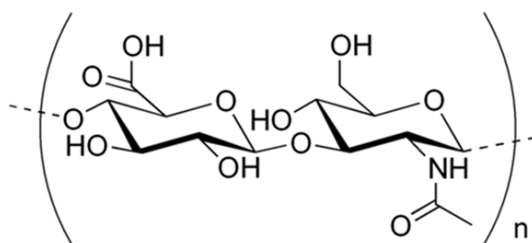


Figure 3.1. The structure of HA

HA can be extracted from animal products or produced by bacterial fermentation (such as *Bacillus subtilis*) to obtain controllable molecular weight. It exists in the synovial fluid and natural extracellular matrix and is an important component of connective tissue, epithelial tissue, and nerve tissue. In addition, HA is biocompatible and hydrophilic and can form a lower concentration of viscous solution, which promotes wound healing by promoting cell migration and proliferation. Moreover, HA can be degraded by hyaluronidase and reactive oxygen species in mammals, producing low molecular weight HA and oligosaccharides. HA can interact with several cell surface receptors such as CD44, CD54 and CD168 which makes it very popular in a lot of controlled delivery applications [8].

Application of HA in tissue engineering

The scaffold is a temporary supporting structure for growing cells and tissues by definition and also called synthetic extracellular matrix, which plays an important role in

supporting cells [191]. HA offers many advantages as a tissue scaffold. First, it is biodegradable, biocompatible and is a major component of connective tissues that play an important role in cell differentiation and growth. Second, HA has a lot of functional groups such as carboxylic acids and hydroxyl groups which can introduce functional domains to form hydrogel by crosslinking. Thirdly, HA has low non-specific adsorption of proteins, and they can have specific interactions between the scaffold and growing cells through cell receptors such as CD44 and RHAMM to facilitate tissue growth and repair [190].

The development of 3D cellular scaffold in tissue engineering has been intensively studied in recent years. Because HA has a lot of functional groups such as carboxylic acid, hydroxyl groups and N-acetyl group, it offers a lot of strategies for HA photopolymerization. The photocrosslinkable HA hydrogels can be formed through the covalent carboxylic acid or hydroxyl groups by reacting the polymer with functional groups, such as methacrylates under homogeneous (such as water) or heterogeneous (e.g., water/DMSO) conditions [8]. As shown in Figure 3.2A, a versatile bioink for 3D printing of high-resolution scaffolds was developed. The scaffolds were based on thermal- and photo-triggered tandem gelation through the blending of thermos-responsive polymer poly (N-isopropylacrylamide) grafted hyaluronan (HA-pNIPAAm) and methacrylated hyaluronan (HAMA) and scaffolds of good viability can be printed by this novel method.

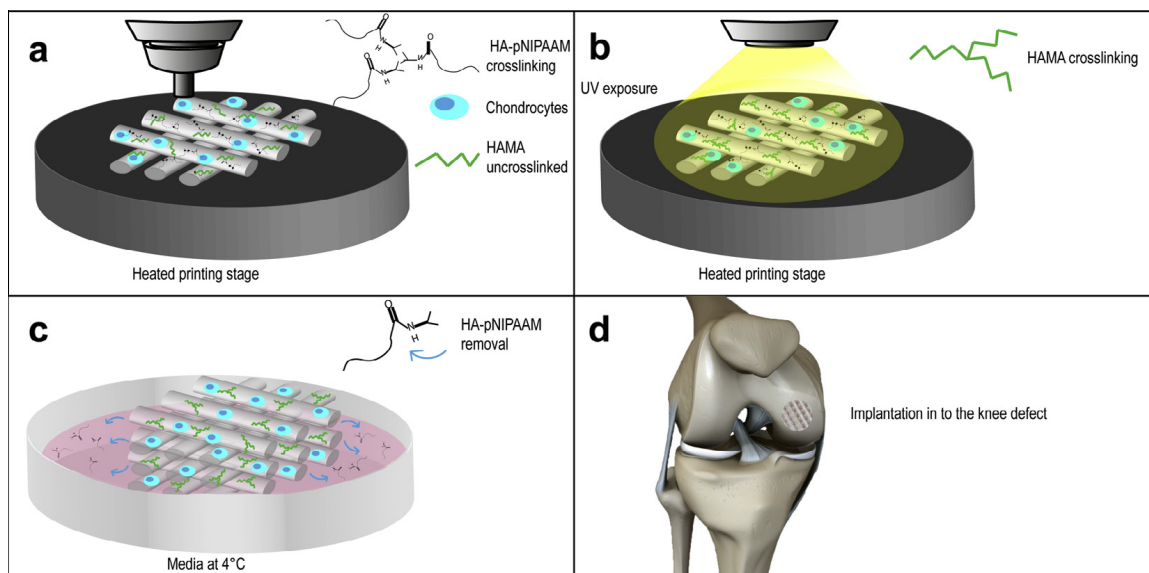


Figure 3.2. Schematic illustration of HA-based 3-D constructs for cartilage engineering. (from Pereira et al. [8])

HA-based nanocarriers for controlled delivery

Among the several drug delivery materials that was using now, polysaccharides are a kind of attractive molecules because they can undergo a large range of chemical modifications and they are biocompatible, biodegradable, and have relatively low immunogenicity. Therefore, polysaccharides have been widely used in delivery of many types of drugs [9]. There're a lot of advantages for the conjugation of chemotherapy drugs to macromolecules, as shown in Figure 3.3. Macromolecules help to improve the drugs' pharmacodynamics (PD) and pharmacokinetics (PK) by different mechanism. For the PD aspect, macromolecules have a high drug loading ability and also can conjugate targeting molecules to improve the specificity of the drugs. As for the PK aspect, macromolecules can increase the blood circulation time and reduce the volume of distribution. Also, the bigger size of the polymer–drug conjugates can get to the tumor sites due to the enhanced permeability and retention (EPR) effect.

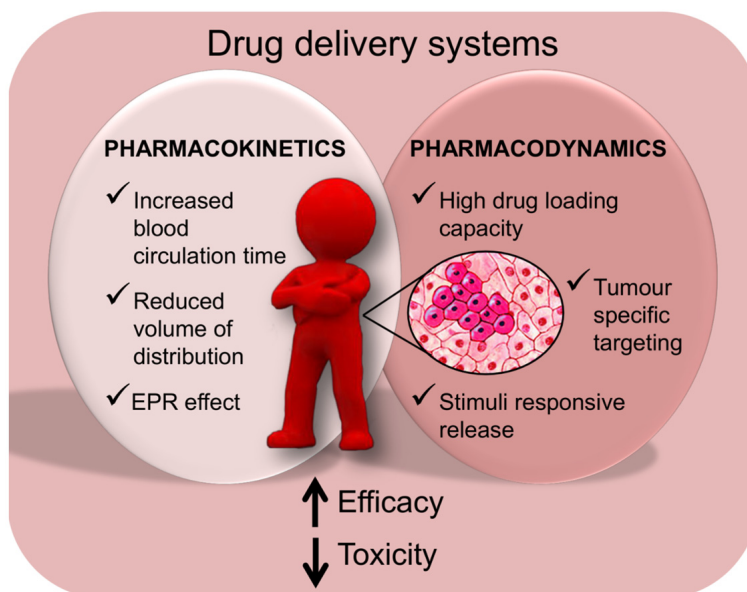


Figure 3.3 Advantages of drug delivery systems of chemotherapy agent conjugated with macromolecules (from Posocco et al. [9])

Hyaluronic Acid conjugates have been used as nanovectors for drugs, genes and nanocomposite for the active targeting in cancer diagnosis and treatment [192].

Hyaluronic acid receptor CD44 is found to overexpress in many cancer cells, particularly in tumor-initiating cells, whereas lower level of CD44 receptors are found on the surface of other non-tumor cells, such as epithelial, hematopoietic, and neuronal cells. Therefore, HA has attracted a lot of interest in the development of novel drug delivery systems in different types of nanovectors, serving as targeting ligand in preparation of actively targeted nano-platforms for a lot of genes, drugs, and diagnostic agents [192].

HA has been widely used in RNAi delivery due to its great advantages mentioned above. Development of nontoxic, tumor-targeting, and *in vivo* RNAi delivery system was usually a hard work. In a study as shown in Figure 3.4, the researchers developed a versatile RNAi nanoplatform which is based on a tumor-targeting and pH responsive RNA nanocarrier [10]. This nanoplatform for RNA delivery contains four components which are a hydrophilic HA shell as CD44-targeting ligand, hydrophobic 5 β -cholanic

acid (CA) core as drug reservoir, phosphate receptor Zn(II)-dipicolylamine (DPA/Zn) as RNA binding site and a calcium phosphate layer. The nanocarrier can distribute the RNAs into the cytoplasm of the cancer cells uniformly and selectively suppress the target gene expression. This nanoplatform can serve as a versatile delivery system for RNAi applications, and this work may open up new possibilities for RNA-based cancer treatments and therapeutics.

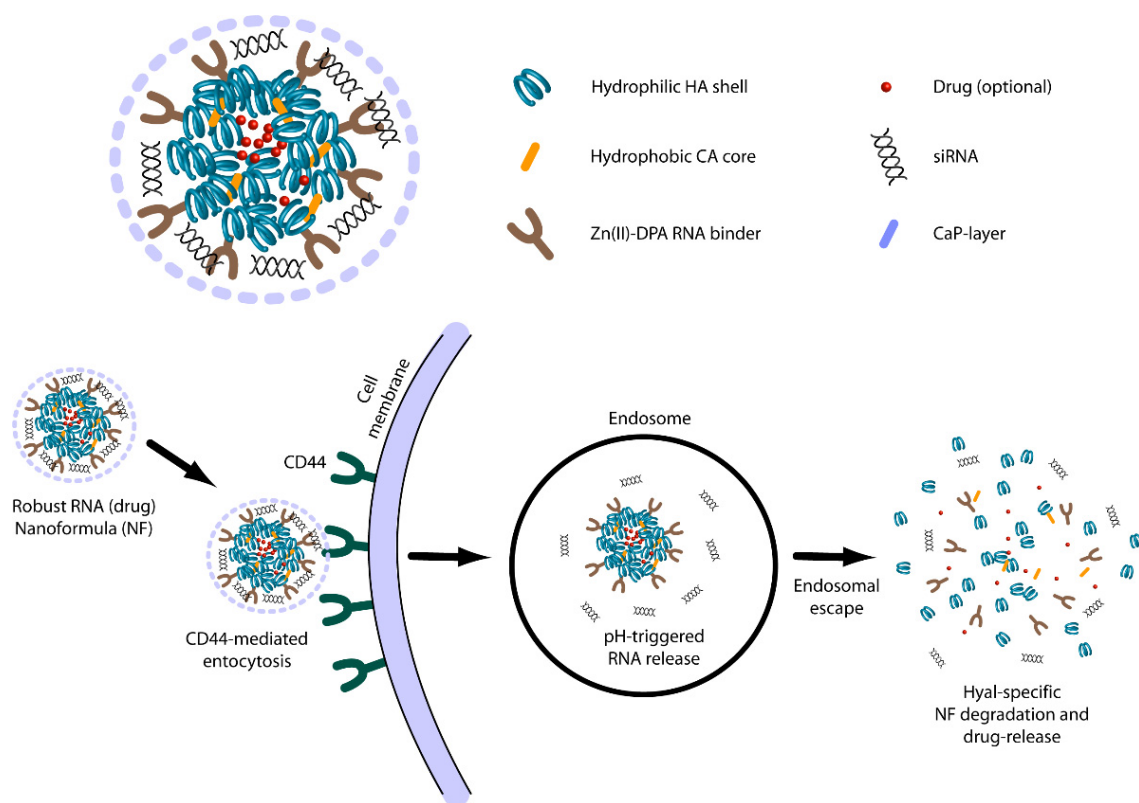


Figure 3.4. HA-based RNAi delivery nano-platform for siRNAs (from Choi et al. [10])

3.1.2 CD44 receptor

CD44 is a single chain glycoprotein and a multi-structural and multi-functional cell surface molecule. CD44 involves in a lot of cell activities, such cell proliferation and differentiation, cell migration, angiogenesis, presentation of cytokines, chemokines, and

growth factors to the corresponding receptors, and the docking of proteases at cell membrane, and in the signaling for cell survival. The discovery that CD44 receptor is crucial on many tumor cell activity has given new hope in the scientific and medical research. Its multi-structural and pleotropic nature was revealed by the biochemical characterization, allows the targeting of malignant cells, which express CD44 receptors. The principal ligand of the CD44 receptor is hyaluronic acid and CD44 can be activated by fragmented HA (molecular mass $<5 \times 10^5$ D), but not the high molecular mass HA ($>10^6$ D) [193].

CD44 can mediate the internalization and metabolism of HA, and various cell types in normal tissues have low levels of endogenous expression, but it needs to be activated before they can bind HA [194]. CD44 can transit from the inactive, low-affinity state to an active, high-affinity state after cell activation such as antigen receptors ligation, sulfation, or the action of cytokines and will be capable of binding HA. Unlike normal cells, tumor-derived cells express the high-affinity state of CD44, thus is capable of binding and internalizing HA. Furthermore, CD44 is reported to interact with HA of minimum length of 6–8 saccharide units [195]. Therefore, there are several possible strategies for cancer treatment, such as interference with the HA-CD44 interaction, targeting drugs to CD44 or HA matrix.

CD44 involves in many pathways such as activation of cell cycling and proliferation, cytoskeleton reorganization, cell migration and maintenance of cell survival, which are highly related with the malignant process, therefore, CD44 is associated with aggressive type of tumors in many cases. There is an upregulation of CD44 in many cancers of epithelial origin [65]. Overexpression of CD44 isoforms in malignant tissues has been already detected in some of the patients compared with the control counterparts, in several diseases including breast and colorectal malignant tissue, lung cancer (squamous cell carcinoma; adenocarcinoma; large cell carcinoma; small cell

carcinoma), hepatocellular carcinoma, renal cell carcinoma, gallbladder carcinoma, ovarian (mostly clear cell) carcinoma, endometrial cancer and melanoma [193].

In conclusion, CD44 can be a promising targeting molecule for the therapy and diagnosis of several human cancers [193]. HA has already been used as drug carrier and ligand on liposomes or nanoparticles to target the drugs to CD44 overexpressing cells. The drugs can be attached to HA through the carboxyl group on the glucuronic acid residue or the hydroxyl group on the N-acetylglucosamine [65]. HA targeting will increase drug accumulation in the CD44 overexpressing cells and HA conjugated drugs can enter the cells via endocytosis.

3.1.3 HA-based CD44 targeted imaging using QDs

A number of work has been done using QDs for HA-CD44 targeted imaging. Hahn's group has reported a series of work using adipic acid dihydrazide-modified HA to conjugate commercial carboxyl Quantum Dots for *in vivo* imaging, and found that lower carboxyl-modified HA (i.e., 35, 22 %) kept the targeted ability for HA receptors in liver, while higher modification ratio (i.e. 50, 68 %) of HA will lose much of HA targeting ability [11, 196-198].

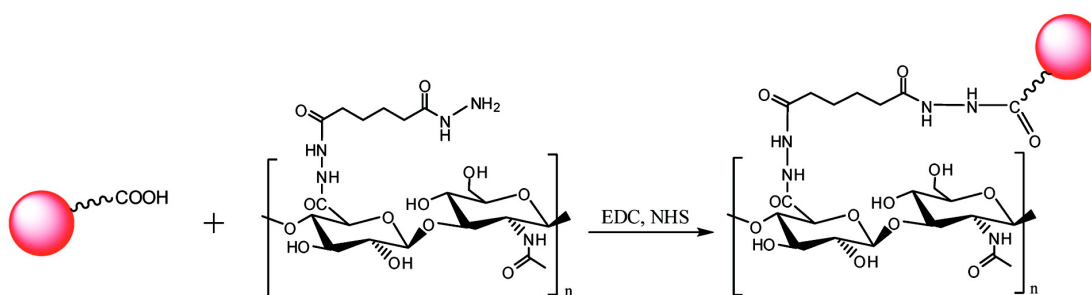


Figure 3.5. Synthesis of a hyaluronic acid-quantum dot (HA-QDot) conjugate using adipic acid dihydrazide-modified HA (HA-ADH) (from Kim et.al. [11])

Graphene quantum dot (GQD) has also been conjugated with hyaluronic acid (HA) (GQD-HA) as a targeting agent and *in vitro* cellular imaging exhibited strong

fluorescence from CD44 overexpressed A549 cells. *In vivo* investigation on CD44 receptor overexpressed tumor-bearing balb/c female mice also demonstrated more bright fluorescence from the tumor tissue [199].

Fluorescent nanosized carbon dots (Cdots) were also reported for the application of real time bioimaging of target specific delivery of hyaluronic acid (HA) derivatives. Polyethylene glycol (PEG) diamine-capped Cdots were synthesized for HA-Cdot conjugates by amide bond formation between amine groups of Cdot and carboxylic groups of HA. *In vitro* bioimaging was realized for target specific intracellular delivery of the HA-Cdot conjugates through HA receptor-mediated endocytosis. Furthermore, *in vivo* real-time bioimaging of Cdots and HA-Cdot conjugates proved the target specific delivery of HA-Cdot conjugates to the liver with abundant HA receptors [200]. Those work in previous studies are good examples for the application of QDs in HA-CD44 targeted imaging.

3.2 Materials and Methods

3.2.1 Materials

Chemicals and instruments

Sodium hyaluronate with MW of 7500 was purchased from Lifecore (USA). Cystamine dihydrochloride, dithiothreitol (DTT), cyclohexane, IGEPAL CO-520, tetramethylammonium hydroxide (TMAH), ethylene- diaminetetraacetic acid (EDTA), and Ellman's reagent were purchased from Sigma-Aldrich. EDC, sulfo-NHS, and cysteine hydrochloride monohydrate were purchased from Pierce. UV-Vis absorption spectra were obtained using a Cary 100 Bio UV-Visible Spectrophotometer from Varian Company. Photoluminescence spectra were recorded by a Fluoromax 2 spectrofluorometer. Dynamic light scattering measurements were performed on a Brookhaven 90Plus Particle size analyzer. Transmission electron microscopy was performed on a Hitachi H-7500 TEM at the Electron Microscopy Core Facility at Emory

University. 96-well plates were read by a Synergy 2 Multi-Mode Microplate Reader (Biotek, USA).

3.2.2 Methods

Synthesis of HA-cysteamine polymer

The synthesis of HA-cysteamine polymer involves two steps: synthesis of HA-cysteamine polymer and reduction of the disulfide bond of cysteamine by DTT. Typically, sodium hyaluronate with average MW of 7500 was dissolved in PBS, then 18 molar excess of EDC and 18 molar excess of sulfo-NHS were added to the HA sodium salt solution, and the mixture was stirred for 1 h to activate the carboxyl groups. Then 12 molar excess of cysteamine dihydrochloride in PBS was added dropwise while stirring, and the mixture was kept reacting overnight. The HA-cysteamine product was purified by dialyzing against 1X PBS buffer using MWCO 3500 dialysis tube. For DTT reduction of the disulfide bond on cysteamine, 5 molar excess of DTT was added to HA-cysteamine solution and stirred for 24 h. The final product was purified by dialyzing against pH 3 buffer using MWCO 3500 dialysis tube. The water was removed by lyophilizing for 2–3 days. Finally cotton-like HA-cysteamine polymers were obtained. The final product should be stored at -20 °C to protect the active thiol groups from being oxidized.

Determination of reactive thiols on HA-cysteamine polymer

The sulfhydryl group concentration on HA-cysteamine polymer was determined via Ellman's reagent by comparing to a standard curve composed of known concentrations of cysteine. Namely, 0.1 M sodium phosphate buffer of pH 8 containing 1 mM EDTA was prepared as reaction buffer. 4 mg Ellman's Reagent was dissolved in 1 ml of reaction buffer as Ellman's reagent solution. A set of cysteine standards were prepared by dissolving cysteine hydrochloride monohydrate at concentrations of 0, 0.25, 0.5, 0.75, 1, 1.25, and 1.5 mM in reaction buffer. 250 µl of each cysteine standard or HA-cysteamine polymer of known weight was added to separate test tubes, which contain 50

μl of Ellman's reagent solution and 2.5 ml of reaction buffer. The mixture was incubated at room temperature for 15 min. Then the absorbance at 412 nm was measured using a plate reader and the standard curve was plotted. Finally, the active thiol group concentration of the HA-cysteamine polymer was determined accordingly.

Synthesis of (CdSe)CdZnS QDs and encapsulation with HA-cysteamine polymer

(CdSe)CdZnS QDs of 645nm emission wavelength were synthesized following previous methods [87, 201]. When encapsulating QDs with HA-cysteamine polymer, a modified reverse micelle method was used [94, 202]. Typically, 0.64 nmol QDs in hexane was dried by vacuum to get a thin film, then 9 ml cyclohexane was added until the QDs was fully dissolved. Next 1 ml IGEPAL CO-520, 10 mg HA-cysteamine polymer in 500 μl water and 3.61 mg TMAH in 200 μl methanol were added to form reverse micelle. The solution should be clear after adding all these reagents. If not clear, add more IGEPAL CO-520 or water. The mixture was sonicated for 5 min, and vortexed for 60 min. Then 1-2 ml ethanol was added to precipitate the HA-cysteamine polymer coated QDs. The pellets was washed with additional ethanol for 3 times and re-dispersed in 1X PBS. After centrifuging the QDs solution at 5000 g for 10 minutes to get rid of the undissolved parts, the supernatant which contains the HA-cysteamine coated QDs was purified using a 0.2 μm syringe filter.

pH stability test

An "universal" pH buffer, Britton–Robinson buffer with pH range from 2 to 12 were prepared [203]. Then a same amount of concentrated QDs were added to each pH solution. The QDs solution were added in fluorescence testing tubes and sealed well with parafilm. After 1 h, 16 h and 24 h incubation at room temperature, the photoluminescence of QDs were recorded by a fluorometer and integrated intensity was calculated for comparison. The fluorescence intensity of QDs in pH 7 buffer after 1h incubation was referenced as 1, and others were scaled as certain percent ratio. The corresponding

fluorescence images of QDs after 24 h incubation were taken by illuminating with a 365 nm hand-held UV lamp.

Long-time stability test

Long-time stability of the HA-polymer coated QDs was tracked for 5 months and compared with mercaptoacetic acid (MAA) coated QDs. Typically, 300 μ L HA-polymer coated QDs in 1X PBS buffer at a concentration of 25 nM was added in a fluorescence testing tube and sealed well with parafilm. The QDs containing tube was stored in 4°C refrigerator and the fluorescence intensity was tested on certain days. To prepare MAA-coated QDs, 150 μ L QDs of 10 nM in crude stock were precipitated with 13 ml acetone. The pellets were washed with acetone and re-dispersed in 1 ml chloroform. 500 μ L MAA and 100 mg TMAH in 500 μ L methanol were added. The whole solution was sonicated for 10 min and kept at 60°C water bath for 1 h. The QDs were precipitated with acetone by centrifuge at 8000 g for 10 min, washed with acetone and dissolved in 1X Borate buffer. The QDs were dialyzed against 50 mM borate buffer (pH 8.5) using 20K MWCO dialysis tube, and then stored at 4°C in the dark. The fluorescence intensity was integrated for each spectrum and compared with the first day's result.

Cell culture medium stability test

The stability of HA-QDs in cell culture medium was tested and compared with the commercial carboxyl 655 nm QDs from Invitrogen. Typically, the HA-QDs and 655 nm carboxyl QDs from Invitrogen were diluted in PBS or DMEM phenol-red free medium with 10% fetal bovine serum (FBS) added. The QDs were sealed and put under room temperature without any protection from light. At 0 h, 1 h, 16 h and 24 h, the fluorescence of these QDs were tested and integrated. The integrated fluorescence intensity of each QDs in PBS at 0 h were set as 1 and all results were referenced to get certain percent ratio.

Cytotoxicity test

MD-MB-231 breast cancer cell line was cultured in RPMI 1640 with 10% FBS and 1% streptomycin and penicillin antibiotics. On the first day, cells were seeded on a 96 well plate at 5×10^3 cells/well. After 24 h culture, QDs were added to the 4, 10 and 25 h incubation time group with the final concentrations of 1, 5, 10 and 20 nM. For the control group, cells of same number were seeded but no QDs were added. This is regarded as 100% cell viability. A blank control with no cells and QDs but only cell culture medium was used as 0% cell viability. Experiments were triplicated. After incubation with QDs, the medium was aspirated and 100 μ l of new cell culture medium and 10 μ l Cell Counting Kit-8 solution was added to each well. Following incubation with cells at 37°C for 3 h, the absorbance at 450 nm was measured by a plate reader.

Cancer cell targeted imaging

CD44⁺ MD-MB-231 and MCF-7 breast cancer cells were used for targeted imaging and NIH/3T3 fibroblast cell was used as a negative control. Due to the different growth speed, NIH/3T3 fibroblast cells were seeded at 3500 cell/well and MD-MB-231 and MCF-7 breast cancer cells were seeded at 25×10^3 cell/well on 8-well chamber slides. After 24 h growth, cells were washed with 1X PBS buffer and then fixed with 200 μ l 4% formaldehyde and 0.25% Triton X-100 in PBS for each well. After 15 min, cells were washed with PBS for 5 min, three times. 200 μ l blocking buffer of 6% bovine serum albumin (BSA) in PBS were added to each well and incubated for 1 h. Then blocking buffer was aspirated and 200 μ l HA-cysteamine polymer coated QDs were added to each well, with final concentrations of 1, 5, 10 and 20 nM in blocking buffer. After 1 h incubation, each well was washed with PBS three times for 5 min each. The slides were mounted with anti-fade mounting media containing DAPI. The slides were imaged under Olympus IX71, using 20X objective.

Hyaluronic acid competitive inhibition test

MCF-7 cells were seeded on an 8-well chamber slide at 30 k/well for overnight growth. The fixation, permeabilization and blocking procedure are the same with the

targeted imaging experiment. Before adding QDs, different concentrations of 200 μ l HA in blocking buffer were added to each well for 1 h. HA concentrations used are 0 nM (as control), 10 nM, 100 nM, 1 μ M, 10 μ M, 100 μ M, 1 mM and 10 mM. Then HA solution was aspirated and 200 μ l QDs at final concentration of 10 nM in blocking buffer were added to each well. After 1 h incubation, the QDs was washed with PBS and mounted, and the slide was imaged under Olympus IX71, using a 20X objective.

3.3 Results and Discussions

3.3.1 Results

Synthesis and characterization of HA-cysteamine polymer

As shown in Figure 3.6(a), the amine group of cysteamine was first covalently conjugated to the carboxyl group on HA using EDC and sulfo-NHS. Then the disulfide bond of cysteamine was further reduced with DTT to get the final HA-cysteamine polymer. Each polymer molecule contains approximately 8 active thiols, as determined via Ellman's method. Averagely, an HA molecule with MW 7500 contains about 19 carboxyl groups, therefore about 42% carboxyl groups on HA have been converted to thiol groups. This thiol modification ratio can ensure strong binding of the HA polymer on QDs surface and also, a large amount of carboxyl groups are left to maintain the HA targeting ability for CD44 receptor on cell surface.

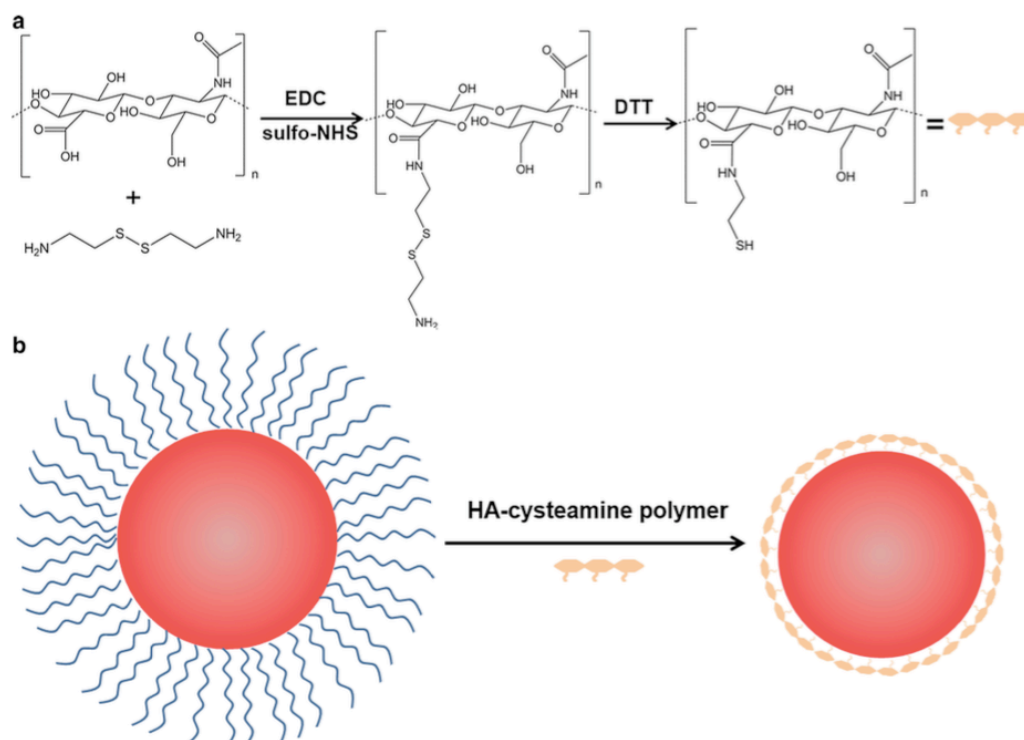


Figure 3.6. Preparation of HA-cysteamine polymer-coated QDs. (a) The chemical synthesis of HA-cysteamine polymer. (b) Schematic illustration of HA polymer coating on QDs

Preparation and characterization of HA-cysteamine polymer coated QDs

Polymer coated QDs were synthesized using an adapted reverse micelle method for ligand exchange and phase transfer reaction [94, 202] as shown in Figure 3.6(b). Hydrophobic QDs protected with oleylamine on surface was synthesized by traditional methods. [87, 201] For ligand exchange, the hydrophobic QDs were first dispersed in cyclohexane. With the addition of IGEPAL CO-520 and HA-cysteamine polymer dissolved in water, a reverse micelle was formed. TMAH was used as a phase transfer catalyst to induce the reaction. After the reaction, water soluble QDs coated with HA-cysteamine polymer were incorporated inside the reverse micelle.

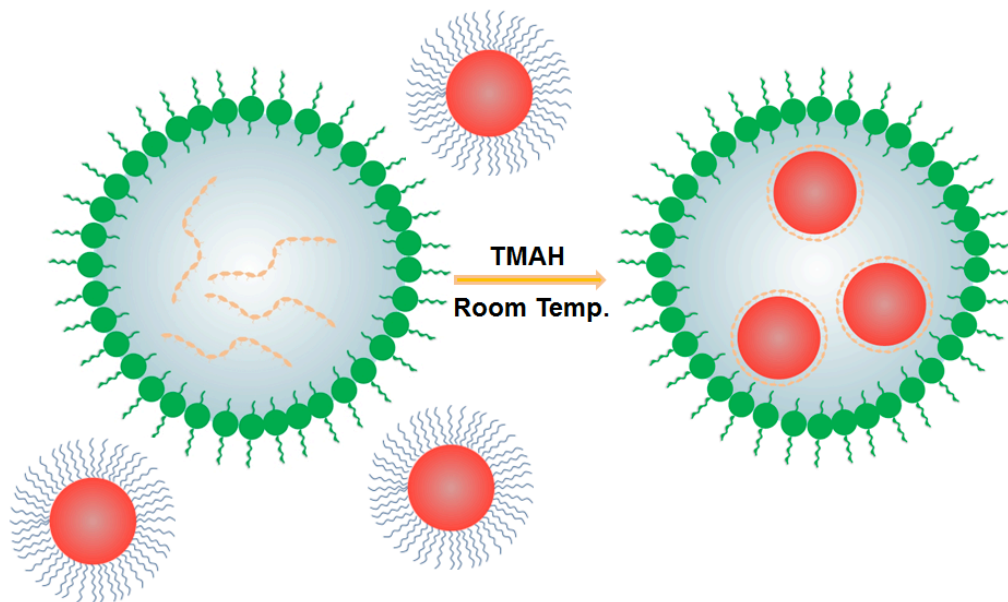


Figure 3.7. Schematic illustration of reverse micelle phase transfer procedure for HA-cysteamine polymer coated QD synthesis.

Figure 3.8(a-b) show representative transmission electron microscopy (TEM) images of QDs before and after polymer coating. Both of them appear uniform in size and were well dispersed. Figure 3.8(a) shows the crystal size of QDs before polymer coating is 9.5 ± 1.3 nm. Negative staining TEM with 1% methylamine tungstate clearly shows polymer coated QDs with a thin layer as shown in the inserted plot of Figure 3.8(b) and the overall size of HA coated QDs is 14.5 ± 1.6 nm. Figure 3.8 (c-d) show UV absorption and fluorescence spectra before (Figure 3.8(c)) and after (Figure 3.8 (d)) the HA polymer coating. We can see that there is no significant difference between the 2 sets of spectra. Quantum yield (QY) calculation was 24% after coating while the QY of QDs in hexane before coating is 28.1%. The QY didn't lose much after polymer coating, which proves a good surface protection and passivation. The dynamic light scattering (DLS) results (Figure 3.8 (e)) show that the hydrodynamic size of the compact polymer coated QDs is around 22.6 ± 5.2 nm.

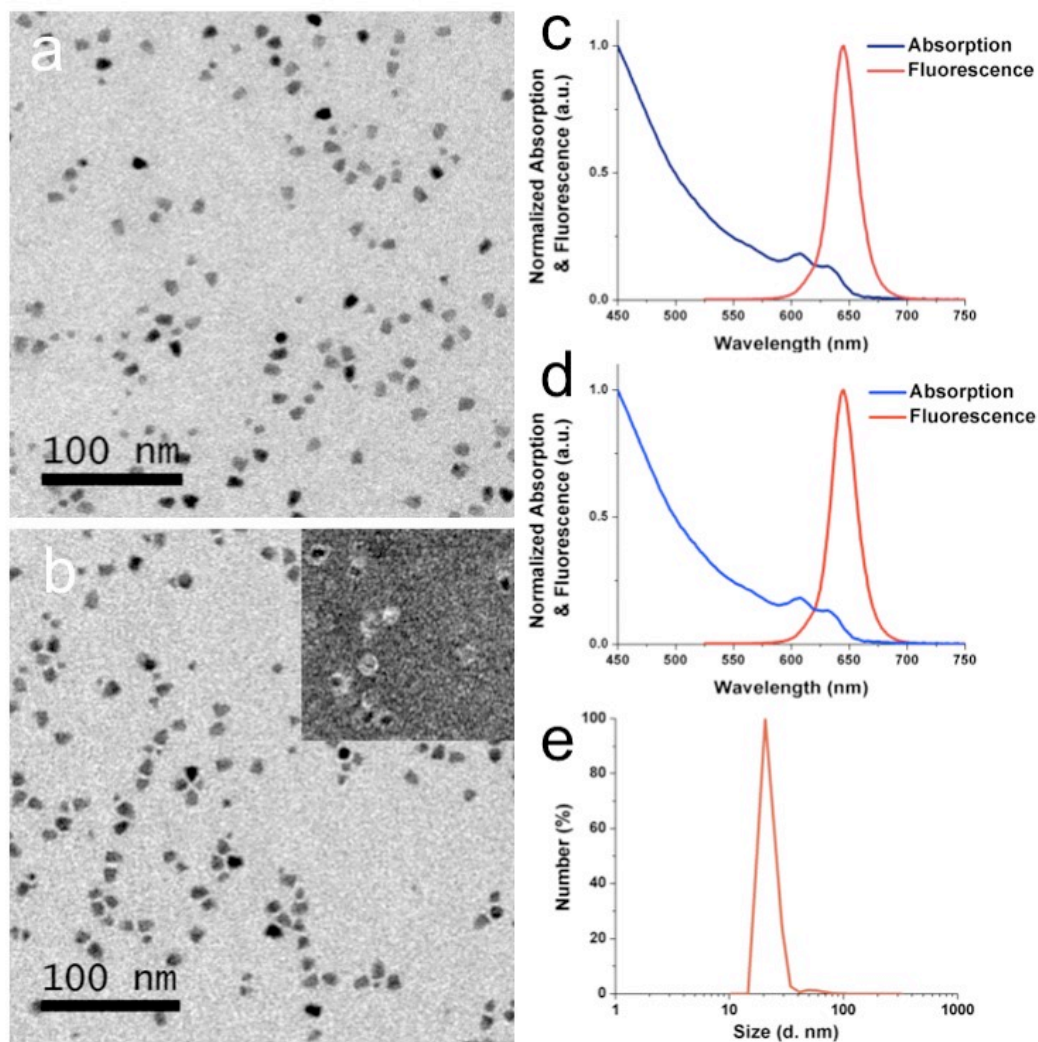


Figure 3.8. Characterization of QDs. (a) TEM image of QDs in hexane (before polymer coating). (b) TEM images of HA-cysteamine polymer coated QDs in water. Negative staining TEM is inserted with the same scale bar, showing the polymer coating layer. (c) Absorption and fluorescence spectra of QDs in hexane (before polymer coating). (d) Absorption and fluorescence spectra of QDs after HA-cysteamine polymer coating, showing no significant difference with the spectra before polymer coating. (e) DLS size distribution showing a peak hydrodynamic diameter of ~ 22.6 nm

To exclude the possibility that the hydrophobic part of IGEPAL CO-520 intercalate into oleylamine on QD surface, and the hydroxyl groups render QDs water soluble, control experiment without adding HA-cysteamine polymer was conducted. The

final QDs pellets cannot dissolve in water, which proved that it is HA polymer rather than IGEPAL CO-520 that makes QDs water-soluble.

pH stability test

The colloidal stability of HA-cysteamine polymer coated QDs in different pH buffer from 2 to 12 was tested. As shown in Figure 3.9 (a), the polymer coated QDs keep great fluorescence performance even after as long as 24 h incubation with the extreme pH condition. The QDs have better fluorescence performance in basic buffer than in acidic buffer. As the incubation time increases at each pH, integrated fluorescence in acidic buffer gradually decreases while in basic buffer it increases. This is reasonable considering the HA has unmodified carboxyl groups, which makes them more soluble in basic solution. However, we can see from Figure 3.9 (b), that after 24 h incubation the QDs didn't precipitate or aggregate and still keeps great colloidal and photo stability even for as long as 24 h incubation with pH range from 2-12. This indicates that the QDs can adapt to the complex body environment of different pH changes, and they can be good candidates as intracellular and *in vivo* imaging probes for long time tracking.

Long-time stability test

Long-time stability of the HA-polymer coated QDs was tracked for 5 months. For the same vial of 25 nM QDs in 1X PBS buffer stored at 4°C, the integrated fluorescence intensity didn't drop much even after as long as 140 days, while a control group using MAA coated QDs stored at the same condition precipitated within 11 days, as shown in Figure 3.10. The HA-polymer coated QDs shows great long time stability comparing with the single thiol MAA coated QDs. This is a good example showing the necessity of using multi-thiol polymer coating.

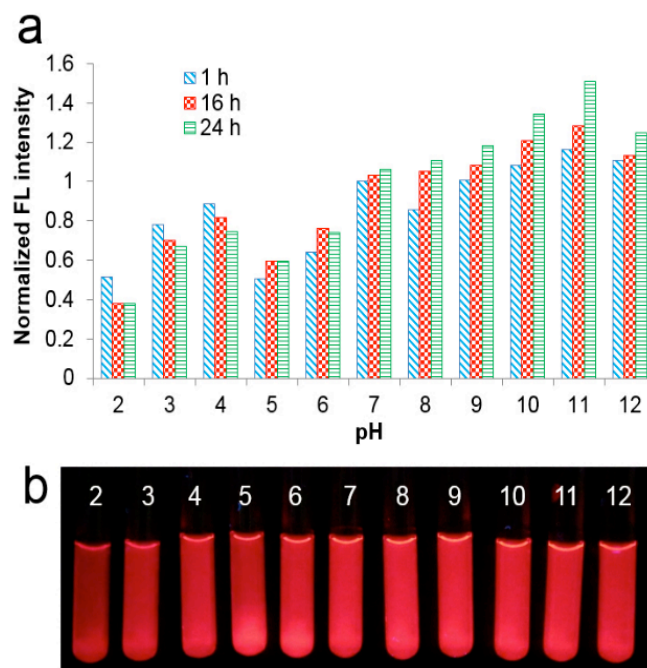


Figure 3.9. pH stability of HA-cysteamine polymer coated QDs. (a) Normalized integrated fluorescence intensity after incubating for 1 h, 16 h and 24 h in different pH buffer. The fluorescence intensity of QDs in pH 7 buffer after 1 h incubation was referenced as 1. (b) Corresponding fluorescence images of QDs after 24 h incubation (illuminated with a 365 nm hand-held UV lamp)

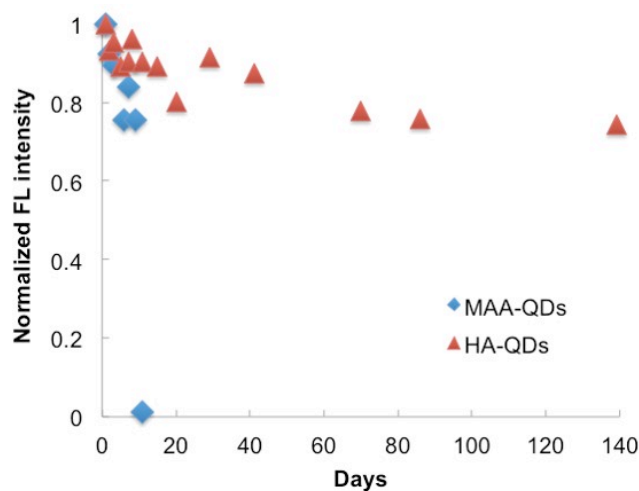


Figure 3.10. Long-time stability of HA-cysteamine polymer coated QDs, compared with MAA coated QDs. The MAA coated QDs precipitated after 11 days thus lose its fluorescence totally

Stability in cell culture medium

The QDs stability in FBS containing cell culture medium is very important for further cellular and even *in vivo* imaging applications. If the fluorescence of QDs is easily influenced by the cell culture medium, then stable and quantitative continues imaging is challengeable. The results of the HA polymer coated QDs were shown in Figure 3.11 (a). We can see that those QDs keeps excellent fluorescence stability in cell culture medium at room temperature without any protection from the light, and the stability of our HA polymer coated QDs are comparable to the commercial carboxyl QDs from Invitrogen (Figure 3.11 (b)). The results proved the great cell culture medium stability of the QDs and showed the possibility for further cellular applications.

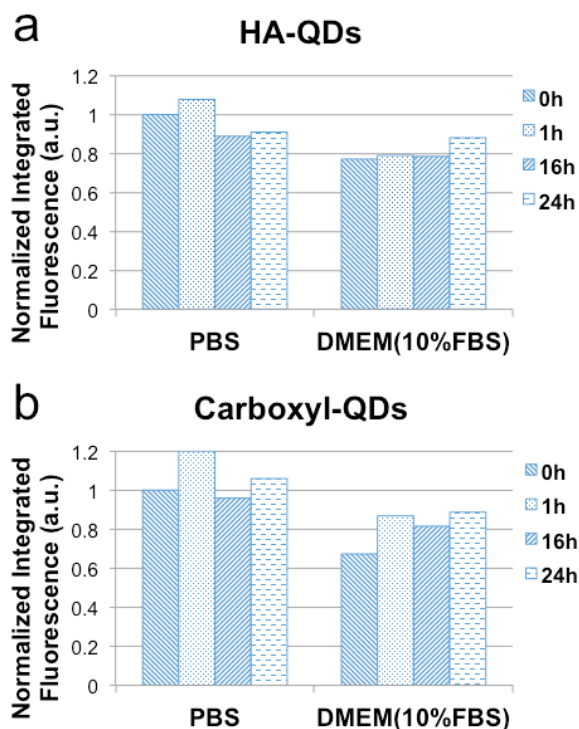


Figure 3.11. Stability in cell culture medium of HA polymer coated QDs and commercial carboxyl QDs from Invitrogen

Cytotoxicity test

MD-MB-231 breast cancer cell line was used for cell toxicity test. T-test was performed for each group comparing to the control group. As shown in Figure 3.12, no significant cytotoxicity was observed in different time and concentration groups, which proved great biocompatibility for the HA polymer coated QDs, and show the potential for *in vivo* application in the future.

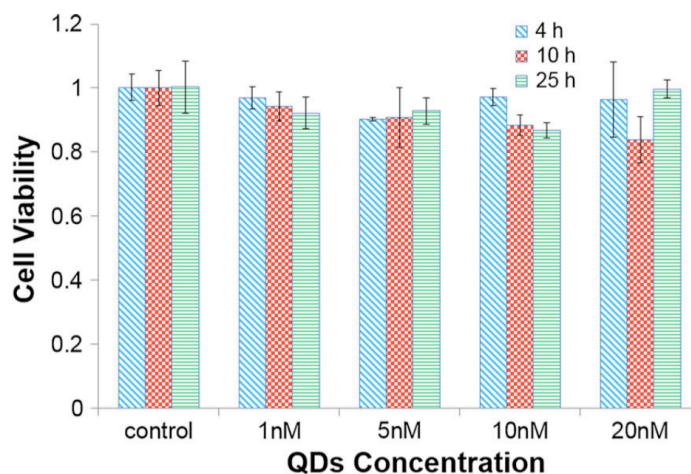


Figure 3.12. Cytotoxicity test of HA-cysteamine polymer-coated QDs. Dose-dependent viability evaluation of MD-MB-231 breast cancer cells treated for 4, 10, and 25 h. The experiments were performed in triplicate.

CD44⁺ Cancer cell targeted imaging

CD44⁺ MCF-7 and MD-MB-231 cell lines were used for targeted imaging and NIH/3T3 cell line was used as a negative control. QDs with different final concentrations of 5 nM and 10 nM have been tested, and shown in Figure 3.13. Obviously, strong fluorescence on MD-MB-231 and MCF-7 cell lines was observed but no fluorescence on NIH/3T3 cell line can be seen. This result not only demonstrates the targeted ability of the polymer coated QDs, but also indicates very little non-specific cellular binding for NIH/3T3 cell. Therefore, for future studies, final concentration of 5 nM QDs will be high enough for HA targeted imaging.

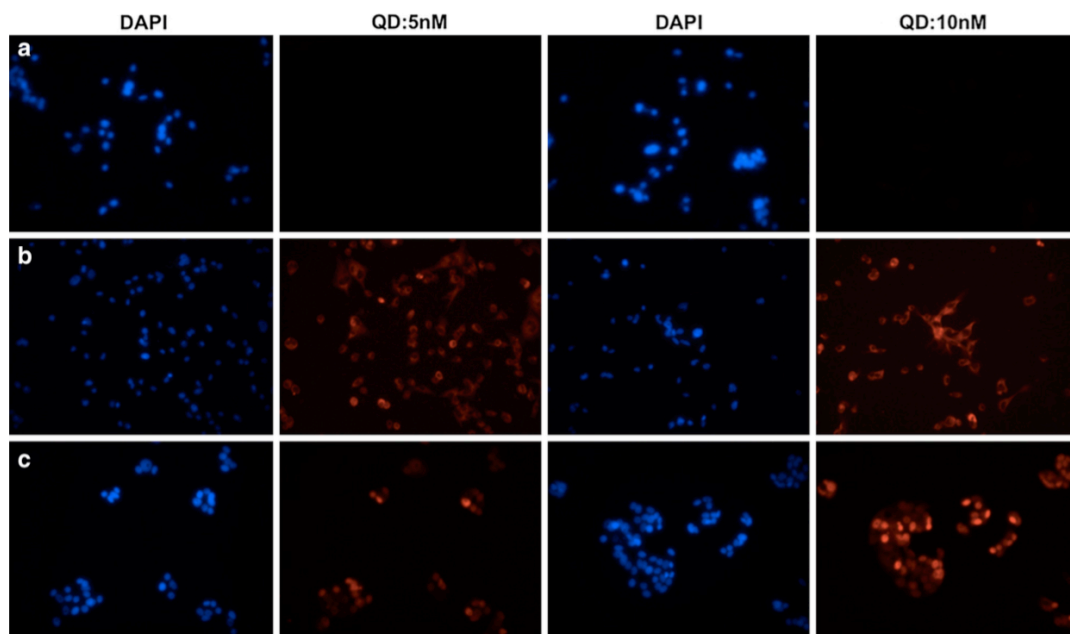


Figure 3.13. Illustration of the targeted imaging of breast cancer cells with HA-cysteamine polymer-coated QDs with final concentration of 5 and 10 nM. (a) NIH/3T3 fibroblast cell line shows no QD fluorescence and little non-specific cellular binding. (b) MD-MB-231 breast cancer cell line shows strong QD fluorescence of targeted staining. (c) MCF-7 breast cancer cell line also shows strong QD fluorescence of targeted staining. 20X objective was used on an Olympus IX 71 microscope

Hyaluronic acid receptor competitive imaging

In order to confirm that the staining of breast cancer cell line is receptor mediated, we conducted a HA competitive imaging experiment on MCF-7 cell by treating the cells with different concentrations of HA before adding of HA polymer coated QDs. As presented in Figure 3.14, when HA concentration increases, the QDs fluorescence intensity shows a downward trend and QD fluorescence couldn't be detected at 10 μ M HA treating dosage. This result is a solid evidence to prove that the mechanism of HA-QDs to stain the cells is mediated by the HA receptor.

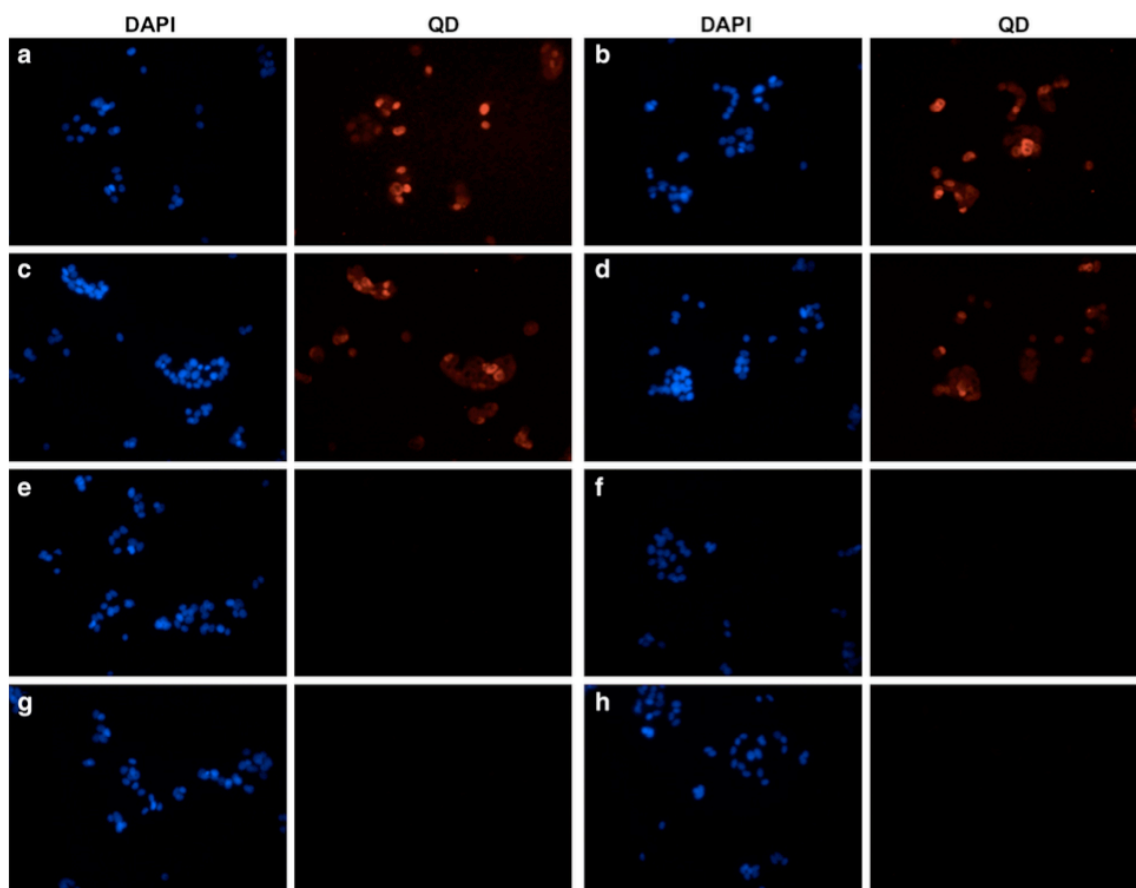


Figure 3.14. HA receptor competitive targeted imaging of MCF-7 cell line with HA-cysteamine polymer-coated QDs treated with different concentrations of HA. (a) Control group (no HA), (b) 10 nM, (c) 100 nM, (d) 1 μ M, (e) 10 μ M, (f) 100 μ M, (g) 1 mM, (h) 10 mM. QD final concentration was 10 nM for all. 20X objective was used on Olympus IX 71 microscope. From 1 to 10 μ M HA, QD fluorescence intensity has a dramatic change, which indicates that the staining is mediated by HA receptor

3.3.2 Discussions

The current established one-step QDs modification method is advantageous in the following three aspects. Firstly, for biomedical applications a targeting moiety like antibody, peptide or small molecule should be added to the surface modified QDs, so that QDs can be used to target tumor biomarkers as well as tumor vasculatures with high affinity and specificity [4]. Because most of the surface coating itself doesn't have targeting ability, thus a following bioconjugation step is necessary. However, it is always

time consuming and usually increases the overall size of QDs. Comparing with previous multidentate polymer coating methods [44-54], the current method is much simplified. By employing the HA polymer as the coating molecules, we have circumvented the targeting moiety conjugation step, and produced QDs with not only small size, but also CD44 receptor recognition groups, namely the carboxyl groups on HA.

Secondly, the traditional QDs coating methods, such as single thiol [27, 43] and di-thiol coating[204] could not protect the QDs surface very well thus the resulting stability is not good enough. And their applications for *in vivo* imaging are hampered by their sensitivity to biochemical environments. In order to get more stable QDs, recent efforts have been directed toward synthesizing ligands or polymers with multiple functional groups with different backbones and pendant groups. For instance poly (methacrylate), [46, 48, 52, 53] poly (acryl acid) (PAA) [44, 47, 49] and poly (maleic anhydride)[45, 54] are the most frequently used backbones. DHLA [46, 49-53] and cysteamine [44, 45, 47] are mostly used as anchoring group, and polyethylene glycol (PEG) [45, 48-50, 52-54] is often used as pendant group to increase water solubility and minimize non-specific cellular binding. However, the reported pH stability is still in a limited range and short time. For instance, polyPEG QDs were incubated at room temperature for 4 h in a pH range of 5-10.5 [48], or for days over a pH range 5.0-9.0 [205]. In this work, a wide pH range of 2-12 has been tested with as long as 24 h incubation time, showing great pH stability and potential to adapt to a more complex body environment. Besides, it is reported that SiO₂ and PE-PEG coated QDs has remarkable stability among pH 1-14 [38], however the pH stability was recorded for only 1 h and the size of the modified QDs are as large as 40-50 nm. These QDs are good candidates for pH sensing, but may not be very suitable for biological application since further bioconjugation will undoubtedly increase the overall size.

Thirdly, the introduction of reverse micelle can prevent QDs aggregation and help keeping good dispersity. This has been demonstrated by the TEM images and the DLS analysis. The reason is that the reverse micelles are tiny droplets of water encapsulated by the surfactant molecules IGEPAL CO-520 and thus physically separated from the cyclohexane oil phase. This water-in-oil microemulsion provides microreactors for QDs coating with hydrophilic cysteamine-HA molecules, therefore allows excellent control of the particle size, shapes, homogeneity and negligible contamination of the product compared with other bulk wet approaches like traditional biphasic exchange method with thiol containing molecule and polymers [43, 44].

It is notably that HA targets the cell receptor through the carboxyl groups, therefore the modification ratio of carboxyl groups on HA is very important. People have done a series of work using adipic acid dihydrazide modified HA to conjugate commercial carboxyl Quantum Dots for *in vivo* imaging, and found that lower carboxyl modified HA (i.e. 35%, 22%) kept the targeted ability for HA receptors in liver, while higher modification ratio (i.e. 50%, 68%) HA will lose much of HA targeting ability [196, 197]. In our work, about 42% of the carboxyl group on HA was modified and the CD44⁺ cancer cell targeted imaging test has proved that this ratio still works well for HA to keep the targeting ability for receptors.

3.4 Summary

In conclusion, we have successfully developed a novel HA-cysteamine polymer coated QDs which are water-soluble, and stable for long time and over a large pH range. The polymer coated QDs shows great biocompatibility and no significant toxicity. Moreover, the HA-cysteamine polymer coated QDs holds CD44⁺ cancer cell targeting ability for breast cancer cell lines. In our work, we only test breast cancer cell lines, but we can see the potential of HA-QDs for other CD44⁺ cancer cell lines. Besides, the

carboxyl groups on the polymer also allows for further functionalization and conjugation. These HA polymer coated QDs open new possibilities such as for long time single QDs tracking, and moreover for *in vivo* cancer imaging.

CHAPTER 4

MULTI-MODALITY HA COATED-QDS FOR OPTICAL/MRI/PET IMAGING

Abstract

Based on the previous work of HA-cystamine polymer coated QDs, the HA polymer was further conjugated with DTPA and DOTA for multi-modality MRI/optical and PET/optical imaging. The DTPA can conjugate Gd ion thus provides ability for MRI imaging and the DOTA unit renders the QDs to have the ability for conjugating Cu ion which provides future ability for ^{64}Cu isotope coupling for PET imaging. The resulting QDs have great water solubility, and excellent colloidal stability. The biocompatibility to NIH/3T3 fibroblast cells and Hela cervical cancer cells were tested. Moreover, CD44⁺ cancer cell targeting ability for cervical cancer cell lines were also tested. This novel HA-DTPA and HA-DOTA polymer holds the promise for multi-modality imaging, such as MRI/optical, PET/optical, SPECT/optical and MRI/PET/SPECT/optical imaging and will have an important influence on cancer diagnostics, molecular imaging, and the integration of different modality imaging.

4.1 Background of Multi-modality imaging probes

4.1.1 Background

Different imaging techniques have their own unique advantages and inherent limitations, therefore, it is unlikely that a single probe can be used for all applications. Typically, high-resolution imaging modality has relatively poor sensitivity, while high sensitivity imaging technique usually has poor resolution. For example, fluorescence imaging can provide high sensitivity, and the ability to have sensitivity for single cells

and subcellular imaging, and can achieve multiplex imaging, but lower tissue penetration depth. MRI and PET can provide high penetration depth, and they are non-invasive imaging techniques. However, PET has a relatively low spatial resolution and the sensitivity of MRI is relatively low [122, 189].

Modality	Form of Energy Used	Spatial Resolution/mm	Imaging Time	Required Molecular Probe Mass (ng)	Advantages	Imaging Cost	Clinical Translation
PET	Annihilation photos	1-2 (microPET); 6-10 (clinical PET)	Minutes	1-100	High sensitivity; quantitative; tracer amount of probe	High	Yes
SPECT	Gamma rays	0.5-2 (microSPECT); 7-15 (clinical SPECT)	Minutes	1-100	High sensitivity; quantitative; tracer amount of probe	Medium-High	Yes
MRI	Radio frequency waves	0.01-0.1 (small-animal MRI); 0.5-1.5 (clinical MRI)	Minutes to hours	10^3 - 10^6	High spatial resolution; superb soft tissue discrimination	High	Yes
FI	Visible to infrared light	<1 (FRI); 1 (FMT)	Seconds to minutes (FRI); minutes (FMT)	10^3 - 10^6	High sensitivity; multiplexed imaging	Low (FRI); Medium-High (FMT)	Yes
BLI	Visible to infrared light	3-5	Minutes	10^3 - 10^6	High sensitivity; high-throughput	Low	No
US	High frequency sound waves	0.04-0.1 (small-animal US); 0.1-1 (clinical US)	Seconds to Minutes	10^3 - 10^6	High sensitivity; portable	Low-Medium	Yes

Figure 4.1. Comparisons of advantages and limitations for each imaging modality (from Yan Xing et al. [12])

In recent years, a variety of imaging modality fusion concepts are very popular and multi-modal imaging techniques and equipment has been greatly developed. Researchers have learned that different imaging modalities can complement to each other and will have a big impact on the bio-medical imaging area. The first fusion of two modal PET / CT device was developed in 1998 by Townsend and his colleagues in cooperation with Siemens Medical and machine was commercially available in 2001 [14]. The next dual-modality PET / MRI instrument was also expected to improve patient safety and in the imaging capability than PET / CT. Nowadays, PET, CT, SPECT, Fluorescence imaging modalities have been fused and developed to 4-modality imaging machine [13]. With the emergence and gradual integration enhanced imaging technology,

these new tools led to the imaging probe design and development, in order to help multi-modality imaging equipment to better realizes the advantages of multi-modality imaging.

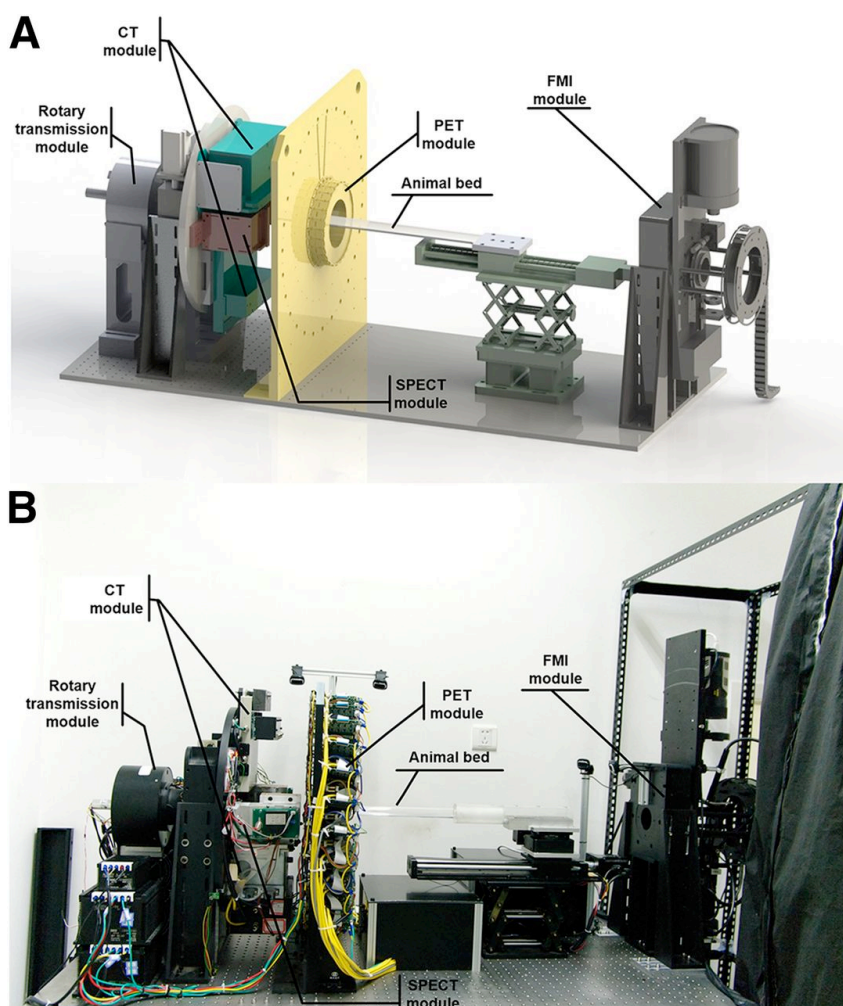


Figure 4.2. Multi-modality imaging machines (A) Quad-modality imaging system design, which consisted of PET, CT, SPECT, and FMI modules. (B) Photograph of quad-modality imaging prototype system. (from Lu et al [13])

In the past few years, the research on multi-modal molecular imaging probe has made a lot of progress [14]. The imaging method of multi-modal probes will help to achieve high resolution, high sensitivity biomedical imaging. To have a more comprehensive view of the disease, an ideal situation is to use multi-modality contrast agent on multi-modality imaging techniques. An advantage of the multi-modality contrast

agent is to avoid multiple injections of contrast agent in the body. What's more, multi-modality probes allow the overall optimization of space, time and sensitivity and can obtain a variety of information in organ, tissue, cellular and sub-cellular level. For example, the research on bimodal contrast agents, optical / MRI contrast agents have been studied a lot in recent years. The optical contrast agent allows the detection of fluorescence intensity of the cells or sub-cellular level while MRI contrast agents typically have a deep tissue penetration property, can reflect physiological differences in tissue and organ levels [14]. Thus, these two complementary techniques help to obtain information that will allow a more precise diagnosis.

Although not all imaging applications require multiple imaging modality binds to a single probe, a multi-modality imaging probe has many advantages. A multi-modal probe can guarantee the same pharmacokinetics and co-localization of different imaging modes. Also it avoid using multiple doses of imaging probes to bring a lot of pressure to the in vivo blood clearance [14]. One thing should be note is that, due to the different sensitivity between different imaging modalities, we cannot simply add all different modalities to one molecule, because the required concentration of the contrast agents are different among different imaging modes [14].

Functionalized nanoparticles for enhancing medical diagnostic image contrast has been playing an increasingly important role in molecular imaging and is very important. Currently the most active areas of research on multi-modality probes are in nano-materials, which has proved good integration of other imaging modalities to form a multi-modal imaging probes [7]. The size and nature of the multi-component nanomaterials provides an excellent platform that can combine with various imaging modalities. Compared with a typical traditional multi-modality small molecular probes, the synthesis procedure of some of the of nanoparticles are relatively simple and fast, and does not require complex multi-step organic synthesis and allow a modular approach, so that the

element replacement for the nanoparticles can be done only by changing simple reagents and does not require the entire redesign [14].

Multi-modality imaging contrast agents can provide a plurality of signals from a biological sample, thus greatly improving the visualization of biological processes. The combination of optical imaging techniques and MRI may represent a useful imaging modality pair for more accurate biomedical detections [22-24], Where MRI or optical imaging can be used to track the distribution of the probes in the body. The advantage of MRI is its high anatomy spatial resolution, but its sensitivity is not good enough, especially for the tiny tumors. While fluorescence imaging has high sensitivity, and the instruments nowadays can detect very little photons and present images on the computer screen. Shorter wavelength light cannot penetrate to deeper tissue, which limits its biological applications. However, the near infrared light can penetrate to relatively deep tissue. Therefore, by combining MRI and fluorescence imaging together, a multimodal imaging probe will have the advantages of high sensitivity and high spatial resolution, so as to enhance the ability of recognition and diagnosis of tumors.

4.1.2 Multi-modality QDs probes

The advantages of quantum dot have made them a good substitute for fluorescence imaging because it can diagnose diseases and other applications at the cellular level to achieve high sensitivity, high spatial resolution, and target-specific real-time imaging. However, fluorescence imaging technology also has its own drawbacks, such as low tissue penetration depth and biological auto-fluorescence, which limits its application in imaging deep tissue. Therefore, they are widely studied in developing multi-modal probes, such as combining PET or MRI [21]. A main approach for synthesizing multi-modality quantum dots can be classified as a conjugation method, such as gadolinium and other molecules attached to the QDs surface via chemical connection. A typical approach is to attach agents such as DOTA and DTPA to the

surface of the quantum dot to chelate PET- or MRI active molecules [55-57, 143, 172-176]. The second method is a core / shell structure, other molecules are comprised in an additional layer to coat QDs [58, 59]. The third way is by doping the appropriate molecules or atoms such as Mn into the QD core [22, 60].

QDs conjugates

The most direct method of modifying quantum dots is by using bifunctional chemical crosslinkers to attach two different molecules to each other, typically functional groups such as amine, thiol or carboxyl group, followed by reaction of the crosslinking agent for a given functional group for specifically connection [206]. A typical approach is to attach agents such as DOTA and DTPA to the surface of the quantum dot to chelate PET- or MRI active molecules [189]. The traditional method through coupling chemistry using succinimidyl ester derivative has been widely used for connecting gadolinium (III) or ^{64}Cu to the amino group on quantum dot surface. In this way, DOTA and DTPA have been coupled to the CdTe / ZnS quantum dots [207] CdSe/ZnS, and glutathione-coupled CdSeTe/CdS QDs.

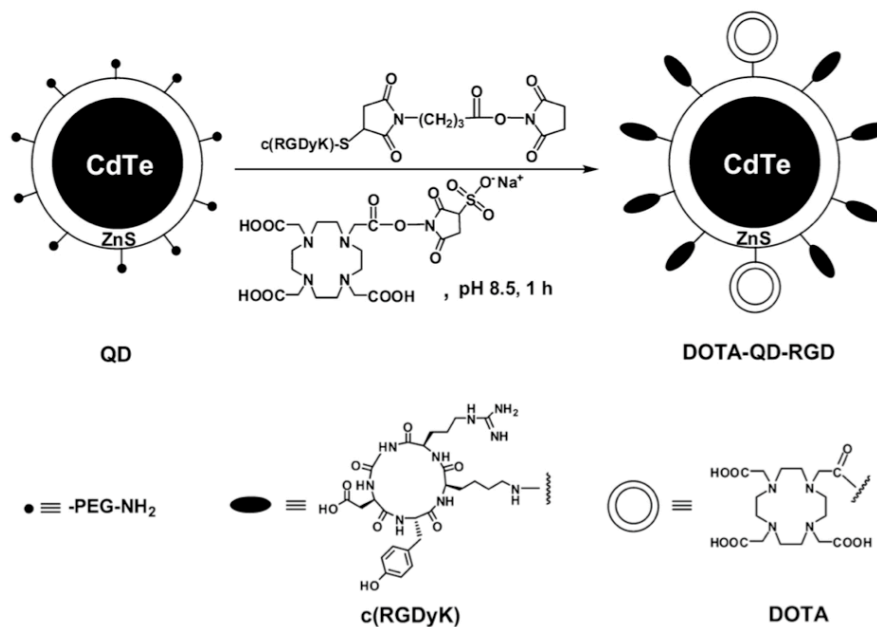


Figure 4.3. Synthesis of dual-function PET/NIRF probe DOTA–QD–RGD through Chelator coupling to surface of CdTe nanoparticles. (From Louie [14]).

A uridine-based dual-modality probe based on quantum dots (QDs) has been reported [208]. The Gd^{3+} -QDs was synthesized through complex procedures. The Gd^{3+} -QD can penetrate the cell surface and can be delivered into the RAW 264.7 cells. The Gd^{3+} -QD enables high-performance MR and fluorescence imaging. This work provides possibilities for QDs based optical/MR imaging, but the synthesis is complex and the coating material cannot provide targeted ability.

In order to limit the intrinsic toxicity of QDs constructed from heavy metals, Stasiuk et al. used InP/ZnS quantum dots with an emission wavelength at around 620 nm which were direct conjugated with gadolinium chelates containing single thiol or dithiol [209]. Another work by Erogbogbo et al. used silicon QDs which is composed of a PEGylated micelle, with hydrophobic Silicon QDs in the core, covalently bound to DOTA-chelated Gd^{3+} , with dynamic light scattering radius of 85 nm [210]. In this work, after the macrophages cell uptake, the probes maintain their optical properties within the intracellular environment. However, only *in vitro* work was done and tumor-targeted study has not been done.

Lipid-Coated dual-modality QDs

Another method for making dual-modality QDs is to introduce paramagnetic ions to the coating lipid shell of the QDs where Gd chelates with lipids are inserted into the lipid coating layer to render MRI functionality [15]. Mulder group have done a lot of work using this typical configuration for different biomedical applications [211-215]. The process was done through evaporation of the mixture of QDs and paramagnetic lipids, as shown in Figure 4.4 [216]. The properties of the particles are similar to liposomes and can be synthesized in a similar size ranges with the QDs which are usually smaller than 10 nm [214]. The size and use of stealth coatings such as PEG can both facilitate to increase the circulating half-life of the probes.

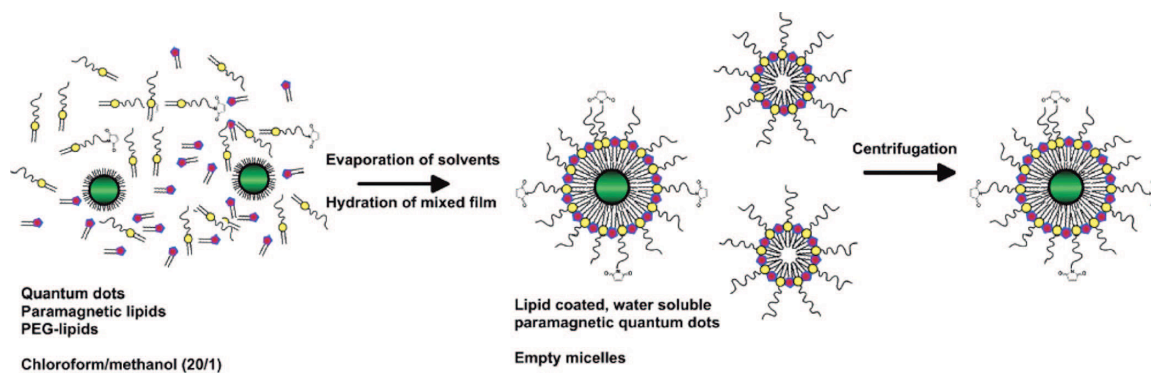


Figure 4.4. Synthesis of lipid-coated multi modality QDs (form Louie [15])

Doped QDs

The third method is by doping the appropriate molecules to QDs. Because the QDs are really small, doping into QDs are very challenging, but still has been studied a lot. The QDs has been doped with transition metals, and the properties are characterized [217-222]. For example, Mn has been doped into II-VI quantum dots such as ZnSe [223], ZnS [224], CdSe [225], and into III-V systems such as InP [226]. The doped QDs materials has been investigated for multimodal imaging applications.

There are some challenges for directly doping into the QDs, because many introduced dopants or impurities will quench the luminescence efficiency of the QDs. The quenching is in a concentration dependent way, therefore the improvement of the MR contrast properties will degrade the optical imaging ability [227]. In order to avoid this problem, researchers have studied many ways to incorporate the paramagnetic ions into the outer coating shell rather than the core to keep the luminescent efficiency. Most quantum dots for biological applications are core/shell structure where the core is coated with a shell of different materials [228]. The shell helps to protect the core from degradation and also improve the surface passivation thus increase the luminescence efficiency. For example, Cd-based QDs (CdSe, CdS, etc.) are usually coated with ZnS shell to prevent the release of toxic Cd ions if the core is degraded. The concept of shell

coatings provide a good platform of multi-modality probes, for each layer can have another functionality, and a lot of work were designed and reported.

The fabrication of Gd-doped CdTe quantum dots (Gd:CdTe QDs) as an agent for dual-modality MRI/ optical imaging was shown in Figure 4.5. A facile one-pot aqueous approach was used and the QDs are synthesized at room temperature with an ultrasmall particle size. Further conjugation with the folic acid renders the QDs targeting ability and successfully labelled live HepG2 cells for targeted cellular imaging [16].

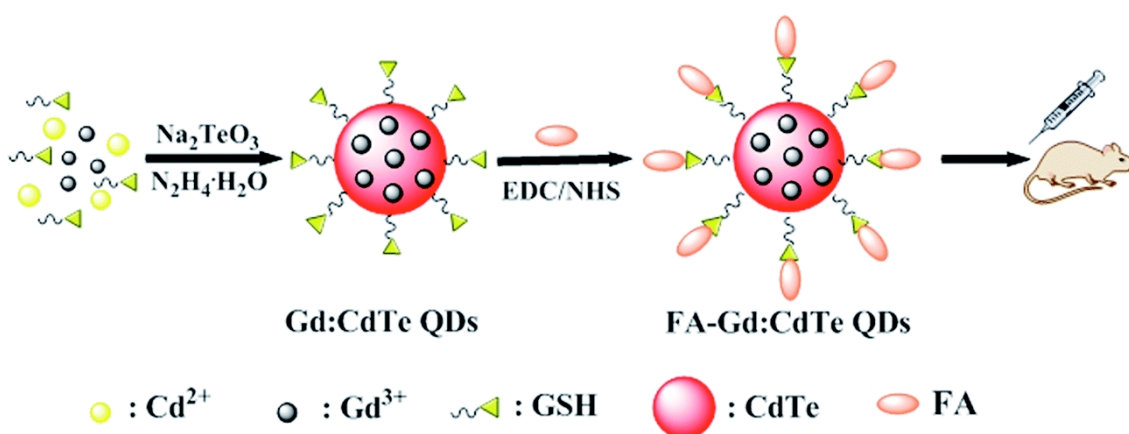


Figure 4.5. Schematic shown for the synthesis of the Gd:CdTe QDs and their surface function with Folic acid. (from Zhang et.al [16])

In another work by Dr. Mingyuan Gao's group, Cd-free $\text{CuInS}_2@\text{ZnS}:\text{Mn}$ QDs were synthesized for dual-modality fluorescence and MRI imaging of tumors *in vivo* [22]. Those QDs has a Zn gradient CuInS_2 core and a ZnS shell and the Mn ions were incorporated into the ZnS shell in order to balance the optical and magnetic properties of the QDs. The QDs were further PEGylated through ligand exchange by using DHLA-PEG ligand. The resulting QDs showed 7000 times lower cytotoxicity than the CdTe QDs and experiments on fluorescence and MR imaging of tumors showed that both the subcutaneous and the intraperitoneal tumor can be visualized for *in vivo* imaging.

Dual-Targeting and Dual-Modality *in vivo* cancer imaging with Quantum Dots

Except for dual-modality imaging probes, dual-targeting probes was another trend that was studied. Recently a dual receptor targeting dual-modality PET/near-infrared fluorescence (NIRF) probe was developed for a more accurate evaluation of tumor-targeted efficacy of QDs [17]. In this work, the QDs were modified with beta-Glu-RGD-BBN (BBN is bombesin) peptides and labeled with F-18 via the 4-nitrophenyl-2-F-18-fluoropropionate prosthetic group. As shown in Figure 4.6, the structure of the multiplex modifying multi-functional QD probe was on the left and structure of single modified multi-functional QDs probe was in the middle, and strategy for enhancing synergistic binding of the hetero-dimeric multi-functional QDs probe was on the right. The functionalized QD probe showed a great promise as a universal dual-targeting probe for *in vivo* detection of tumors and opens up a new strategy for multi-targeting multi-modality QD probes for improved tumor-targeting efficacy.

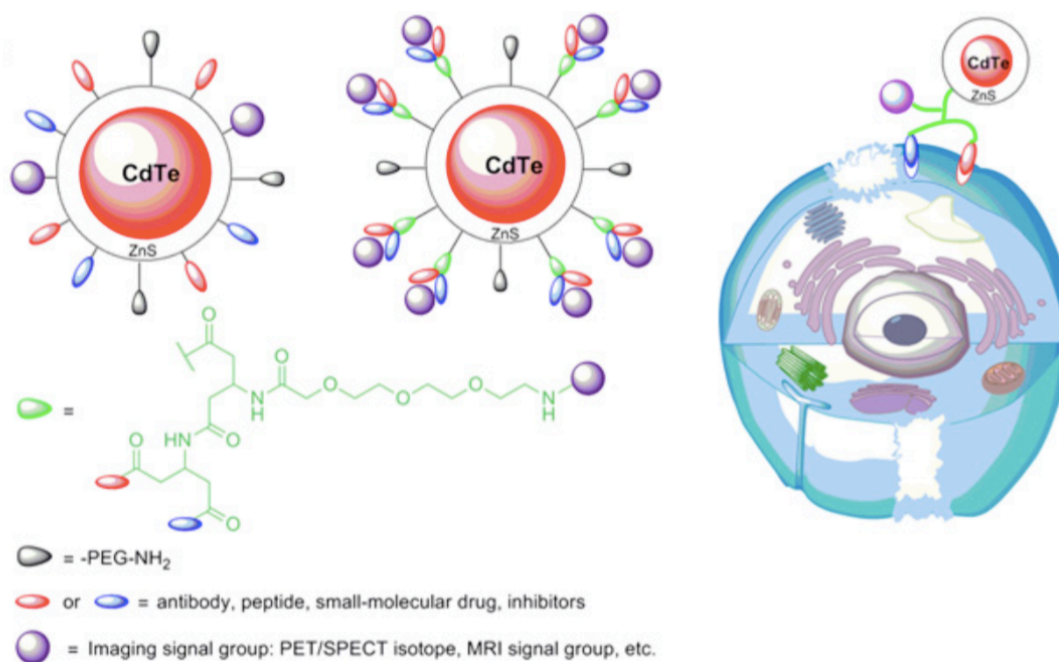


Figure 4.6. Schematic illustration of functionalized QD probe for *in vivo* cancer dual-targeting and dual-modality imaging (from Kongzhen Hu et al. [17])

Summary

Combining modalities of different instruments and in different probes have the advantages and benefits, but there is no one is the best approach for all problems. The clinical applications for multi-modality probes still need time to establish for not all applications benefits from an all-in-one probe. Therefore, to identify the diagnostic and therapeutic targets which have the most to gain from common probe is still a challenge which will aid in increase of the acceptance of multi-modality imaging probes. What's more, the collaboration between biologists, chemists, and clinicians is very important in order to adapt biologically incompatible probes with imaging properties for the realistic uses. Greater cross communication and multi-modality cross communication will be crucial for the development of new probes especially for novel nanotechnology platforms. Another thing that need to notice is that some modalities such as PET and MRI have different sensitivities, therefore multi-modality probes will require a lot of low-sensitivity probes which increase probe size comparing to the high sensitivity probe, in order to fulfill the concentration requirements for each modality. In an ideal situation, fusing probes of different functions should not reduce each probe's individual effectiveness [15].

4.2 HA-DTPA-Gd QDs for dual-modality optical/MRI imaging

4.2.1 Materials and Methods

Materials

Sodium hyaluronate with MW of 6300 was purchased from Lifecore (USA). Cystamine dihydrochloride, dithiothreitol (DTT), IGEPAL CO-520, tetramethylammonium hydroxide (TMAH), diethylene triamine pentaacetic acid (DTPA) were purchased from Sigma-Aldrich. NIR QDs were purchased from Invitrogen. EDC and sulfo-NHS were purchased from Pierce. $GdCl_3$ were purchased from Aladin. Tetra-azacyclododecanetetra-acetic acid (DOTA) were purchased from STREM chemicals. Dry

DMSO was provided by J&K Scientific. Cyclohexane, Methanol, Ethanol and other solvent were purchased from Sinopharm Chemical Reagent Beijing. Dialysis tube (MWCO 1000) was purchased from Spectrum Labs. UV–Vis absorption spectra were obtained using a UV-2550 UV-vis spectrophotometer (Shimadzu). The fluorescence spectrum was recorded on a Nanolog FL3-2iHR (HORIBA JOBIN). The structural details of the nanoparticles were analyzed by the HRTEM method using a JEM-2100F at Peking University. NMR spectrums were performed on a 400Hz NMR machine at the NMR imaging center of Peking University. Gadolinium and copper contents were determined on an inductive coupled plasma-optical emission spectrometry (PROFILE SPEC, Leeman Labs, USA). MRI images are acquired on a GE Discovery MR 750 3.0T machine with a T/R Animal coil by Magtron-35mm using SE series.

Methods

Synthesis of HA-cystamine-DTPA-Gd polymer

As shown in Figure 4.7, the synthesis of HA-cysteamine-DTPA-Gd polymer involves four steps: synthesis of HA-cystamine polymer, DTPA conjugation to the HA-cystamine polymer, Gd coupling and reduction of the disulfide bond of cystamine by DTT.

Typically, sodium hyaluronate with average MW of 6276 was dissolved in PBS to about 10 mg/ml, then 17 molar excess of EDC, and final concentration of 5mM sulfo-NHS were added to the HA sodium salt solution. The solution was stirred for 15min to activate the carboxyl groups on HA polymer. Then 30 molar excess of cystamine dihydrochloride in PBS were added, and the mixture was kept reacting at room temperature for 24 h. The HA-cystamine product was purified by dialysis against pure water using dialysis tube (molecular weight cut-off, 1kDa) for 2 days and lyophilized to get the dry HA-cystamine product. The HA-cystamine conjugation was confirmed by ¹H NMR on a 400MHz machine.

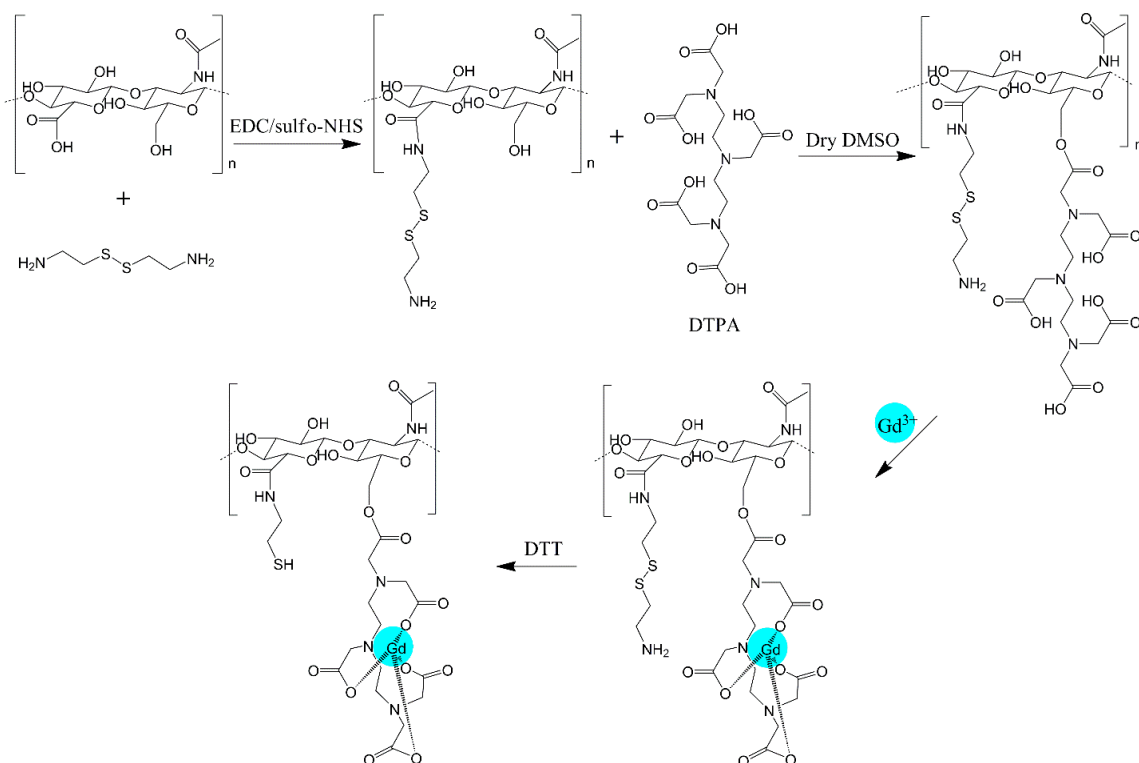


Figure 4.7. Synthesis routes of HA-DTPA-Gd polymer

Table 4.1. Typical amount for HA-cystamine synthesis.

Reagent	Equivalent	Amount (umol)	Molecular weight(g/mol)	weight (mg)	volume (ml)	
Hyaluronic acid sodium salt	1	39.8	6276	250	23	in PBS
COOH	17	677.2				
EDC	30	1195.1	191.7	229.1	1	
sulfo-NHS		125	217.13	27.1	1	
Cystamine dihydrochloride	30	1195.0	225.2	269.1	0	
					25	in PBS

According to previously reported method [229, 230], DTPA was conjugated to the HA backbone by the formation of ester bonds between the carboxyl group in DTPA and the hydroxyl group in the HA backbone. Typically, 40 molar excess of DTPA and HA-cystamine were dissolved in 50 ml of anhydrous dimethyl sulfoxide and protected

with a drying tube containing calcium chloride inside. The mixture was stirred for 24 h at room temperature, and after the reaction, 25 ml of pure water was slowly added to the solution. The resulting solution was placed in a dialysis bag (molecular weight cut-off, 1kDa) and dialyzed against pure water for 2 days. The dialysis product was lyophilized and the HA-cysteamine-DTPA product was obtained as a powder.

The conjugation of DTPA to HA was confirmed via fourier transform infrared spectrometry (FT-IR) on a VECTOR22 (Bruker, Germany). Spectra was recorded on KBr plates over the range 4000~400 cm^{-1} at a wavenumber resolution of 1 cm^{-1} . To determine the amount of DTPA that was conjugated to HA, NMR was also conducted on a 400MHz NMR machine.

Table 4.2. Typical amount for HA-cystamine conjugating DTPA.

Reagent	Equivalent	Amount (umol)	Molecular weight(g/mol)	weight (mg)	volume (ml)	
HA-cystamine	1	9.2	6276	57.8	50	in DMSO
DTPA	40	368.4	393.35	144.9		

Subsequently, for Gd coupling, 50 molar excess of $\text{GdCl}_3 \cdot 6\text{H}_2\text{O}$ and HA-cysteamine-DTPA polymer were dissolved in 8 ml of water and shaken for 24 h at room temperature and then dialyzed in a dialysis bag (molecular weight cutoff, 1 kDa) against pure water for 1 day.

Table 4.3. Typical amount for Gd coupling with HA-cystamine-DTPA polymer.

Reagent	Equivalent	Amount (umol)	Molecular weight (g/mol)	weight (mg)	Volume (ml)	
HA-cystamine-DTPA	1	9.2	6276	57.8	8	in water
GdCl_3	50	460.5	371.7	171.2		

Finally, for DTT reduction of the disulfide bond on cystamine, DTT of a final concentration of 80mM was added and the whole solution was shaken for 24 h. After dialyzing, 5~10 mg DTT was added to the solution to protect the free thiol groups. After lyophilizing, the HA-Gd polymer was collected.

Gadolinium contents were estimated on an inductive coupled plasma-optical emission spectrometry (ICP-AES). For the ICP-AES sample preparation, the HA-Gd polymer was digested by adding 3.5mg polymer to 5ml HNO₃, and incubate overnight. On the 2nd day, 2ml perchloric acid was added and the mixture was heated slowly to 170°C for 1.5h. Finally pure water was added to 10 ml. Gadolinium contents were determined on an inductive coupled plasma-optical emission spectrometry (PROFILE SPEC, Leeman Labs, USA).

QDs coating with of HA-DTPA-Gd polymer and characterization

NIR Organic (CdSeTe) ZnS QDs of 780 nm emission wavelength were purchased from invitrogen. When encapsulating QDs with HA-DTPA-Gd polymer, a modified reverse micelle method was used [94, 124, 202]. Typically, 200µl of 1µM QDs in decane were diluted with 4.5 ml cyclohexane and 0.5 ml IGEPAL CO-520 was added to the solution. Then 3.5~4 mg of HA-DTPA-Gd polymer in 50 µl water was added to form reverse micelle. 50 µl of 0.1M Tetramethylammonium Hydroxide (TMAH) in methanol was also added as a catalyst. The mixture was vortexed for 1 min, and shaken for 60 min. After reaction, 1 ml ethanol was added and the solution was centrifuged at 6000g for 5 min to precipitate the HA polymer-coated QDs. The pellets were washed with additional ethanol for 3 times and washed with water once and finally re-dispersed in water. After centrifuging the QDs solution at 5000 g for 5 min to get rid of the undissolved parts, the supernatant which contains the HA polymer-coated QDs was purified using a 0.45 µm syringe filter.

For characterization, the UV-vis absorption spectrum was recorded on a UV-2550 UV-vis spectrophotometer (Shimadzu). The fluorescence spectrum was recorded on a

Nanolog FL3-2iHR (HORIBA JOBIN). The structural details of the nanoparticles were analyzed by the HRTEM using a JEM-2100F under the help of Dr. Jia at College of Chemistry and Molecular Engineering, Peking University. This machine was equipped with a field emission gun, ultra-high resolution pole piece, and ultrathin window JEOL detector. An OSIS CANTEGA CCD camera was used to obtain the HRTEM images. The gadolinium contents were determined on an inductive coupled plasma-optical emission spectrometry (PROFILE SPEC, Leeman Labs, USA) by digesting QDs with HNO₃ and perchloric acid.

Relaxation rate measurements of the HA-Gd QDs

The T1 relaxivity of HA-GD QDs was compared with Gd-DTPA solution of the same Gd concentration. The test was performed with GE Discovery MR 750 3.0T machine. The T1 contrast intensities of the HA-Gd QDs and Gd-DTPA solution were scanned at 0.2, 0.1, 0.05, 0.02, 0.01 and 0.005 mM of Gd concentrations. Typically, 500 μ l of HA-Gd QDs and Gd-DTPA solution at different concentrations were put in each 1.5ml Eppendorf tube, and placed in a plastic box containing pure water. A head and neck unite coil of the MRI machine was used to hold the box and T1-weighted MR images was collected at different repetition time. The specific parameters are as follows: echo time (TE) = 9 ms, repetition time (TR) = 100, 200, 300, 600, 900, 1200, 1500 ms.

Cell viability test

Hela cervical cancer cell line was cultured in DMEM with 10 % FBS and 1 % streptomycin and penicillin antibiotics. On the first day, cells were seeded on a 96-well plate at 5000 cells/well. After 24 h culture, HA-Gd polymer-coated QDs were added to the 1, 4 and 8 h incubation time group with the final concentrations of 1, 5 and 10 nM. For the control group, cells of the same number were seeded but no QDs were added. This is regarded as 100 % cell viability. A blank control with only cell culture medium in the well was regarded as 0 % cell viability. Experiments were quintuplicated. After incubation with QDs, 10 μ l Cell Counting Kit-8 solution was added to each well.

Following incubation with cells at 37 °C for 3 h, the absorbance at 450 nm was measured by a plate reader.

In vitro cell targeted imaging

CD44⁺ cervical cancer Hela cells were used for targeted imaging and NIH/3T3 fibroblast cell was used as a negative control. The cells were cultured in DMEM with 10% FBS and 1 % streptomycin and penicillin antibiotics. Cells were plated on an 8-well chamber slide at 10k cell/well in 400ul culture medium. After 24 h growth, the medium was aspirated and cells were washed with 1X PBS buffer and then fixed with 200 µl 4 % formaldehyde and 0.25 % Triton X-100 in PBS for each well. After 15 min, cells were washed with PBS for 5 min, three times. After fixation, 160 µl blocking buffer of 5 % bovine serum albumin (BSA) in PBS was added to each well and incubated for 1h at RT. Then blocking buffer was aspirated and each well was washed with PBS three times for 5 min each. For QDs coating, 100 µl HA polymer-coated QDs were added to each well, with final concentrations of 5nM and 20 nM in PBS. After 1 h incubation, the QDs was aspirated and washed with PBS for 3 times, 5 min each. The slides were mounted with anti-fade mounting media containing DAPI. The slides were imaged under Leica DMI3000B microscope.

In vivo Tumor-targeted fluorescence imaging

For the *in vivo* fluorescence imaging experiment, cervical cancer Hela cells was used to build the tumor model. Female “Balb/c nude” mice of six weeks are used as the experimental models. Tumors were created by subcutaneous injection of 5×10^6 Hela cells in 100 µL PBS buffer onto the back of right shoulder of each mouse. Tumors grew to a suitable size at the injection sites 6 weeks later. Before imaging, each mouse was subject to isoflurane anesthesia and placed in the animal bed in the right position with the anesthesia. HA-Gd QDs with an emission wavelength of 780 nm conjugates were prepared and purified with 0.2µm syringe filter before injection. 200µl of 50nM HA-Gd QDs were administered to the nude tumor bearing mice by tail-vein injection.

The fluorescence of injected HA-Gd QDs was captured with a luminescent image analyzer before and after injection. An animal fluorescence imaging system was used to take the fluorescence images, which contains a tungsten halogen-based excitation module, an adjustable animal holder, a high sensitivity CCD camera (iKon 934 M, Andor) detection module and a gas anesthesia component. High-resolution images (512×512 pixels) were taken using GFP filter (FF01-466/40-25) for excitation and Cy7 filter (FF02-809/81-25) for emission. The raw data was acquired under the control of baseline clamp and processed by Andor SOLIS software. The images were processed by ImageJ.

In vivo Tumor-targeted MRI imaging

For *in vivo* MRI imaging, the animal model was the same as for the fluorescence imaging. Female “Balb/c nude” Hela tumor bearing mice was used. The tumor-bearing mice are obtained by injecting Hela cells into their right back without any other treatment. After the tumors formed at the injection sites, mice were taken for MRI imaging. Before imaging, the mouse was injected with 10% chloralhydrate anesthesia for 100 µl / 25g mouse and placed in the animal bed in the ventral position. Then, HA-Gd QDs conjugates were prepared and purified with 0.2 µm syringe filter before injection. 200µl of 50nM QDs were administered to the nude tumor bearing mice by tail-vein injection. MRI images are acquired before and after the injection of the HA-Gd QDs contrast agents, on a GE Discovery MR 750 3.0T machine with a T/R Animal coil by Magtron-35mm using SE series. The TR was set to be 400 and TE was 12.

4.2.2 Results and Discussions

Characterization of HA-cystamine-DTPA polymer

The synthesis of HA-cysteamine-DTPA-Gd polymer involves four steps: synthesis of HA-cystamine polymer, DTPA conjugation to the HA-cystamine polymer, Gd coupling and reduction of the disulfide bond of cystamine by DTT.

For the HA-cystamine polymer conjugate DTPA, from the FT-IR image of HA-cystamine-DTPA (Figure 4.8), the peak at 1730cm^{-1} which represents the C=O formation is a strong sign that DTPA was successfully conjugated to the HA backbone.

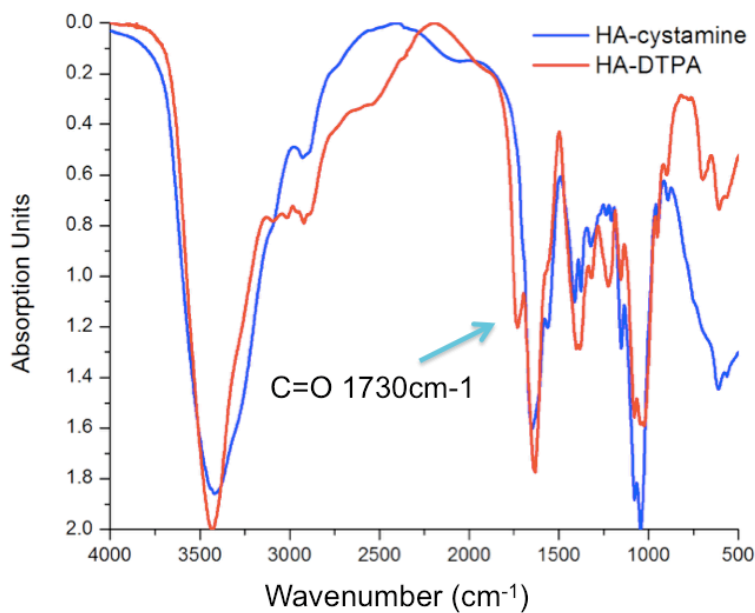


Figure 4.8. FT-IR image of HA and HA-cystamine-DTPA

The HA-cystamine conjugation was confirmed by NMR. As shown in Figure 4.9, the comparison of HA and HA-cystamine, the peak at around 2.85 ppm and 2.95 ppm which is the cystamine was shown, which proved successful conjugation of cystamine to HA polymer. The amount of cystamine and DTPA that was conjugated to HA can be calculated from the integration of the corresponding part on the NMR curve. After calculation, there were ~6 cystamine on each HA polymer.

Quantitative characterization of DTPA that was conjugated to HA-cystamine polymer was also confirmed by NMR. The NMR curve was shown in Figure 4.9, and the NMR prediction by chemdraw was shown in Figure 4.10. The circles of the same color represent the corresponded group. The amount of DTPA that was conjugated to HA can

be calculated from the integration of the corresponding part on the NMR curve. After calculation, there were 1 DTPA on every 2 HA polymer.

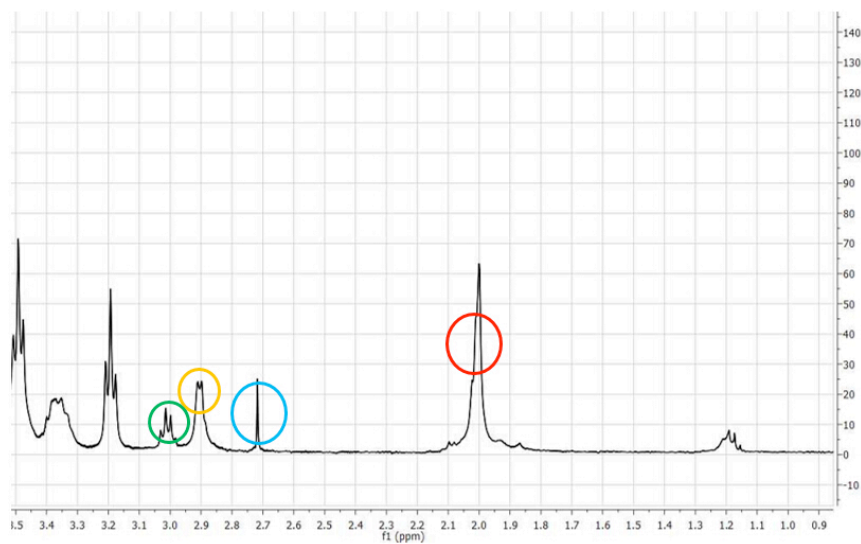
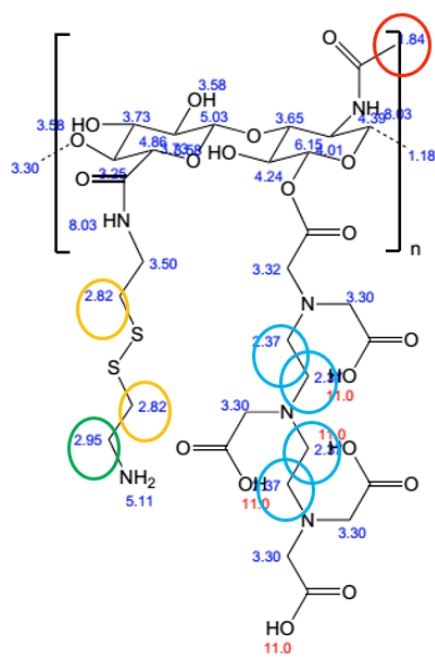


Figure 4.9 NMR image of HA-cystamine-DTPA

ChemNMR ^1H Estimation



Estimation quality is indicated by color: good, medium, rough

Figure 4.10. NMR prediction by Chemdraw of HA-cystamine-DTPA

Characterization of HA-Gd polymer coated QDs

UV-absorption and Fluorescence curve before and after HA-Gd polymer coating were shown in Figure 4.11. The QDs absorption and emission curve after HA-Gd polymer coating keeps the same shape as before coating, thus indicates a good stability of the HA-Gd polymer coated QDs.

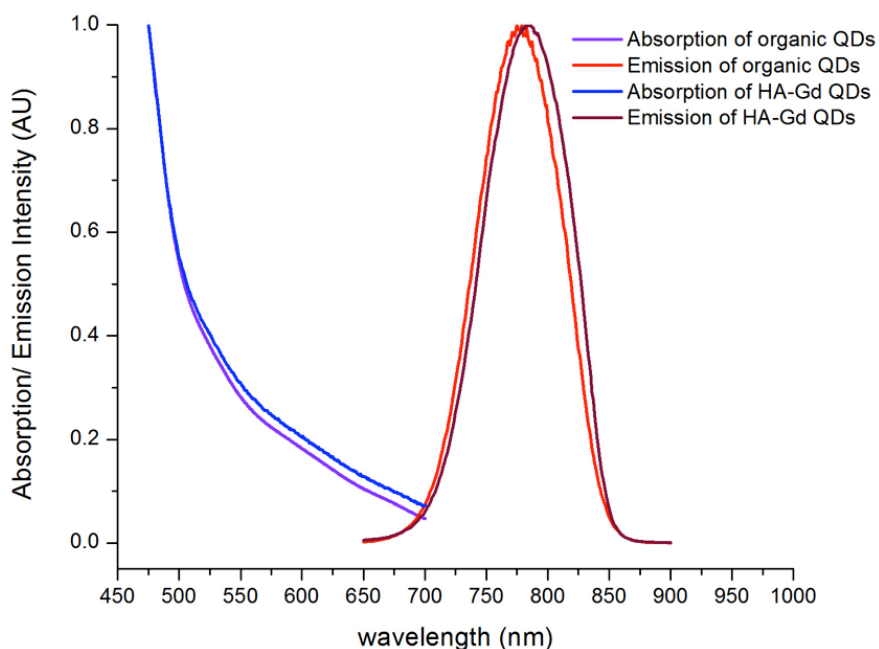


Figure 4.11. UV-absorption and Fluorescence image of QDs and HA-QDs

A typical TEM image of NIR QDs in decane was shown in Figure 4.12 A, where the as-prepared HA-Gd QDs was shown in figure B. The HA-Gd QDs exhibited a triangle-like geometry with a diameter of ~ 10 nm, and were highly dispersible in water. The surface conjugation of QDs with DTPA and further Gd^{3+} chelation did not obviously affect the morphology of QDs, as evidenced by the TEM images.

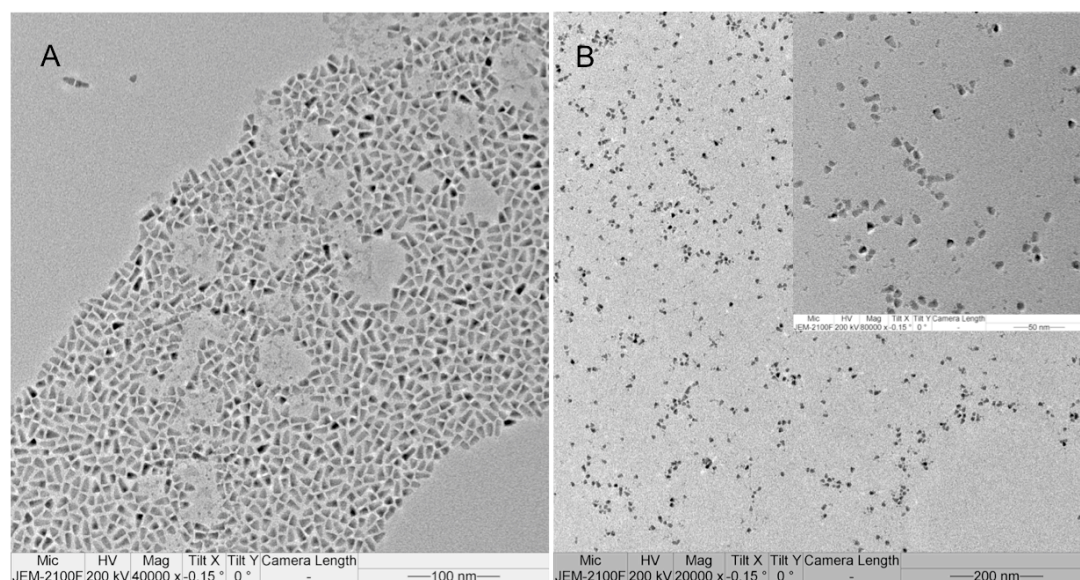


Figure 4.12. TEM figures of QDs in decane (A) and HA-Gd QDs (B)

Gd content determination of HA-DTPA Gd QDs by ICP-AES

200 μl HA-DTPA Gd QDs were used for ICP-AES. Typically, 200 μl QDs were diluted with 5ml HNO_3 and stay overnight. The second day 2 ml perchloric acid were added and the whole solution was heated to 170 $^\circ\text{C}$ for 1.5h. Finally, the solution was cooled to room temperature and pure water was added to 10ml for ICP-AES. After running ICP-AES, the Gd content in solution is 0.781 $\mu\text{g/ml}$. therefore, there were total 7.81 μg Gd in 10ml solution. Namely, in 200 μl QDs, the Gd content is 7.81 μg / (157.25g/mol) = 0.0497 μmol = 49.7 nmol.

The concentration of Gd is 49.7nmol / 200 μl = 2.485×10^{-4} mol/L = 248.5 μM . The concentration of QDs was determined by UV-vis absorption, which is 123.23 nM. Therefore, there were 248.5 / 123.23 * 1000 = 2016 Gd ions per QD.

Calculation of longitudinal relaxation rate

T1-weighted MR images of the HA-Gd QDs according to the Gd concentration are presented in Figure 4.13. As the Gd concentration increased, the MR signals also strengthened, which can be seen by the brightness.

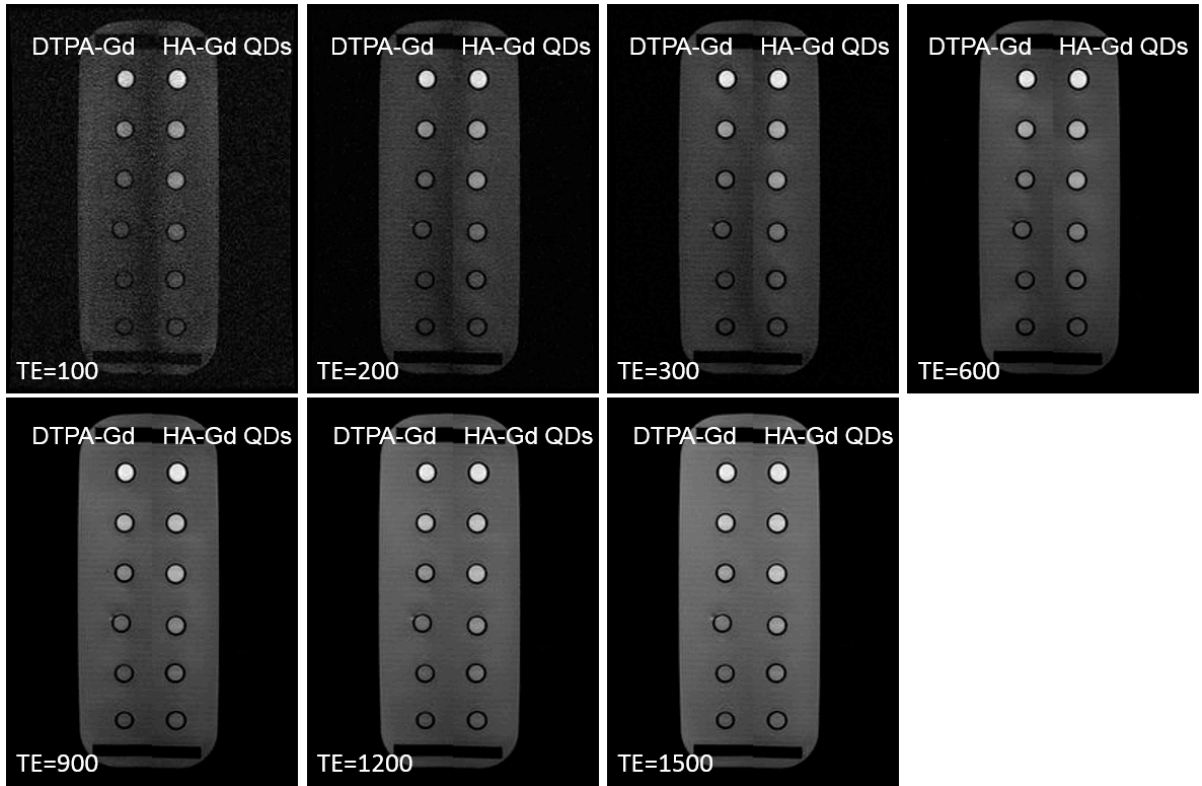


Figure 4.13. T1-weighted MR images of HA-Gd QDs and DTPA-Gd solution at different TE value

According to the T1 calculation equation:

$$S_{SE}(TR, TE) = N(H) [1 - 2e^{-(TR-TE/2)/T_1} + e^{-(TR/T_1)}] e^{-(TE/T_2)} \quad (4.1)$$

SE refers to the Spin Echo, TR refers to Time of Repetition and TE refers to Time of Echo. For the calculation of T1, We can use any two S_{SE} value such as S1 and S2, by calculating the ratio of S1 and S2,

$$\frac{S_1}{S_2} = \frac{1 - 2e^{-(TR_1-TE/2)/T_1} + e^{-(TR_1/T_1)}}{1 - 2e^{-(TR_2-TE/2)/T_1} + e^{-(TR_2/T_1)}} \quad (4.2)$$

Using the corresponding TR1 and TR2, we can get different T1 value. By calculating the average of T1, we can get T1 value at different concentrations of Gd.

Through programing on Matlab, different T1 value at different concentration were calculated. The code was as the following:

```

33
34 - IR1=[100, 200, 300, 600, 900, 1200];
35 - IR2=[200, 300, 600, 900, 1200, 1500];
36 - Se=[0.594494962, 0.708514714, 0.547839359, 0.725316543, 0.804956837, 0.839450185];
37 - IE=9;
38 - for para_previous=1:10000
39 -     SeCal1=(1-2.*exp(-(IR1-IE/2)/para_previous)+exp(-IR1/para_previous));
40 -     SeCal2=(1-2.*exp(-(IR2-IE/2)/para_previous)+exp(-IR2/para_previous));
41 -     SeCal=SeCal1./SeCal2;
42 -     y(para_previous)=sum(sqrt((Se-SeCal).^2));
43 - end
44 - plot(y);

```

Figure 4.14. The matlab code used for calculating the T1 value at different concentrations of Gd.

After running the program, a curve of y will be plotted and the minimum value at the valley will be corresponded T1 value. By calculating the average of different T1 value, we can get T1 value of different concentration.

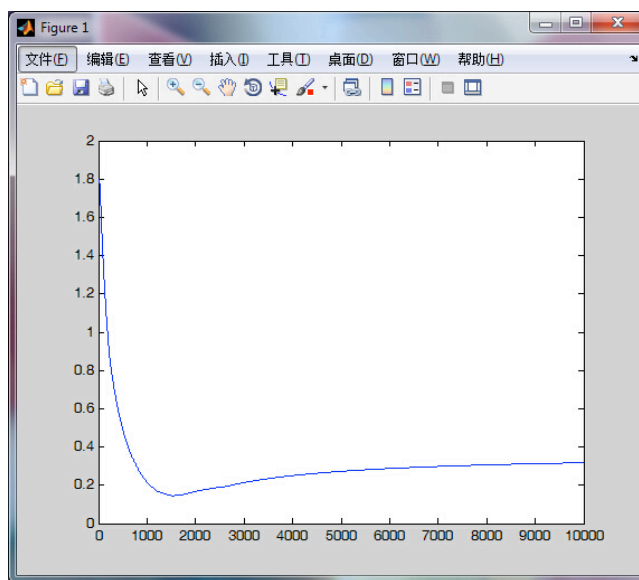


Figure 4.15. The typical curve for T1 value calculation

Quantitative analysis on Origin software showed a linear relationship between the proton longitudinal relaxation rate ($1/T1$) and Gd concentration. The linearity between T1 relaxivity ($r1$) of the HA-QDs and Gd concentration indicates that Gd^{3+} was successfully

chelated into the DTPA ligand on HA shell of the QDs. The specific relaxivity (r_1) of HA-Gd QDs was $5 \text{ mM}^{-1} \text{ s}^{-1}$, which is slightly higher than the DTPA-Gd solution.

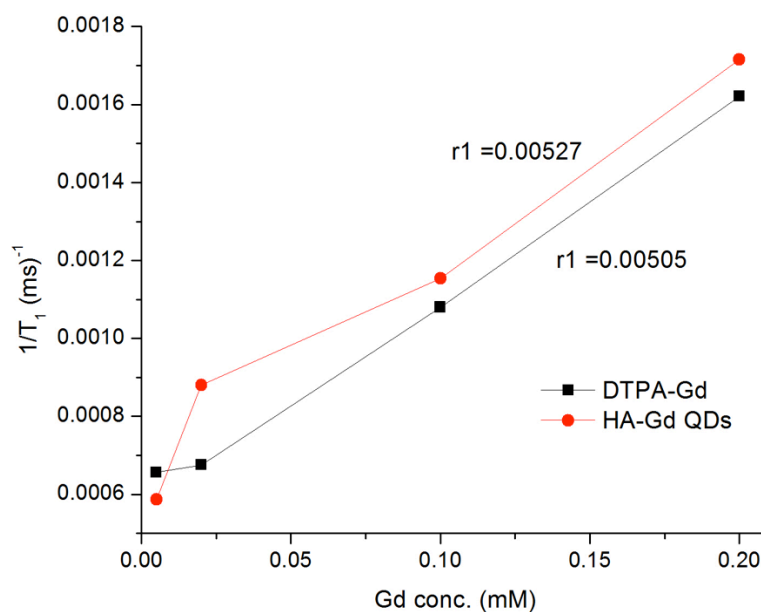


Figure 4.16. The proton longitudinal relaxation rate ($1/T_1$) according to the Gd concentration.

Biocompatibility test of HA-Gd QDs on Hela cell lines

The cytotoxicity of HA-Gd QDs was examined in cervical cancer Hela cells. QDs of different final concentrations of 1, 5, 10 nM were incubated with the cells for 1, 4 and 8 h. The experiments were performed in quintuplicated and T test was performed for each group comparing to the control group. As shown in Figure 4.17, no significant cytotoxicity was observed at all concentration and incubation time groups and the cell viability remains over 80 %. This result has proved great biocompatibility for the HA-Gd QDs, and shows the potential for *in vivo* applications in the future.

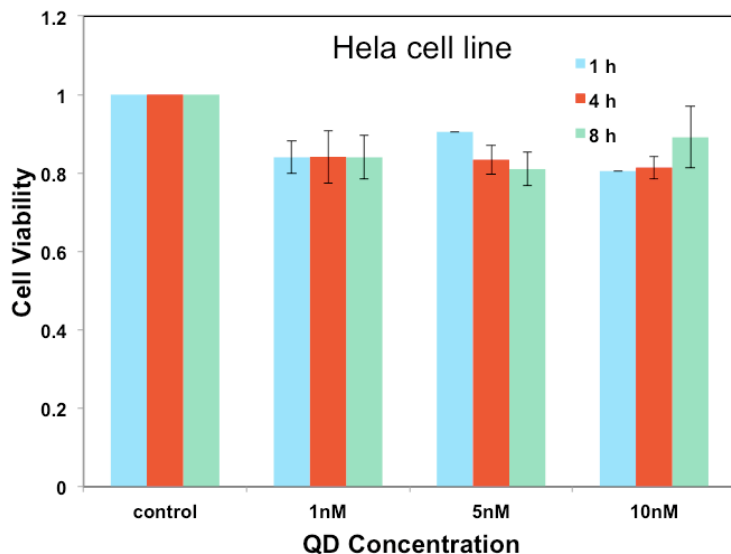


Figure 4.17. Cell viability test of HeLa cells.

In vitro cell targeted imaging

CD44⁺ HeLa cell lines were used for targeted imaging and NIH/3T3 cell line was used as a negative control. QDs with different final concentrations of 5 nM and 20 nM have been tested, and shown in Figure 4.18. Obviously, strong fluorescence on HeLa cell lines was observed but no fluorescence on NIH/3T3 cell line can be seen. This result not only demonstrates the HA-Gd polymer coated QDs still remains the targeted ability for CD44⁺ cancer cells, but also indicates very little non-specific cellular binding for NIH/3T3 cell.

In vivo Tumor-targeted fluorescence imaging

The HA-Gd QDs was prepared with the final concentration of 50 nM in PBS buffer and administered intravenous injection (200 μ L per mouse) into the nude mice bearing subcutaneous HeLa tumors. An animal FL imaging system was used to take the fluorescence images. We set the GFP excitation filter (FF01-466/40-25) and the Cy7 emission filter (FF02-809/81-25) to take the fluorescence images. The pictures of HA-Gd QDs solution in tube before injection was shown in Figure 4.19. Figure 4.19 (A)

shows the bright field image while B is the fluorescence image. Figure 4.19 (C) was the overlay of the bright field and fluorescence images.

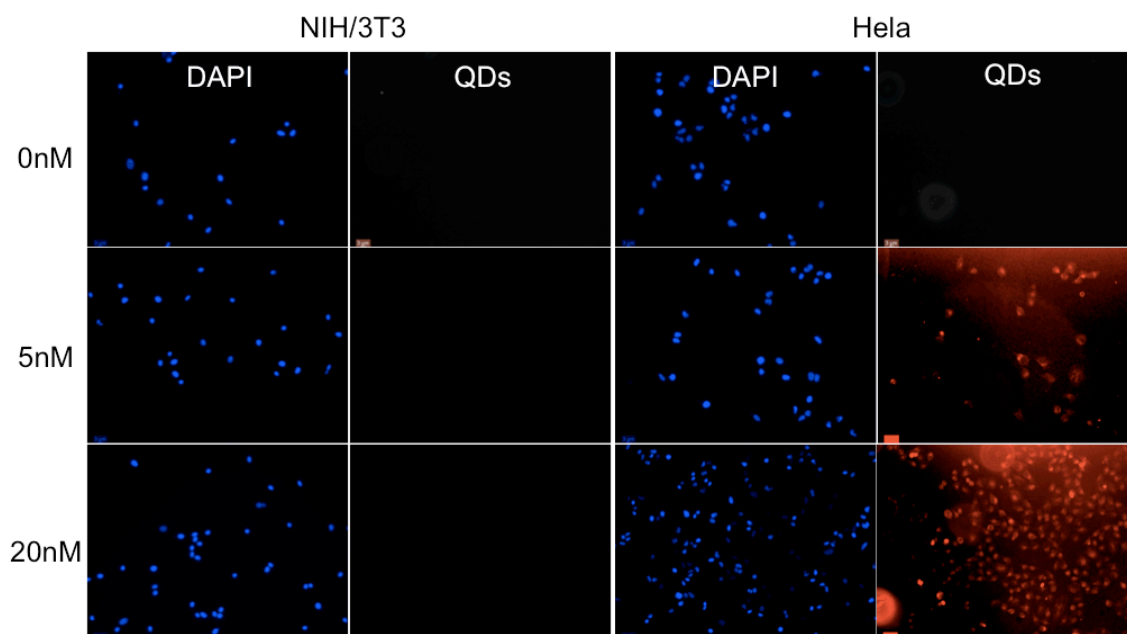


Figure 4.18. Fluorescence microscopic images of HeLa and NIH/3T3 cells labeled with HA-Gd QDs.

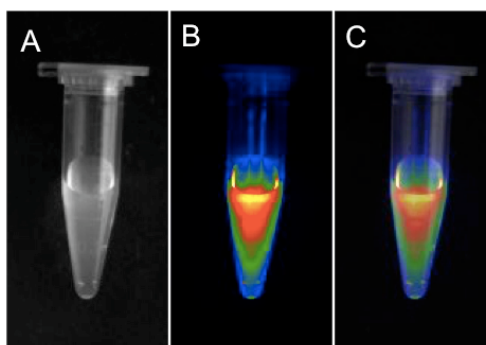


Figure 4.19. The HA-Gd QDs that was used to inject the mouse (A) Bright field image. (B) Fluorescence image. (C) Overlay of the bright field and fluorescence images.

As shown in Figure 4.20, a series of *in vivo* images detected by the animal fluorescence imaging system at different time was taken. The fluorescent background as

a control prior to injection was collected first (Fig 4.20 (A)). After HA-Gd QDs was injected through the tail vein, fluorescence images of the mouse were collected at 1 h, 2 h, 3 h and 6 h, respectively. The images indicated that fluorescence signal was observed in the tumor after 1 h (Figure 4.20 (B)). During the 2 h time intervals, there was an obvious increase area of fluorescence signal in tumor site, indicating highly specific tumor targeting of HA-Gd QDs. After 3 h, the fluorescence showed slightly decrease. By reviewing the literatures of QDs *in vivo* tumor-targeted imaging, most of the QDs started to accumulate at the tumor sites around 1-2 hours [6, 11, 197, 231-237], which coincide with our results.

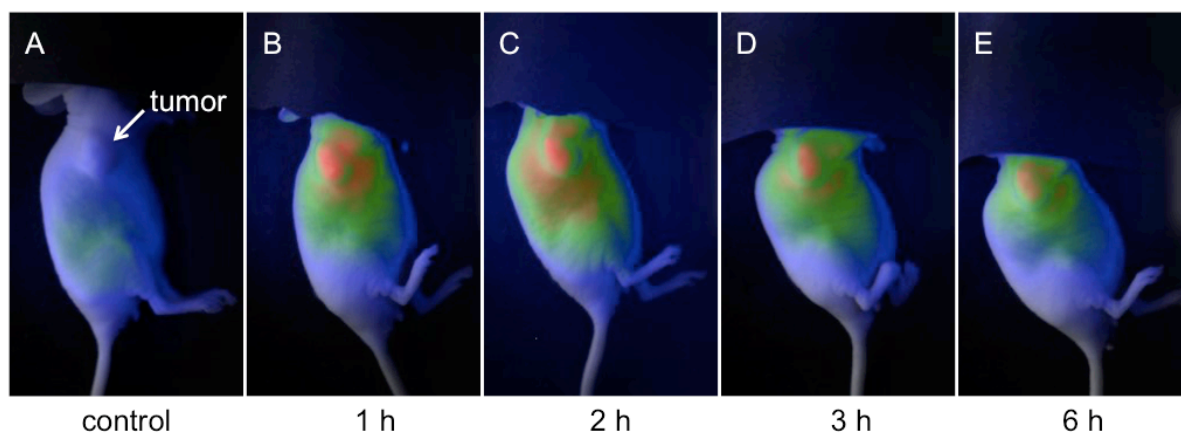


Figure 4.20. In vivo fluorescence imaging of HeLa tumor-bearing mice injected with HA-Gd QDs. (A) before injection (B) 1 h (C) 2 h (D) 3 h (E) 6 h after HA-Gd QDs was injected. The figures are the merged images of bright field and fluorescence images. All of the images were taken under the same condition.

To verify the information collected from the *in vivo* fluorescence images, the mouse was sacrificed after 24 hours. The tumor and organs (liver, spleen, heart, lung and kidney) of the mouse were taken out and the fluorescence image was acquired, which was shown in Figure 4.21. Fluorescence intensity in tumor tissues and liver was stronger than other tissues (heart, kidney, spleen and lung).

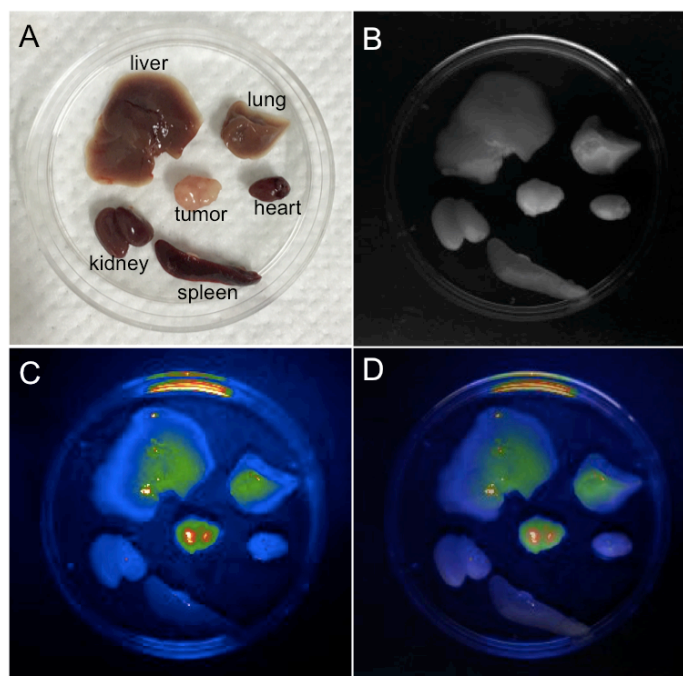


Figure 4.21. The fluorescence image of the tumor and organs of the mouse. (A) photo to show the organs and tumor. (B) Bright field image. (C) Fluorescence image. (D) Overlay of the bright field and fluorescence images.

In vivo Tumor-targeted MRI imaging

The *in vivo* MRI imaging was performed in mice bearing transplanted HeLa tumor. The HA-Gd QDs (50nM QDs concentration, 100 μ M Gd concentration, 200 μ L) was injected into mice through tail vein. The MR images were acquired before injection and at 1 h after injection as illustrated in Figure 4.22. The positions of tumor were indicated by arrow. A significant contrast enhancement of the whole body and tumor tissue was observed at 1 h after injection on the MRI image. These *in vivo* experiments showed that the HA-Gd conjugated QDs selectively target CD44 overexpressed tumor after systemic administration and are sufficient to contrast the CD44 expression in tumor lesions using both T₁ MRI sequence and Fluorescence modalities.

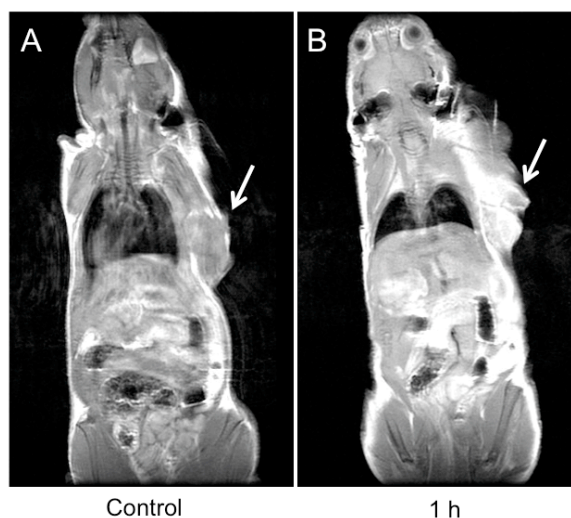


Figure 4.22. T1-weighted MR images of the mice bearing HeLa tumor (as indicated by arrow) following tail vein injection of HA-Gd QDs obtained at 0 h (before injection, Figure A) and 1 h (Figure B) after injection.

4.2.3 Summary

As a summary, we have successfully conjugated HA-cysteamine polymer with DTPA via the formation of ester bonds between the carboxyl group in DTPA and the hydroxyl group in the HA backbone and the HA-cysteamine DTPA polymer was used to coat NIR QDs. The QDs has the binding ability of Gd through the DTPA group. The Gd ion conjugation provides ability for MRI imaging and the calculated longitudinal relaxation rate is comparable with DTPA-Gd solution. Therefore, dual-modality MRI/optical imaging probes can be realized through this novel method. The resulting QDs have great water solubility, and excellent colloidal stability and also show great biocompatibility and no significant toxicity to NIH/3T3 fibroblast cells and HeLa cervical cancer cells. Moreover, the HA polymer-coated QDs hold CD44⁺ cancer cell targeting ability for cervical cancer cell lines. Besides, the carboxyl groups on the polymer backbone also allow for further functionalization and conjugation with other targeting probes like ligands or antibodies. Therefore, the HA-DTPA Gd polymer coated QDs can be applied for dual-modality MRI/optical imaging and can be used for variety of

biomarkers detection such as multi-plexed biomarker staining and for *in vivo* molecular imaging as well as targeted drug delivery.

4.3 HA-DOTA-Cu QDs for dual-modality optical/PET imaging

4.3.1 Materials and Methods

Materials

Sodium hyaluronate with MW of 6300 was purchased from Lifecore (USA). Cystamine dihydrochloride, dithiothreitol (DTT), IGEPAL CO-520, tetramethylammonium hydroxide (TMAH) were purchased from Sigma-Aldrich. NIR QDs were purchased from Invitrogen. EDC and sulfo-NHS were purchased from Pierce. tetra-azacyclododecanetetra-acetic acid (DOTA) were purchased from STREM chemicals. dry DMSO were provided by J&K Scientific. Cyclohexane, Methanol, Ethanol and other solvent were purchased from Sinopharm Chemical Reagent Beijing. Dialysis tube (MWCO 1000) was purchased from Spectrum Labs. UV–Vis absorption spectra were obtained using a UV-2550 UV-vis spectrophotometer (Shimadzu). The fluorescence spectrum was recorded on a Nanolog FL3-2iHR (HORIBA JOBIN). The structural details of the nanoparticles were analyzed by the HRTEM method using a JEM-2100F at Peking University. NMR spectrum were performed on a 400Hz NMR machine at the NMR imaging center of Peking University. Copper contents were estimated on an inductive coupled plasma-optical emission spectrometry (PROFILE SPEC, Leeman Labs, USA).

Methods

Synthesis of HA-cystamine-DOTA polymer

As shown in Figure 4.23, the synthesis of HA-cysteamine-DOTA polymer involves three steps: synthesis of HA-cystamine polymer, DOTA conjugation to the HA-cystamine polymer and DTT reduction of the disulfide bond.

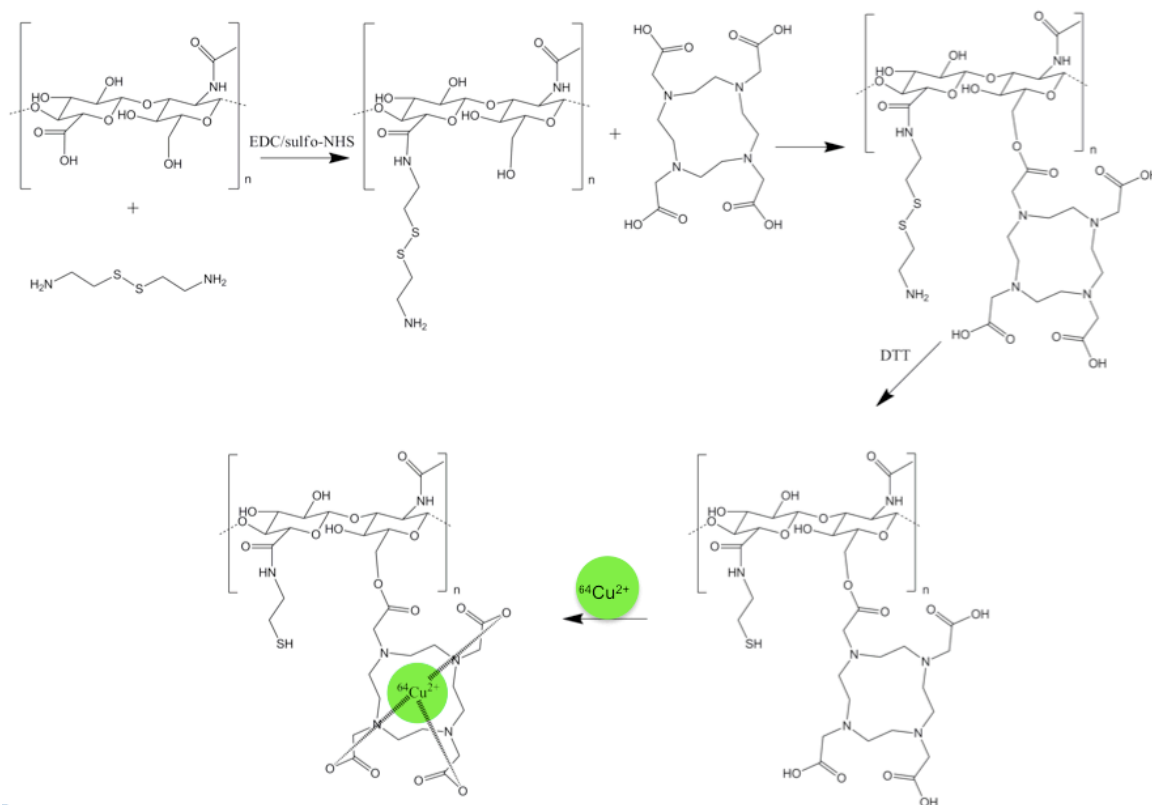


Figure 4.23. Synthesis routes of HA-DOTA polymer

Typically, sodium hyaluronate with average MW of 6276 was dissolved in PBS to about 10 mg/ml, then 17 molar excess of EDC, and final concentration of 5mM sulfo-NHS were added to the HA sodium salt solution. The solution was stirred for 15min to activate the carboxyl groups on HA polymer. Then 30 molar excess of cystamine dihydrochloride in PBS were added, and the mixture was kept reacting at room temperature for 24 h. The HA-cystamine product was purified by dialysis against pure water using dialysis tube (molecular weight cut-off, 1kDa) for 2 days and lyophilized to get the dry HA-cystamine product. The HA-cystamine conjugation was confirmed by ^1H NMR on a 400MHz machine.

Table 4.4. Typical amount for HA-cystamine synthesis.

Reagent	Equivalent	Amount (μmol)	Molecular weight (g/mol)	weight (mg)	volume (ml)	
Hyaluronic acid sodium salt	1	39.8	6276	250	23	in PBS
COOH	17	677.2				
EDC	30	1195.0	191.7	229.1	1	
sulfo-NHS		125	217.13	27.1	1	
Cystamine dihydrochloride	30	1195.0	225.2	269.1	0	
					25	in PBS

According to previously reported method [229, 230], DOTA was conjugated to the HA backbone by the formation of ester bonds between the carboxyl group in DOTA and the hydroxyl group in the HA backbone. Typically, 40 molar excess of DOTA and HA-cystamine were dissolved in 50 ml of anhydrous dimethyl sulfoxide and protected with a drying tube containing calcium chloride inside. The mixture was stirred for 24 h at room temperature, and after the reaction, 25 ml of pure water was slowly added to the solution. The resulting solution was placed in a dialysis bag (molecular weight cut-off, 1kDa) and dialyzed against pure water for 2 days. The dialysis product was lyophilized and the HA-cysteamine-DOTA product was obtained as a powder.

The conjugation of DOTA to HA was confirmed via fourier transform infrared spectrometry (FT-IR) on a VECTOR22 (Bruker, Germany). Spectra was recorded on KBr plates over the range $4000\sim 400\text{ cm}^{-1}$ at a wavenumber resolution of 1 cm^{-1} . To determine the amount of DOTA that was conjugated to HA, NMR was also conducted on a 400MHz NMR machine.

Table 4.5. Typical amount for HA-cystamine conjugating DOTA.

Reagent	Equivalent	Amount(μ mol)	Molecular weight (g/mol)	weight (mg)	volume (ml)	
HA-cystamine	1	7.97	6276	50	50	in DMSO
DOTA	40	318.7	404.42	128.9		

Next for DTT reduction of the disulfide bond on cystamine, DTT of a final concentration of 80mM was added and the whole solution was shaken for 24 h. After dialyzing against water through 1000 MWCO tube for 1 day, 5~10 mg DTT was added to the solution to protect the free thiol groups. After lyophilizing, the HA-cystamine-DOTA polymer was collected as powder.

HA-DOTA polymer for Cu coupling and QDs coating

As HA-DOTA polymer will be used for isotope Cu coupling, so Cu coupling and QDs coating were finished in one step in order to reduce the time for purifying the QDs. Typically, 1mg HA-DOTA polymer were conjugated with 10 μ l CuCl₂ (10 mg/ml in water) and 40 μ l H₂O solution for 1h (37°C). Then the QDs were coated with the HA-DOTA Cu polymer. Typically 50 μ l of 1 μ M QDs in decane was diluted with 4.5ml cyclohexane and 0.5ml IGEPAL 520 was added. The 1mg HA-DOTA Cu polymer in 50 μ l water was then added to the solution and 50 μ l 0.1M TMAH in methanol was also added as a catalyst. The mixture was vortexed for 1 min, and shaken for 60 min. After reaction, 1 ml ethanol was added and the solution was centrifuged at 6000g for 5 min to precipitate the HA polymer-coated QDs. The pellets were washed with additional ethanol for 3 times and washed with water once and finally re-dispersed in water. After centrifuging the QDs solution at 5000 g for 5 min to get rid of the undissolved parts, the supernatant which contains the HA polymer-coated QDs was purified using a 0.22 μ m syringe filter.

For characterization, the UV-vis absorption spectrum was recorded on a UV-2550 UV-vis spectrophotometer (Shimadzu). The fluorescence spectrum was recorded on a Nanolog FL3-2iHR (HORIBA JOBIN). The TEM was performed on a JEM-2100F TEM machine. The Cu contents were estimated on an inductive coupled plasma-optical emission spectrometry (PROFILE SPEC, Leeman Labs, USA) by digesting QDs with HNO_3 and perchloric acid.

4.3.2 Results and Discussions

Characterization of HA-cystamine-DOTA polymer

The synthesis of HA-cystamine-DOTA polymer involves three steps: synthesis of HA-cystamine polymer, DOTA conjugation to the HA-cystamine polymer and DTT reduction of the disulfide bond.

For the HA-cystamine polymer conjugate DOTA, from the FT-IR image of HA-cystamine-DOTA (Figure 4.24), the peak at 1730cm^{-1} which represents the C=O formation is a strong sign that DOTA was successfully conjugated to the HA backbone.

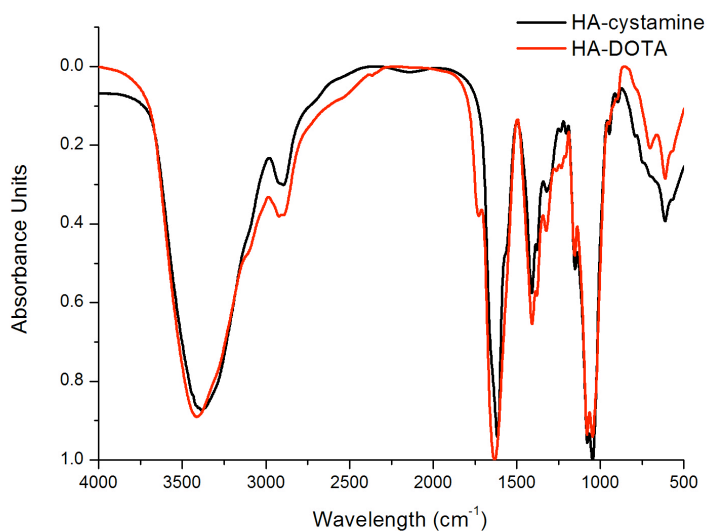


Figure 4.24. FT-IR image of HA and HA-cystamine-DOTA

The HA-cystamine conjugation was confirmed by NMR. As shown in Figure 4.25, the comparison of HA and HA-cystamine-DOTA, the peak at around 2.85 ppm and 2.95 ppm which is the cystamine was shown, which proved successful conjugation of cystamine to HA polymer. Quantitative characterization of DOTA that was conjugated to HA-cystamine polymer was also confirmed by NMR. The NMR curve was shown in Figure 4.25, and the NMR prediction by chemdraw was shown in Figure 4.26. The circles of the same color represents the corresponded group. The amount of DOTA that was conjugated to HA can be calculated from the integration of the corresponding part on the NMR curve. After calculation, there were 1 DOTA on every 3 HA polymer.

Characterization of HA-DOTA-Cu polymer coated QDs

UV-absorption and Fluorescence curve before and after HA-DOTA-Cu polymer coating were shown in Figure 4.27. The QDs absorption and emission curve after HA-DOTA-Cu polymer coating keeps the same shape as before coating, thus indicates a good stability of the HA-DOTA-Cu polymer coated QDs.

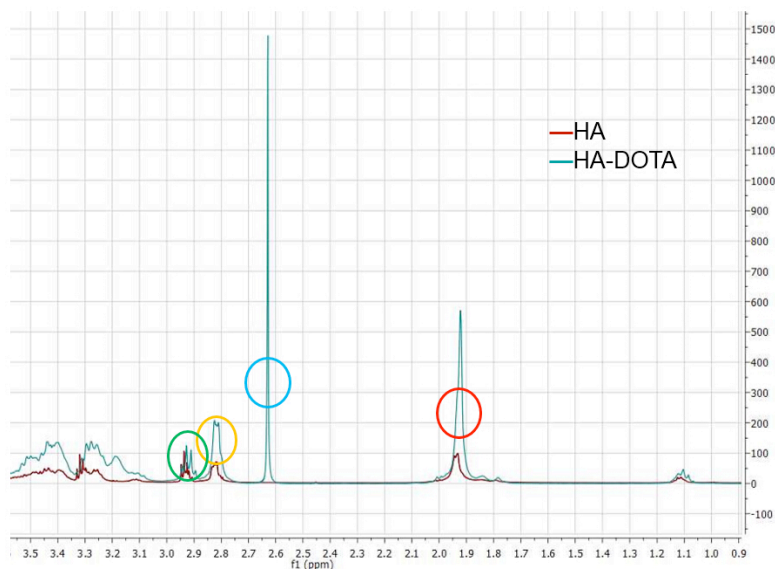


Figure 4.25. NMR of HA-cystamine-DOTA and HA.

TEM results were shown in Figure 4.28. From the TEM, we can get the average size of the QDs was around 10 nm. The HA-DOTA Cu QDs distributed uniformly in size, which proves a well disperse in water. The surface conjugation of QDs with DOTA and further Cu ion chelation did not obviously affect the morphology of QDs, as evidenced by the TEM images.

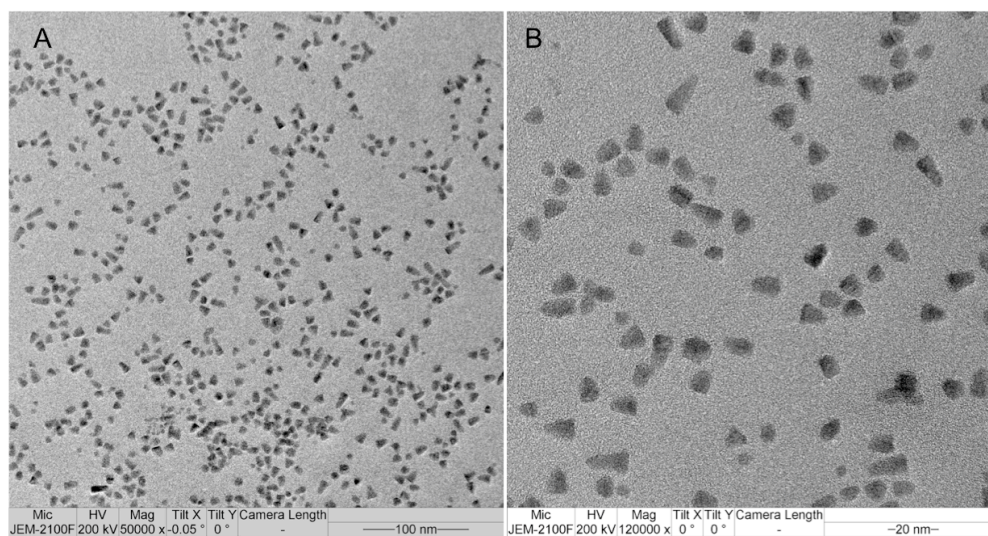


Figure 4.28. TEM figure of HA-DOTA Cu QDs to show a size distribution.

Cu content determination of HA-DOTA Cu QDs by ICP-AES

100 μ l HA-DOTA Cu QDs were used for ICP-AES. Typically, 100 μ l QDs were diluted with 5ml HNO₃ and stay overnight. The second day 2 ml perchloric acid were added and the whole solution was heated to 170 $^{\circ}$ C for 1.5h. Finally, the solution was cooled to room temperature and pure water was added to 10ml for ICP-AES. After running ICP-AES, the Cu content in solution is 0.0571 μ g/ml. therefore, there were total 0.571 μ g Cu in 10ml solution. Namely, in 100 μ l QDs, the Cu content is 0.571 μ g / (64g/mol) = 0.0089 μ mol = 8.9nmol.

The concentration of Cu is 8.9nmol / 100 μ l = 8.9*10⁻⁵ mol/L = 89 μ M. The concentration of QDs was determined by UV-vis absorption, which is 74nM. Therefore, there were 89 / 74 * 1000 = 1203 Cu ions per QD.

4.3.3 Summary

In this part, we have successfully conjugated HA-cysteamine polymer with DOTA via the formation of ester bonds between the carboxyl group in DOTA and the hydroxyl group in the HA backbone and the HA-cysteamine DOTA polymer was used to coat NIR QDs. The resulting QDs have great water solubility and excellent colloidal stability. The QDs also has the binding ability of Cu through the DOTA group, and ICP-AES results shows a relatively high amount of Cu content in the HA-DOTA Cu QDs. The preliminary results provide a future application for coupling ^{64}Cu isotopes for PET imaging. Therefore, dual-modality PET/optical imaging probes can be realized through this novel method.

4.4 Summary

In this chapter, the Hyaluronic acid-cysteamine polymer was conjugated with DTPA and DOTA for multi-modality MRI/optical and PET/optical imaging. The DTPA can conjugate Gd ion thus provides ability for MRI imaging and the calculated longitudinal relaxation rate is comparable with DTPA-Gd solution. The DOTA unit renders the QDs to have the ability for conjugating Cu ion, which provides future ability for ^{64}Cu isotope coupling for PET imaging. The resulting QDs have great water solubility, and excellent colloidal stability and also show great biocompatibility and no significant toxicity to NIH/3T3 fibroblast cells and Hela cervical cancer cells. Moreover, the HA polymer-coated QDs hold CD44⁺ cancer cell targeting ability for cervical cancer cell lines. The HA-DTPA polymer can also conjugate $^{99\text{m}}\text{Tc}$ for SPECT imaging. Therefore, this novel HA-DTPA and HA-DOTA polymer holds the promise for multi-modality imaging, such as MRI/optical, PET/optical, SPECT/optical and

MRI/PET/SPECT/optical imaging and will have a significant impact on cancer diagnostics, molecular profiling, and the integration of different modality imaging.

CHAPTER 5

SUMMARY

As a summary, we have successfully developed a novel HA-cysteamine polymer coated QDs, which are water-soluble, and stable for long time and over a large pH, range. The polymer coated QDs shows great biocompatibility and no significant toxicity. Moreover, the HA-cysteamine polymer coated QDs holds CD44⁺ cancer cell targeting ability for breast cancer cell lines. Based on this well-designed system, the Hyaluronic acid-cystamine polymer was further conjugated with DTPA and DOTA for multi-modality MRI/optical and PET/optical imaging. The DTPA can conjugate Gd ion provides ability for MRI imaging and the calculated longitudinal relaxation rate is comparable with DTPA-Gd solution. The DOTA unit renders the QDs to have the ability for conjugating Cu ion, which provides future ability for ⁶⁴Cu isotope coupling for PET imaging. The resulting QDs have great water solubility, and excellent colloidal stability and also show great biocompatibility and no significant toxicity to NIH/3T3 fibroblast cells and Hela cervical cancer cells. Moreover, the HA polymer-coated QDs hold CD44⁺ cancer cell targeting ability for cervical cancer Hela cell lines. The HA-DTPA polymer can also conjugate ^{99m}Tc for SPECT imaging. The QDs core can also be replaced with Au nanoparticles, which is suitable for CT enhancement imaging. Therefore, this novel HA-DTPA and HA-DOTA polymer holds the promise for multi-modality imaging, such as MRI/optical, MRI/CT, PET/optical, SPECT/optical and PET/CT/SPECT imaging. We expect this versatile method will have a significant impact on cancer diagnostics, molecular profiling, and the integration of different modality imaging.

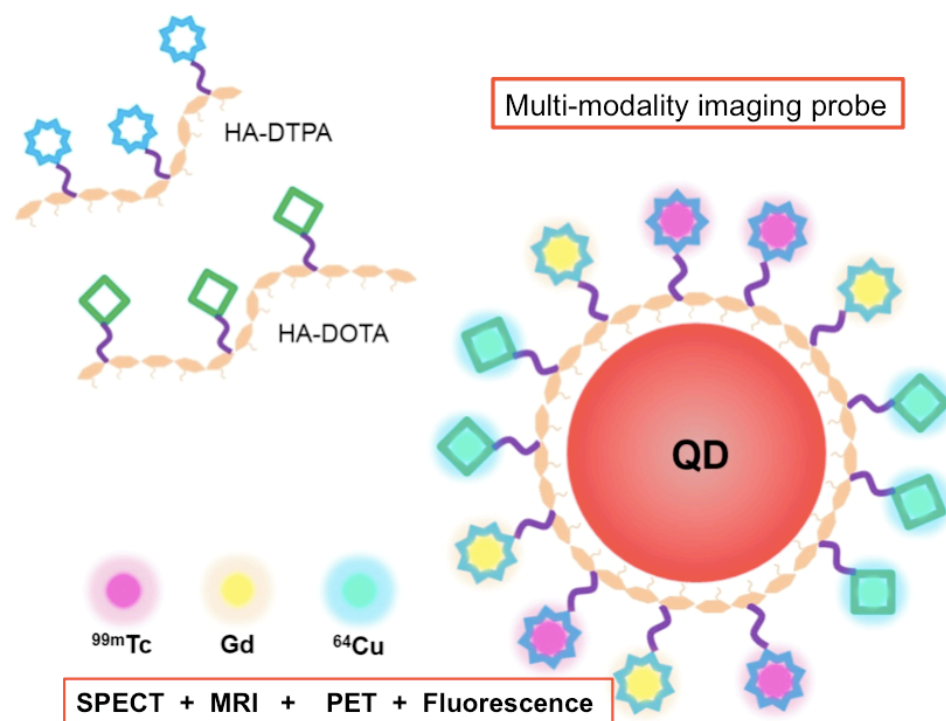


Figure 5.1 Multi-modality imaging probe based on our HA-cystamine QDs system

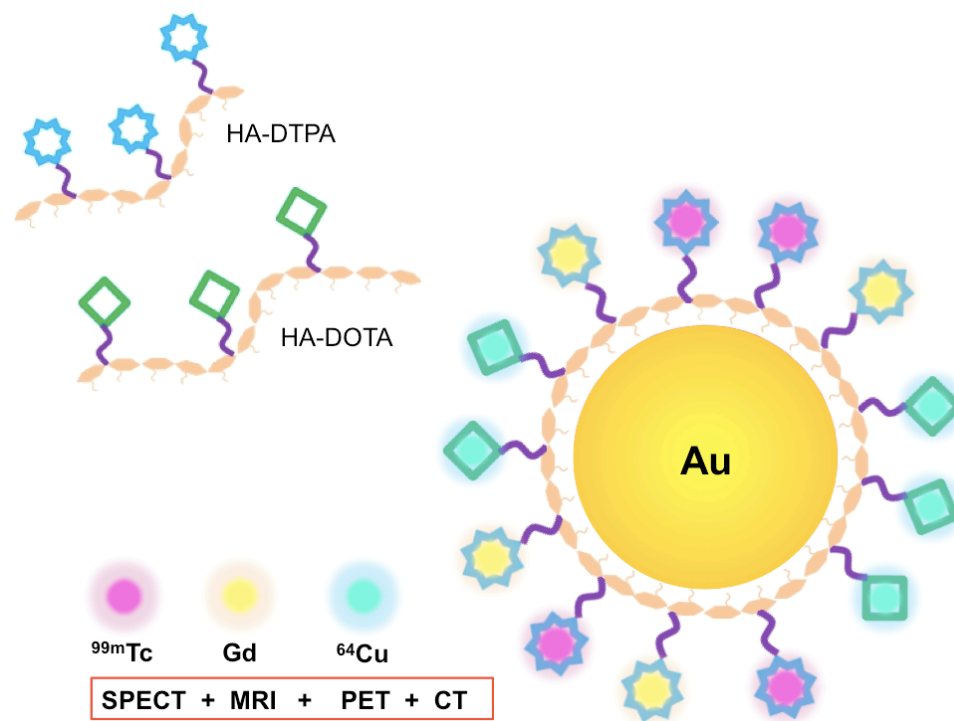


Figure 5.2 Multi-modality imaging probe based on our HA-cystamine Au NP system

REFERENCES

1. WHO, *2014 World Cancer Report*. 2014.
2. Medintz, I.L., et al., *Quantum dot bioconjugates for imaging, labelling and sensing*. Nature Materials, 2005. **4**(6): p. 435-446.
3. Wu, X., et al., *Immunofluorescent labeling of cancer marker Her2 and other cellular targets with semiconductor quantum dots*. Nat Biotech, 2003. **21**(1): p. 41-46.
4. Smith, A.M., et al., *Bioconjugated quantum dots for in vivo molecular and cellular imaging*. Advanced drug delivery reviews, 2008. **60**(11): p. 1226-1240.
5. Yezhelyev, M.V., et al., *In situ molecular profiling of breast cancer biomarkers with multicolor quantum dots*. Advanced Materials, 2007. **19**(20): p. 3146-+.
6. Gao, X., et al., *In vivo cancer targeting and imaging with semiconductor quantum dots*. Nature biotechnology, 2004. **22**(8): p. 969-976.
7. Michalet, X., et al., *Quantum Dots for Live Cells, in Vivo Imaging, and Diagnostics*. Science, 2005. **307**(5709): p. 538-544.
8. Pereira, R.F. and P.J. Bartolo, *3D bioprinting of photocrosslinkable hydrogel constructs*. Journal of Applied Polymer Science, 2015. **132**(48).
9. Posocco, B., et al., *Polysaccharides for the Delivery of Antitumor Drugs*. Materials, 2015. **8**(5): p. 2569-2615.
10. Choi, K.Y., et al., *Versatile RNA Interference Nanoplatfom for Systemic Delivery of RNAs*. ACS Nano, 2014. **8**(5): p. 4559-4570.
11. Kim, K.S., et al., *Bioimaging for Targeted Delivery of Hyaluronic Acid Derivatives to the Livers in Cirrhotic Mice Using Quantum Dots*. ACS Nano, 2010. **4**(6): p. 3005-3014.
12. Xing, Y., et al., *Radiolabeled Nanoparticles for Multimodality Tumor Imaging*. Theranostics, 2014. **4**(3): p. 290-306.
13. Lu, Y., et al., *An Integrated Quad-Modality Molecular Imaging System for Small Animals*. Journal of Nuclear Medicine, 2014. **55**(8): p. 1375-1379.
14. Louie, A., *Multimodality imaging probes: design and challenges*. Chem Rev, 2010. **110**(5): p. 3146-95.

15. Louie, A.Y., *Multimodality Imaging Probes: Design and Challenges*. Chemical Reviews, 2010. **110**(5): p. 3146-3195.
16. Zhang, F., et al., *Facile synthesis of functional gadolinium-doped CdTe quantum dots for tumor-targeted fluorescence and magnetic resonance dual-modality imaging*. Journal of Materials Chemistry B, 2014. **2**(41): p. 7201-7209.
17. Hu, K.Z., et al., *In Vivo Cancer Dual-Targeting and Dual-Modality Imaging with Functionalized Quantum Dots*. Journal of Nuclear Medicine, 2015. **56**(8): p. 1278-1284.
18. Varmus, H., *The new era in cancer research*. Science, 2006. **312**(5777): p. 1162-5.
19. Sherr, C.J., *Cancer cell cycles*. Science, 1996. **274**(5293): p. 1672-7.
20. Hanahan, D. and R.A. Weinberg, *The hallmarks of cancer*. Cell, 2000. **100**(1): p. 57-70.
21. Ferrari, M., *Cancer nanotechnology: opportunities and challenges*. Nature Reviews Cancer, 2005: p. 161-171.
22. Ding, K., et al., *Magnetically engineered Cd-free quantum dots as dual-modality probes for fluorescence/magnetic resonance imaging of tumors*. Biomaterials, 2014. **35**(5): p. 1608-17.
23. Cormode, D.P., et al., *Nanocrystal core high-density lipoproteins: a multimodality contrast agent platform*. Nano Lett, 2008. **8**(11): p. 3715-23.
24. Prinzen, L., et al., *Optical and magnetic resonance imaging of cell death and platelet activation using annexin a5-functionalized quantum dots*. Nano Lett, 2007. **7**(1): p. 93-100.
25. Bruchez, M., et al., *Semiconductor nanocrystals as fluorescent biological labels*. Science, 1998. **281**(5385): p. 2013-2016.
26. Chan, W.C.W., et al., *Luminescent quantum dots for multiplexed biological detection and imaging*. Current Opinion in Biotechnology, 2002. **13**(1): p. 40-46.
27. Chan, W.C.W. and S. Nie, *Quantum dot bioconjugates for ultrasensitive nonisotopic detection*. Science, 1998. **281**(5385): p. 2016-2018.
28. Cheng, Y., et al., *Convenient Generation of Quantum Dot-Incorporated Photonic Crystal Beads for Multiplex Bioassays*. Journal of Biomedical Nanotechnology, 2014. **10**(5): p. 760-766.
29. Ruan, G., et al., *Imaging and tracking of tat peptide-conjugated quantum dots in living cells: new insights into nanoparticle uptake, intracellular transport, and*

- vesicle shedding*. Journal of the American Chemical Society, 2007. **129**(47): p. 14759-14766.
30. Steponkiene, S., et al., *Cellular Uptake and Photosensitizing Properties of Quantum Dot-Chlorin e 6 Complex: In Vitro Study*. Journal of Biomedical Nanotechnology, 2014. **10**(4): p. 679-686.
 31. Wu, X., et al., *Immunofluorescent labeling of cancer marker Her2 and other cellular targets with semiconductor quantum dots*. Nature biotechnology, 2002. **21**(1): p. 41-46.
 32. Xing, Y., et al., *Bioconjugated quantum dots for multiplexed and quantitative immunohistochemistry*. Nature Protocols, 2007. **2**(5): p. 1152-1165.
 33. Zheng, H., et al., *Detection of the cancer marker CD146 expression in melanoma cells with semiconductor quantum dot label*. Journal of biomedical nanotechnology, 2010. **6**(4): p. 303-311.
 34. Leutwyler, W.K., S.L. Bürgi, and H. Burgl, *Semiconductor clusters, nanocrystals, and quantum dots*. Science, 1996. **271**: p. 933.
 35. Smith, A.M., A.M. Mohs, and S. Nie, *Tuning the optical and electronic properties of colloidal nanocrystals by lattice strain*. Nature nanotechnology, 2008. **4**(1): p. 56-63.
 36. Smith, A.M. and S. Nie, *Bright and compact alloyed quantum dots with broadly tunable near-infrared absorption and fluorescence spectra through mercury cation exchange*. Journal of the American Chemical Society, 2011. **133**(1): p. 24.
 37. Derfus, A.M., W.C. Chan, and S.N. Bhatia, *Probing the cytotoxicity of semiconductor quantum dots*. Nano letters, 2004. **4**(1): p. 11-18.
 38. Hu, X. and X. Gao, *Silica-Polymer Dual Layer-Encapsulated Quantum Dots with Remarkable Stability*. ACS nano, 2010. **4**(10): p. 6080-6086.
 39. Schroedter, A., et al., *Biofunctionalization of silica-coated CdTe and gold nanocrystals*. Nano Letters, 2002. **2**(12): p. 1363-1367.
 40. Kim, S.-W., et al., *Phosphine oxide polymer for water-soluble nanoparticles*. Journal of the American Chemical Society, 2005. **127**(13): p. 4556-4557.
 41. Pellegrino, T., et al., *Hydrophobic nanocrystals coated with an amphiphilic polymer shell: a general route to water soluble nanocrystals*. Nano Letters, 2004. **4**(4): p. 703-707.
 42. Uskoković, V. and M. Drogenik, *Synthesis of materials within reverse micelles*. Surface Review and Letters, 2005. **12**(02): p. 239-277.

43. Liu, W., et al., *Compact cysteine-coated CdSe (ZnCdS) quantum dots for in vivo applications*. Journal of the American Chemical Society, 2007. **129**(47): p. 14530-14531.
44. Smith, A.M. and S. Nie, *Minimizing the hydrodynamic size of quantum dots with multifunctional multidentate polymer ligands*. Journal of the American Chemical Society, 2008. **130**(34): p. 11278-11279.
45. Duan, H.W., M. Kuang, and Y.A. Wang, *Quantum Dots with Multivalent and Compact Polymer Coatings for Efficient Fluorescence Resonance Energy Transfer and Self-Assembled Biotagging*. Chemistry of Materials, 2010. **22**(15): p. 4372-4378.
46. Giovanelli, E., et al., *Highly Enhanced Affinity of Multidentate versus Bidentate Zwitterionic Ligands for Long-Term Quantum Dot Bioimaging*. Langmuir, 2012. **28**(43): p. 15177-15184.
47. Liu, L., et al., *Bifunctional Multidentate Ligand Modified Highly Stable Water-Soluble Quantum Dots*. Inorganic Chemistry, 2010. **49**(8): p. 3768-3775.
48. Liu, W., et al., *Compact biocompatible quantum dots via RAFT-mediated synthesis of imidazole-based random copolymer ligand*. Journal of the American Chemical Society, 2009. **132**(2): p. 472-483.
49. Palui, G., H.B. Na, and H. Mattoussi, *Poly(ethylene glycol)-Based Multidentate Oligomers for Biocompatible Semiconductor and Gold Nanocrystals*. Langmuir, 2011. **28**(5): p. 2761-2772.
50. Stewart, M.H., et al., *Multidentate Poly(ethylene glycol) Ligands Provide Colloidal Stability to Semiconductor and Metallic Nanocrystals in Extreme Conditions*. Journal of the American Chemical Society, 2010. **132**(28): p. 9804-9813.
51. Wu, Y.Z., et al., *pH-Responsive Quantum Dots via an Albumin Polymer Surface Coating*. Journal of the American Chemical Society, 2010. **132**(14): p. 5012-5014.
52. Yildiz, I., et al., *Hydrophilic CdSe–ZnS Core–Shell Quantum Dots with Reactive Functional Groups on Their Surface*. Langmuir, 2010. **26**(13): p. 11503-11511.
53. Yildiz, I., et al., *Biocompatible CdSe–ZnS Core–Shell Quantum Dots Coated with Hydrophilic Polythiols*. Langmuir, 2009. **25**(12): p. 7090-7096.
54. Zhang, P., et al., *Click-Functionalized Compact Quantum Dots Protected by Multidentate-Imidazole Ligands: Conjugation-Ready Nanotags for Living-Virus Labeling and Imaging*. Journal of the American Chemical Society, 2012. **134**(20): p. 8388-8391.

55. Cai, W., et al., *Dual-function probe for PET and near-infrared fluorescence imaging of tumor vasculature*. J Nucl Med, 2007. **48**(11): p. 1862-70.
56. Schipper, M.L., et al., *microPET-based biodistribution of quantum dots in living mice*. J Nucl Med, 2007. **48**(9): p. 1511-8.
57. Jin, T., et al., *Gd³⁺-functionalized near-infrared quantum dots for in vivo dual modal (fluorescence/magnetic resonance) imaging*. Chem Commun (Camb), 2008(44): p. 5764-6.
58. Koole, R., et al., *Paramagnetic lipid-coated silica nanoparticles with a fluorescent quantum dot core: a new contrast agent platform for multimodality imaging*. Bioconjug Chem, 2008. **19**(12): p. 2471-9.
59. Van Schooneveld, M.M., et al., *Improved biocompatibility and pharmacokinetics of silica nanoparticles by means of a lipid coating: a multimodality investigation*. Nano Lett, 2008. **8**(8): p. 2517-25.
60. Lee, J.H., et al., *Dual-mode nanoparticle probes for high-performance magnetic resonance and fluorescence imaging of neuroblastoma*. Angew Chem Int Ed Engl, 2006. **45**(48): p. 8160-2.
61. Gold, M.H., *Use of hyaluronic acid fillers for the treatment of the aging face*. Clinical interventions in aging, 2007. **2**(3): p. 369.
62. Kerscher, M., J. Bayrhammer, and T. Reuther, *Rejuvenating influence of a stabilized hyaluronic acid-based gel of nonanimal origin on facial skin aging*. Dermatologic Surgery, 2008. **34**(5): p. 720-726.
63. Jang, Y.L., et al., *Hyaluronic Acid-siRNA Conjugate/Reducible Polyethylenimine Complexes for Targeted siRNA Delivery*. Journal of Nanoscience and Nanotechnology, 2014. **14**(10): p. 7388-7394.
64. Wang, T.W., et al., *The effect of gelatin-chondroitin sulfate-hyaluronic acid skin substitute on wound healing in SCID mice*. Biomaterials, 2006. **27**(33): p. 5689-5697.
65. Platt, V.M. and F.C. Szoka Jr, *Anticancer therapeutics: targeting macromolecules and nanocarriers to hyaluronan or CD44, a hyaluronan receptor*. Molecular pharmaceutics, 2008. **5**(4): p. 474-486.
66. Luo, Y. and G.D. Prestwich, *Synthesis and selective cytotoxicity of a hyaluronic acid-antitumor bioconjugate*. Bioconjugate chemistry, 1999. **10**(5): p. 755-763.
67. Coradini, D., et al., *Hyaluronic acid as drug delivery for sodium butyrate: Improvement of the anti-proliferative activity on a breast-cancer cell line*. International journal of cancer, 1999. **81**(3): p. 411-416.

68. Yadav, A.K., P. Mishra, and G.P. Agrawal, *An insight on hyaluronic acid in drug targeting and drug delivery*. Journal of drug targeting, 2008. **16**(2): p. 91-107.
69. Hosseinkhani, H., et al., *Biodegradable nanoparticles for gene therapy technology*. Journal of Nanoparticle Research, 2013. **15**(7): p. 1-15.
70. Jiang, G., et al., *Target specific intracellular delivery of siRNA/PEI- HA complex by receptor mediated endocytosis*. Molecular pharmaceutics, 2009. **6**(3): p. 727-737.
71. Lee, H., et al., *Target-specific intracellular delivery of siRNA using degradable hyaluronic acid nanogels*. Journal of controlled release, 2007. **119**(2): p. 245-252.
72. Chen, B., R.J. Miller, and P.K. Dhal, *Hyaluronic Acid-Based Drug Conjugates: State-of-the-Art and Perspectives*. Journal of Biomedical Nanotechnology, 2014. **10**(1): p. 4-16.
73. Saravanakumar, G., et al., *Hyaluronic Acid-Based Conjugates for Tumor-Targeted Drug Delivery and Imaging*. Journal of Biomedical Nanotechnology, 2014. **10**(1): p. 17-31.
74. Mi, P., et al., *Gd-DTPA-loaded polymer-metal complex micelles with high relaxivity for MR cancer imaging*. Biomaterials, 2013. **34**(2): p. 492-500.
75. Kim, K.S., et al., *A cancer-recognizable MRI contrast agents using pH-responsive polymeric micelle*. Biomaterials, 2014. **35**(1): p. 337-43.
76. Einevoll, G.T., *Confinement of excitons in Quantum Dots*. Physical Review B, 1992. **45**(7): p. 3410-3417.
77. Takagahara, T. and K. Takeda, *Theory of the quantum confinement effect on excitons in Quantum Dots of indirect-gap materials*. Physical Review B, 1992. **46**(23): p. 15578-15581.
78. Takagahara, T., *Effects of dielectric confinement and electron-hole exchange interaction on excitonic states in semiconductor Quantum Dots*. Physical Review B, 1993. **47**(8): p. 4569-4585.
79. Alivisatos, A.P., *Perspectives on the Physical Chemistry of Semiconductor Nanocrystals*. The Journal of Physical Chemistry, 1996. **100**(31): p. 13226-13239.
80. Efros, A.L., *Interband absorption of light in a semiconductor sphere*. Soviet Physics Semiconductors-Ussr, 1982. **16**(7): p. 772-775.
81. Ekimov, A.I. and A.A. Onushchenko, *Quantum size effect in the optical-spectra of semiconductor micro-crystals*. Soviet Physics Semiconductors-Ussr, 1982. **16**(7): p. 775-778.

82. Murray, C., D.J. Norris, and M.G. Bawendi, *Synthesis and characterization of nearly monodisperse CdE (E= sulfur, selenium, tellurium) semiconductor nanocrystallites*. Journal of the American Chemical Society, 1993. **115**(19): p. 8706-8715.
83. Spanhel, L., et al., *Photochemistry of colloidal semiconductors- surface modification and stability of strong luminescing CdS particles*. Journal of the American Chemical Society, 1987. **109**(19): p. 5649-5655.
84. Dannhauser, T., et al., *Photophysics of quantized colloidal semiconductors dramatic luminescence enhancement by binding of simple amines*. Journal of Physical Chemistry, 1986. **90**(23): p. 6074-6076.
85. Kortan, A.R., et al., *Nucleation and growth of CdSe on ZnS quantum crystallite seeds, and vice versa, in inverse micelle media*. Journal of the American Chemical Society, 1990. **112**(4): p. 1327-1332.
86. Dabbousi, B.O., et al., *(CdSe)ZnS core-shell quantum dots: Synthesis and characterization of a size series of highly luminescent nanocrystallites*. Journal of Physical Chemistry B, 1997. **101**(46): p. 9463-9475.
87. Qu, L. and X. Peng, *Control of photoluminescence properties of CdSe nanocrystals in growth*. Journal of the American Chemical Society, 2002. **124**(9): p. 2049-2055.
88. Murray, C.B., D.J. Norris, and M.G. Bawendi, *Synthesis and characterization of nearly monodisperse CdE (E=S, Se, Te) semiconductor nanocrystallites*. Journal of the American Chemical Society, 1993. **115**(19): p. 8706-8715.
89. Peng, Z.A. and X.G. Peng, *Formation of high-quality CdTe, CdSe, and CdS nanocrystals using CdO as precursor*. Journal of the American Chemical Society, 2001. **123**(1): p. 183-184.
90. Yu, W.W. and X.G. Peng, *Formation of high-quality CdS and other II-VI semiconductor nanocrystals in noncoordinating solvents: Tunable reactivity of monomers*. Angewandte Chemie-International Edition, 2002. **41**(13): p. 2368-2371.
91. Hines, M.A. and P. Guyot-Sionnest, *Synthesis and characterization of strongly luminescing ZnS-Capped CdSe nanocrystals*. Journal of Physical Chemistry, 1996. **100**(2): p. 468-471.
92. Duan, H. and S. Nie, *Cell-penetrating quantum dots based on multivalent and endosome-disrupting surface coatings*. Journal of the American Chemical Society, 2007. **129**(11): p. 3333-3338.

93. Uyeda, H.T., et al., *Synthesis of compact multidentate ligands to prepare stable hydrophilic quantum dot fluorophores*. Journal of the American Chemical Society, 2005. **127**(11): p. 3870-3878.
94. Jana, N.R., et al., *Cysteine-functionalized polyaspartic acid: a polymer for coating and bioconjugation of nanoparticles and quantum dots*. Langmuir, 2010. **26**(9): p. 6503-6507.
95. Choi, H.S., et al., *Renal clearance of quantum dots*. Nature Biotechnology, 2007. **25**(10): p. 1165-1170.
96. Mattoussi, H., et al., *Self-assembly of CdSe-ZnS quantum dot bioconjugates using an engineered recombinant protein*. Journal of the American Chemical Society, 2000. **122**(49): p. 12142-12150.
97. Dubertret, B., et al., *In vivo imaging of quantum dots encapsulated in phospholipid micelles*. Science, 2002. **298**(5599): p. 1759-1762.
98. Gao, X.H., W.C.W. Chan, and S.M. Nie, *Quantum-dot nanocrystals for ultrasensitive biological labeling and multicolor optical encoding*. Journal of Biomedical Optics, 2002. **7**(4): p. 532-537.
99. Akerman, M.E., et al., *Nanocrystal targeting in vivo*. Proceedings of the National Academy of Sciences of the United States of America, 2002. **99**(20): p. 12617-12621.
100. Goldman, E.R., et al., *Self-assembled luminescent CdSe-ZnS quantum dot bioconjugates prepared using engineered poly-histidine terminated proteins*. Analytica Chimica Acta, 2005. **534**(1): p. 63-67.
101. Medintz, I.L., et al., *Self-assembled nanoscale biosensors based on quantum dot FRET donors*. Nature Materials, 2003. **2**(9): p. 630-638.
102. Howarth, M., et al., *Monovalent, reduced-size quantum dots for imaging receptors on living cells*. Nature Methods, 2008. **5**(5): p. 397-399.
103. Zhang, Y., et al., *HaloTag protein-mediated site-specific conjugation of bioluminescent proteins to quantum dots*. Angewandte Chemie-International Edition, 2006. **45**(30): p. 4936-4940.
104. Xue, M., et al., *A new nanoprobe based on FRET between functional quantum dots and gold nanoparticles for fluoride anion and its applications for biological imaging*. Biosensors & Bioelectronics, 2012. **36**(1): p. 168-173.
105. Lv, Y., K. Li, and Y. Li, *Surface modification of quantum dots and magnetic nanoparticles with PEG-conjugated chitosan derivatives for biological applications*. Chemical Papers, 2013. **67**(11): p. 1404-1413.

106. Regulacio, M.D., et al., *Aqueous synthesis of highly luminescent AgInS₂-ZnS quantum dots and their biological applications*. *Nanoscale*, 2013. **5**(6): p. 2322-2327.
107. Zhu, Y., et al., *One-pot preparation of highly fluorescent cadmium telluride/cadmium sulfide quantum dots under neutral-pH condition for biological applications*. *Journal of Colloid and Interface Science*, 2013. **390**: p. 3-10.
108. Chinnathambi, S., et al., *Silicon Quantum Dots for Biological Applications*. *Advanced Healthcare Materials*, 2014. **3**(1): p. 10-29.
109. Lin, L., et al., *Luminescent graphene quantum dots as new fluorescent materials for environmental and biological applications*. *Trac-Trends in Analytical Chemistry*, 2014. **54**: p. 83-102.
110. Karakoti, A.S., et al., *Surface functionalization of quantum dots for biological applications*. *Advances in Colloid and Interface Science*, 2015. **215**: p. 28-45.
111. Massey, M., et al., *Mind your P's and Q's: the coming of age of semiconducting polymer dots and semiconductor quantum dots in biological applications*. *Current Opinion in Biotechnology*, 2015. **34**: p. 30-40.
112. Peng, J., et al., *Biological Application of Luminescent Graphene Quantum Dots*. *Science of Advanced Materials*, 2015. **7**(10): p. 1945-1961.
113. Wang, J. and J. Qiu, *Luminescent Graphene Quantum Dots: As Emerging Fluorescent Materials for Biological Application*. *Science of Advanced Materials*, 2015. **7**(10): p. 1979-1989.
114. Zheng, X.T., et al., *Glowing Graphene Quantum Dots and Carbon Dots: Properties, Syntheses, and Biological Applications*. *Small*, 2015. **11**(14): p. 1620-1636.
115. Iyer, G., et al., *Peptide coated quantum dots for biological applications*. *Ieee Transactions on Nanobioscience*, 2006. **5**(4): p. 231-238.
116. Jamieson, T., et al., *Biological applications of quantum dots*. *Biomaterials*, 2007. **28**(31): p. 4717-4732.
117. Liu, J., et al., *Applications of Quantum Dots in Biological Analysis and Biomedical Diagnosis*. *Progress in Chemistry*, 2010. **22**(6): p. 1068-1076.
118. Obonyo, O., et al., *Quantum dots synthesis and biological applications as imaging and drug delivery systems*. *Critical Reviews in Biotechnology*, 2010. **30**(4): p. 283-301.

119. Rauf, S., A. Glidle, and J.M. Cooper, *Application of quantum dot barcodes prepared using biological self-assembly to multiplexed immunoassays*. Chemical Communications, 2010. **46**(16): p. 2814-2816.
120. Bilan, R., et al., *Quantum Dot Surface Chemistry and Functionalization for Cell Targeting and Imaging*. Bioconjugate Chemistry, 2015. **26**(4): p. 609-624.
121. Lim, S.Y., W. Shen, and Z. Gao, *Carbon quantum dots and their applications*. Chemical Society Reviews, 2015. **44**(1): p. 362-381.
122. Wegner, K.D. and N. Hildebrandt, *Quantum dots: bright and versatile in vitro and in vivo fluorescence imaging biosensors*. Chemical Society Reviews, 2015. **44**(14): p. 4792-4834.
123. Smith, A.M. and S.M. Nie, *Chemical analysis and cellular imaging with quantum dots*. Analyst, 2004. **129**(8): p. 672-677.
124. Wang, H., et al., *Biocompatible hyaluronic acid polymer-coated quantum dots for CD44+ cancer cell-targeted imaging*. Journal of Nanoparticle Research, 2014. **16**(10): p. 1-13.
125. Pathak, S., et al., *Hydroxylated quantum dots as luminescent probes for in situ hybridization*. Journal of the American Chemical Society, 2001. **123**(17): p. 4103-4104.
126. Jaiswal, J.K., et al., *Long-term multiple color imaging of live cells using quantum dot bioconjugates*. Nat Biotech, 2003. **21**(1): p. 47-51.
127. Lidke, D.S., et al., *Quantum dot ligands provide new insights into erbB/HER receptor-mediated signal transduction*. Nature Biotechnology, 2004. **22**(2): p. 198-203.
128. Dahan, M., et al., *Diffusion dynamics of glycine receptors revealed by single-quantum dot tracking*. Science, 2003. **302**(5644): p. 442-445.
129. Lieleg, O., et al., *Specific Integrin Labeling in Living Cells Using Functionalized Nanocrystals*. Small, 2007. **3**(9): p. 1560-1565.
130. Young, S.H. and E. Rozengurt, *Qdot Nanocrystal Conjugates conjugated to bombesin or ANG II label the cognate G protein-coupled receptor in living cells*. American Journal of Physiology-Cell Physiology, 2006. **290**(3): p. C728-C732.
131. Jaiswal, J.K., et al., *Long-term multiple color imaging of live cells using quantum dot bioconjugates*. Nature Biotechnology, 2003. **21**(1): p. 47-51.
132. Lagerholm, B.C., et al., *Multicolor coding of cells with cationic peptide coated quantum dots*. Nano Letters, 2004. **4**(10): p. 2019-2022.

133. Delehanty, J.B., et al., *Self-assembled quantum dot-peptide bioconjugates for selective intracellular delivery*. *Bioconjugate Chemistry*, 2006. **17**(4): p. 920-927.
134. Gardini, L., M. Capitanio, and F.S. Pavone, *3D tracking of single nanoparticles and quantum dots in living cells by out-of-focus imaging with diffraction pattern recognition*. *Scientific Reports*, 2015. **5**: p. 10.
135. Larson, D.R., et al., *Water-soluble quantum dots for multiphoton fluorescence imaging in vivo*. *Science*, 2003. **300**(5624): p. 1434-1436.
136. Gao, X.H., et al., *In vivo cancer targeting and imaging with semiconductor quantum dots*. *Nature Biotechnology*, 2004. **22**(8): p. 969-976.
137. Gao, X.H., et al., *In vivo molecular and cellular imaging with quantum dots*. *Current Opinion in Biotechnology*, 2005. **16**(1): p. 63-72.
138. So, M.K., et al., *Self-illuminating quantum dot conjugates for in vivo imaging*. *Nature Biotechnology*, 2006. **24**(3): p. 339-343.
139. Li, L., et al., *Highly Luminescent CuInS₂/ZnS Core/Shell Nanocrystals: Cadmium-Free Quantum Dots for In Vivo Imaging*. *Chemistry of Materials*, 2009. **21**(12): p. 2422-2429.
140. Morgan, N.Y., et al., *Real time in vivo non-invasive optical imaging using near-infrared fluorescent quantum dots*. *Academic Radiology*, 2005. **12**(3): p. 313-323.
141. Smith, A.M., et al., *Engineering luminescent quantum dots for In vivo molecular and cellular imaging*. *Annals of Biomedical Engineering*, 2006. **34**(1): p. 3-14.
142. Gao, X., et al., *Quantum Dots Bearing Lectin-Functionalized Nanoparticles as a Platform for In Vivo Brain Imaging*. *Bioconjugate Chemistry*, 2008. **19**(11): p. 2189-2195.
143. Jin, T., et al., *Gd(3+)-functionalized near-infrared quantum dots for in vivo dual modal (fluorescence/magnetic resonance) imaging*. *Chemical Communications*, 2008(44): p. 5764-5766.
144. Weng, K.C., et al., *Targeted tumor cell internalization and imaging of multifunctional quantum dot-conjugated immunoliposomes in vitro and in vivo*. *Nano Letters*, 2008. **8**(9): p. 2851-2857.
145. Kikkeri, R., et al., *In Vitro Imaging and in Vivo Liver Targeting with Carbohydrate Capped Quantum Dots*. *Journal of the American Chemical Society*, 2009. **131**(6): p. 2110-+.
146. Yong, K.-T., et al., *Biocompatible Near-Infrared Quantum Dots as Ultrasensitive Probes for Long-Term in vivo Imaging Applications*. *Small*, 2009. **5**(17): p. 1997-2004.

147. Gao, J., et al., *Ultrasmall Near-Infrared Non-cadmium Quantum Dots for in vivo Tumor Imaging*. *Small*, 2010. **6**(2): p. 256-261.
148. Gao, J., et al., *In Vivo Tumor-Targeted Fluorescence Imaging Using Near-Infrared Non-Cadmium Quantum Dots*. *Bioconjugate Chemistry*, 2010. **21**(4): p. 604-609.
149. Gu, Y.-P., et al., *Ultrasmall Near-Infrared Ag₂Se Quantum Dots with Tunable Fluorescence for in Vivo Imaging*. *Journal of the American Chemical Society*, 2012. **134**(1): p. 79-82.
150. Hong, G., et al., *In Vivo Fluorescence Imaging with Ag₂S Quantum Dots in the Second Near-Infrared Region*. *Angewandte Chemie-International Edition*, 2012. **51**(39): p. 9818-9821.
151. Maeda, H., et al., *Tumor vascular permeability and the EPR effect in macromolecular therapeutics: a review*. *Journal of Controlled Release*, 2000. **65**(1-2): p. 271-284.
152. Singhal, S., S. Nie, and M.D. Wang, *Nanotechnology Applications in Surgical Oncology*, in *Annual Review of Medicine*. 2010. p. 359-373.
153. Yu, X., et al., *Immunofluorescence detection with quantum dot bioconjugates for hepatoma in vivo*. *Journal of Biomedical Optics*, 2007. **12**(1).
154. Cai, W.B., et al., *Peptide-labeled near-infrared quantum dots for imaging tumor vasculature in living subjects*. *Nano Letters*, 2006. **6**(4): p. 669-676.
155. Yezhelyev, M.V., et al., *Emerging use of nanoparticles in diagnosis and treatment of breast cancer*. *Lancet Oncology*, 2006. **7**(8): p. 657-667.
156. Mulder, W.J.M., et al., *Quantum dots with a paramagnetic coating as a bimodal molecular imaging probe*. *Nano Letters*, 2006. **6**(1): p. 1-6.
157. Rumiana Bakalova, †, §, et al., *Silica-Shelled Single Quantum Dot Micelles as Imaging Probes with Dual or Multimodality*. *Analytical Chemistry*, 2006. **78**(16): p. 5925-32.
158. van Tilborg, G.A., et al., *Annexin A5-Conjugated Quantum Dots with a Paramagnetic Lipidic Coating for the Multimodal Detection of Apoptotic Cells*. *Bioconjugate Chemistry*, 2006. **17**(4): p. 865-868.
159. Weibo, C., et al., *Dual-function probe for PET and near-infrared fluorescence imaging of tumor vasculature*. *Journal of Nuclear Medicine Official Publication Society of Nuclear Medicine*, 2007. **48**(11): p. 1862-70.

160. Wang, S., et al., *Core/Shell Quantum Dots with High Relaxivity and Photoluminescence for Multimodality Imaging*. *J.am.chem.soc.*, 2007. **129**(13): p. 3848-3856.
161. Guo, W.S., et al., *Intrinsically Radioactive Cu-64 CuInS/ZnS Quantum Dots for PET and Optical Imaging: Improved Radiochemical Stability and Controllable Cerenkov Luminescence*. *Acs Nano*, 2015. **9**(1): p. 488-495.
162. Guo, W.S., et al., *Color-tunable Gd-Zn-Cu-In-S/ZnS quantum dots for dual modality magnetic resonance and fluorescence imaging*. *Nano Research*, 2014. **7**(11): p. 1581-1591.
163. Qiang, M., et al., *Multilayered, core/shell nanoprobe based on magnetic ferric oxide particles and quantum dots for multimodality imaging of breast cancer tumors*. *Biomaterials*, 2012. **33**(33): p. 8486-8494.
164. Selvan, S.T., *Silica-coated quantum dots and magnetic nanoparticles for bioimaging applications (Mini-Review)*. *Biointerphases Journal*, 2010. **5**(3): p. 110-115.
165. Tu, C.Q., et al., *Paramagnetic, Silicon Quantum Dots for Magnetic Resonance and Two-Photon Imaging of Macrophages*. *Journal of the American Chemical Society*, 2010. **132**(6): p. 2016-2023.
166. Koole, R., et al., *Paramagnetic Lipid-Coated Silica Nanoparticles with a Fluorescent Quantum Dot Core: A New Contrast Agent Platform for Multimodality Imaging*. *Bioconjugate Chemistry*, 2008. **19**(12): p. 2471-2479.
167. Wang, S., et al., *Core/shell quantum dots with high relaxivity and photoluminescence for multimodality imaging*. *Journal of the American Chemical Society*, 2007. **129**(13): p. 3848-3856.
168. Bakalova, R., et al., *Silica-shelled single quantum dot micelles as imaging probes with dual or multimodality*. *Analytical Chemistry*, 2006. **78**(16): p. 5925-5932.
169. Teston, E., et al., *Design, Properties, and In Vivo Behavior of Superparamagnetic Persistent Luminescence Nanohybrids*. *Small*, 2015. **11**(22): p. 2696-2704.
170. Chen, F., et al., *In Vivo Tumor Vasculature Targeted PET/NIRF Imaging with TRC105(Fab)-Conjugated, Dual-Labeled Mesoporous Silica Nanoparticles*. *Molecular Pharmaceutics*, 2014. **11**(11): p. 4007-4014.
171. Lin, X., et al., *Chimeric Ferritin Nanocages for Multiple Function Loading and Multimodal Imaging*. *Nano Letters*, 2011. **11**(2): p. 814-819.
172. Weibo, C., et al., *Dual-function probe for PET and near-infrared fluorescence imaging of tumor vasculature*. *Journal of Nuclear Medicine*, 2007. **48**(11): p. 1862-70.

173. Chen, K., et al., *Dual-modality optical and positron emission tomography imaging of vascular endothelial growth factor receptor on tumor vasculature using quantum dots*. European Journal of Nuclear Medicine and Molecular Imaging, 2008. **35**(12): p. 2235-2244.
174. Schipper, M.L., et al., *MicroPET-based biodistribution of quantum dots in living mice*. Journal of Nuclear Medicine, 2007. **48**(9): p. 1511-1518.
175. Gerion, D., et al., *Paramagnetic Silica-Coated Nanocrystals as an Advanced MRI Contrast Agent*. The Journal of Physical Chemistry C, 2007. **111**(34): p. 12542-12551.
176. Yang, H., et al., *Gd-III-functionalized fluorescent quantum dots as multimodal imaging probes*. Advanced Materials, 2006. **18**(21): p. 2890-+.
177. Sun, Y., et al., *Core-Shell Lanthanide Upconversion Nanophosphors as Four-Modal Probes for Tumor Angiogenesis Imaging*. Acs Nano, 2013. **7**(12): p. 11290-11300.
178. Heidt, T. and M. Nahrendorf, *Multimodal iron oxide nanoparticles for hybrid biomedical imaging*. Nmr in Biomedicine, 2013. **26**(7): p. 756-765.
179. Liu, Y., et al., *Optical probes and the applications in multimodality imaging*. Contrast Media & Molecular Imaging, 2011. **6**(4): p. 169-177.
180. Lim, Y.T., et al., *Multiplexed Imaging of Therapeutic Cells with Multispectrally Encoded Magnetofluorescent Nanocomposite Emulsions*. Journal of the American Chemical Society, 2009. **131**(47): p. 17145-17154.
181. Cherry, S.R., *Multimodality Imaging: Beyond PET/CT and SPECT/CT*. Seminars in Nuclear Medicine, 2009. **39**(5): p. 348-353.
182. Mulder, W.J.M., et al., *Nanoparticulate Assemblies of Amphiphiles and Diagnostically Active Materials for Multimodality Imaging*. Accounts of Chemical Research, 2009. **42**(7): p. 904-914.
183. Lucignani, G., *Nanoparticles for concurrent multimodality imaging and therapy: The dawn of new theragnostic synergies*. European Journal of Nuclear Medicine and Molecular Imaging, 2009. **36**(5): p. 869-874.
184. Mulder, W.J.M., et al., *Molecular imaging of tumor angiogenesis using alpha v beta 3-integrin targeted multimodal quantum dots*. Angiogenesis, 2009. **12**(1): p. 17-24.
185. Cormode, D.P., et al., *Nanocrystal Core High-Density Lipoproteins: A Multimodality Contrast Agent Platform*. Nano Letters, 2008. **8**(11): p. 3715-3723.

186. Cai, W.B. and X.Y. Chen, *Multimodality molecular imaging of tumor angiogenesis*. Journal of Nuclear Medicine, 2008. **49**: p. 113S-128S.
187. Kobayashi, H., et al., *Multimodal nanoprobe for radionuclide and five-color near-infrared optical lymphatic imaging*. Acs Nano, 2007. **1**(4): p. 258-264.
188. Mulder, W.J.M., et al., *Magnetic and fluorescent nanoparticles for multimodality imaging*. Nanomedicine, 2007. **2**(3): p. 307-324.
189. Shi, Y.P., et al., *Facile synthesis of gadolinium (III) chelates functionalized carbon quantum dots for fluorescence and magnetic resonance dual-modal bioimaging*. Carbon, 2015. **93**: p. 742-750.
190. Collins, M.N. and C. Birkinshaw, *Hyaluronic acid based scaffolds for tissue engineering-A review*. Carbohydrate Polymers, 2013. **92**(2): p. 1262-1279.
191. Murugan, R. and S. Ramakrishna, *Design strategies of tissue engineering scaffolds with controlled fiber orientation*. Tissue Engineering, 2007. **13**(8): p. 1845-1866.
192. Arpicco, S., et al., *Hyaluronic Acid Conjugates as Vectors for the Active Targeting of Drugs, Genes and Nanocomposites in Cancer Treatment*. Molecules, 2014. **19**(3): p. 3193-3230.
193. Naor, D., et al., *CD44 in Cancer*. Critical Reviews in Clinical Laboratory Sciences, 2002. **39**(6): p. 527-579(53).
194. Cichy, J. and E. Pure, *The liberation of CD44*. Journal of Cell Biology, 2003. **161**(5): p. 839-843.
195. Lesley, J., et al., *Hyaluronan binding by cell surface CD44*. Journal of Biological Chemistry, 2000. **275**(35): p. 26967-26975.
196. Kim, J., et al., *In vivo real-time bioimaging of hyaluronic acid derivatives using quantum dots*. Biopolymers, 2008. **89**(12): p. 1144-1153.
197. Kim, K.S., et al., *In Vivo Real Time Confocal Microscopy for Target Specific Delivery of Hyaluronic Acid-Quantum Dot Conjugates*. Nanomedicine: Nanotechnology, Biology and Medicine, 2012.
198. Kim, J., K. Park, and S.K. Hahn, *Effect of hyaluronic acid molecular weight on the morphology of quantum dot-hyaluronic acid conjugates*. International Journal of Biological Macromolecules, 2008. **42**(1): p. 41-45.
199. Abdullah Al, N., et al., *Target Delivery and Cell Imaging Using Hyaluronic Acid-Functionalized Graphene Quantum Dots*. Molecular Pharmaceutics, 2013. **10**(10): p. 3736-3744.

200. Goh, E.J., et al., *Bioimaging of Hyaluronic Acid Derivatives Using Nanosized Carbon Dots*. *Biomacromolecules*, 2012. **13**(8): p. 2554-2561.
201. Xie, R., et al., *Synthesis and characterization of highly luminescent CdSe-Core CdS/ZnO. 5CdO. 5S/ZnS multishell nanocrystals*. *Journal of the American Chemical Society*, 2005. **127**(20): p. 7480-7488.
202. Ying, J.Y. and A. Zarur, *Synthesis of nanometer-sized particles by reverse micelle mediated techniques*. 2002, Google Patents.
203. Britton, H.T.S. and R.A. Robinson, *CXCVIII.—Universal buffer solutions and the dissociation constant of veronal*. *Journal of the Chemical Society (Resumed)*, 1931: p. 1456-1462.
204. Clapp, A.R., E.R. Goldman, and H. Mattoussi, *Capping of CdSe–ZnS quantum dots with DHLA and subsequent conjugation with proteins*. *Nature Protocols*, 2006. **1**(3): p. 1258-1266.
205. Yildiz, I., et al., *Biocompatible CdSe– ZnS Core– Shell Quantum Dots Coated with Hydrophilic Polythiols*. *Langmuir*, 2009. **25**(12): p. 7090-7096.
206. Hermanson, G.T., *Chapter 1 - Functional Targets*, in *Bioconjugate Techniques (Second Edition)*, G.T. Hermanson, Editor. 2008, Academic Press: New York. p. 1-168.
207. Cai, W., et al., *Dual-function probe for PET and near-infrared fluorescence imaging of tumor vasculature*. *Journal of Nuclear Medicine*, 2007. **48**(11): p. 1862-1870.
208. Park, J., et al., *A DTTA-ligated uridine-quantum dot conjugate as a bimodal contrast agent for cellular imaging*. *Chemical Communications*, 2012. **48**(26): p. 3218-3220.
209. Stasiuk, G.J., et al., *Cell-Permeable Ln(III) Chelate-Functionalized InP Quantum Dots As Multimodal Imaging Agents*. *Acs Nano*, 2011. **5**(10): p. 8193-8201.
210. Erogbogbo, F., et al., *Bioconjugation of luminescent silicon quantum dots to gadolinium ions for bioimaging applications*. *Nanoscale*, 2012. **4**(17): p. 5483-5489.
211. Koole, R., et al., *Paramagnetic Lipid-Coated Silica Nanoparticles with a Fluorescent Quantum Dot Core: A New Contrast Agent Platform for Multimodality Imaging*. *Bioconjugate Chemistry*, 2008. **19**(12): p. 2471-2479.
212. Mulder, W.J.M., et al., *Molecular imaging of tumor angiogenesis using $\alpha\text{v}\beta\text{3}$ -integrin targeted multimodal quantum dots*. *Angiogenesis*, 2008. **12**(1): p. 17-24.

213. van Tilborg, G.A.F., et al., *Annexin A5-Conjugated Quantum Dots with a Paramagnetic Lipidic Coating for the Multimodal Detection of Apoptotic Cells*. *Bioconjugate Chemistry*, 2006. **17**(4): p. 865-868.
214. van Schooneveld, M.M., et al., *Improved Biocompatibility and Pharmacokinetics of Silica Nanoparticles by Means of a Lipid Coating: A Multimodality Investigation*. *Nano Letters*, 2008. **8**(8): p. 2517-2525.
215. Mulder, W.J.M., et al., *Molecular imaging of macrophages in atherosclerotic plaques using bimodal PEG-micelles*. *Magnetic Resonance in Medicine*, 2007. **58**(6): p. 1164-1170.
216. Mulder, W.J.M., et al., *Quantum Dots with a Paramagnetic Coating as a Bimodal Molecular Imaging Probe*. *Nano Letters*, 2006. **6**(1): p. 1-6.
217. Erwin, S.C., et al., *Doping semiconductor nanocrystals*. *Nature*, 2005. **436**(7047): p. 91-94.
218. Beaulac, R., et al., *Mn²⁺-Doped CdSe Quantum Dots: New Inorganic Materials for Spin-Electronics and Spin-Photonics*. *Advanced Functional Materials*, 2008. **18**(24): p. 3873-3891.
219. Bhattacharjee, A.K. and J. Pérez-Conde, *Transition metal-doped quantum dots: Optical detection and manipulation of spin states*. *Physica E: Low-dimensional Systems and Nanostructures*, 2006. **32**(1-2): p. 430-433.
220. Ma, L., et al., *Magnetic properties of transition-metal impurities in silicon quantum dots*. *Physical Review B*, 2007. **75**(4): p. 045312.
221. Mahamuni, S., A.D. Lad, and S. Patole, *Photoluminescence Properties of Manganese-Doped Zinc Selenide Quantum Dots*. *The Journal of Physical Chemistry C*, 2008. **112**(7): p. 2271-2277.
222. Radovanovic, P.V., et al., *Colloidal Transition-Metal-Doped ZnO Quantum Dots*. *Journal of the American Chemical Society*, 2002. **124**(51): p. 15192-15193.
223. Bhattacharjee, A.K. and J. Pérez-Conde, *Optical properties of paramagnetic ion-doped semiconductor nanocrystals*. *Physical Review B*, 2003. **68**(4): p. 045303.
224. Huong, N.Q. and J.L. Birman, *Theory of luminescent emission in nanocrystal ZnS:Mn with an extra electron*. *Physical Review B*, 2004. **69**(8): p. 085321.
225. Magana, D., et al., *Switching-on Superparamagnetism in Mn/CdSe Quantum Dots*. *Journal of the American Chemical Society*, 2006. **128**(9): p. 2931-2939.
226. Sahoo, Y., et al., *Chemically Fabricated Magnetic Quantum Dots of InP:Mn*. *The Journal of Physical Chemistry B*, 2005. **109**(32): p. 15221-15225.

227. Bol, A.A. and A. Meijerink, *Luminescence Quantum Efficiency of Nanocrystalline ZnS:Mn²⁺. 1. Surface Passivation and Mn²⁺ Concentration*. The Journal of Physical Chemistry B, 2001. **105**(42): p. 10197-10202.
228. Reiss, P., M. Protière, and L. Li, *Core/Shell Semiconductor Nanocrystals*. Small, 2009. **5**(2): p. 154-168.
229. Yim, H., et al., *The performance of gadolinium diethylene triamine pentaacetate-pullulan hepatocyte-specific T1 contrast agent for MRI*. Biomaterials, 2011. **32**(22): p. 5187-5194.
230. Cho, H.-J., et al., *Hyaluronic acid-ceramide-based optical/MR dual imaging nanoprobe for cancer diagnosis*. Journal of Controlled Release, 2012. **162**(1): p. 111-118.
231. Chen, H., et al., *Folate Conjugated CdHgTe Quantum Dots with High Targeting Affinity and Sensitivity for In vivo Early Tumor Diagnosis*. Journal of Fluorescence, 2011. **21**(2): p. 793-801.
232. Yimei, L., et al., *Aqueous synthesized near-infrared-emitting quantum dots for RGD-based in vivo active tumour targeting*. Nanotechnology, 2013. **24**(13): p. 135101.
233. Qin, M.-Y., et al., *In vivo cancer targeting and fluorescence-CT dual-mode imaging with nanoprobe based on silver sulfide quantum dots and iodinated oil*. Nanoscale, 2015. **7**(46): p. 19484-19492.
234. Chen, H., et al., *Characterization of tumor-targeting Ag₂S quantum dots for cancer imaging and therapy in vivo*. Nanoscale, 2014. **6**(21): p. 12580-12590.
235. Oh, E.J., et al., *Target specific and long-acting delivery of protein, peptide, and nucleotide therapeutics using hyaluronic acid derivatives*. Journal of Controlled Release, 2010. **141**(1): p. 2-12.
236. Yong, K.-T., et al., *Synthesis of cRGD-peptide conjugated near-infrared CdTe/ZnSe core-shell quantum dots for in vivo cancer targeting and imaging*. Chemical Communications, 2010. **46**(38): p. 7136-7138.
237. Chen, L.-N., et al., *Aqueous one-pot synthesis of bright and ultrasmall CdTe/CdS near-infrared-emitting quantum dots and their application for tumor targeting in vivo*. Chemical Communications, 2012. **48**(41): p. 4971-4973.